2019

Improving intermediate temperature performance of NI-YSZ cermet anodes for solid oxide fuel cells by infiltration of nickel nanoparticles and mixed ionic electronic conductors

BOSTON UNIVERSITY

COLLEGE OF ENGINEERING

Dissertation

IMPROVING INTERMEDIATE TEMPERATURE PERFORMANCE OF NI-YSZ CERMET ANODES FOR SOLID OXIDE FUEL CELLS BY INFILTRATION OF NICKEL NANOPARTICLES AND MIXED IONIC ELECTRONIC CONDUCTORS

by

YANCHEN LU

B.S., University of Alberta, 2014
M.S., Boston University, 2015

Submitted in partial fulfillment of the

requirements for the degree of

Doctor of Philosophy

2019

Approved by

First Reader

Soumendra N. Basu, Ph.D.
Professor of Mechanical Engineering
Professor and Associate Division Head of Materials Science and Engineering

Second Reader

Uday B. Pal, Ph.D.
Professor of Mechanical Engineering
Professor of Materials Science and Engineering

Third Reader

Srikanth Gopalan, Ph.D.
Associate Professor of Mechanical Engineering
Associate Professor of Materials Science and Engineering

Fourth Reader

Karl F. Ludwig, Jr., Ph.D.
Professor of Physics
Professor of Materials Science and Engineering

DEDICATION

I would like to dedicate this work to my father Hai Lu, my mother Yin Yan, and my wife Yenai Ma.

ACKNOWLEDGMENTS

First, I am deeply indebted to my research advisor, Prof. Soumendra N. Basu. I would like to thank him for offering me such a great opportunity to join this thoughtful and rewarding journey. My PhD study was accompanied with his expert guidance and relaxing humor. I also grateful to Prof. Uday B Pal and Prof. Srikanth Gopalan for their innovative ideas and encouragement. I also would like to thank Prof. Karl Ludwig and Prof. Shyamsunder Erramilli for serving on my thesis committee and chairing my dissertation defense.

I would like to thank Prof. Elise Morgan, Dr. Alexey Nikiforov, Ms. Anlee Krupp, Dr. Jeffrey Bacon, Ms. Kara Mogensen, and Mr. Bob Sjostrom for their technical assistance. Many thanks to Ms. Elizabeth Flagg, Ms, Ruth Mason, and Ms. Gabriella McNevin for their administrative help.

I also would like to acknowledge all my colleagues: Dr. Yang Yu, Dr. Deniz Cetin, Dr. Yihong Jiang, Dr. Shizhao Su, Dr. Ryan Eriksen, Dr. Mustafa Ordu, Dr. Jicheng Guo, Dr. Zhihao Sun, Dr. Ruofan Wang, Dr. Yiwen Gong, Dr. Thomas Villalon, Mr. Paul Gasper, Mr. Boshan Mo, Mr. Ben Levitas, Ms. Jane Banner, Mr. Zhikuan Zhu, Ms. Michelle Sugimoto, Ms. Yuexin Zhu, Mr. Haoxuan Yan.

This research was funded in part by the U.S. Department of Energy, National Energy Technology Laboratory under award number DEFE0026096.

Last but not least, I would like to express my deepest gratitude to my parents and my wife. This dissertation would not have been possible without their warm love, and endless support.

IMPROVING INTERMEDIATE TEMPERATURE PERFORMANCE OF NI-YSZ CERMET ANODES FOR SOLID OXIDE FUEL CELLS BY INFILTRATION OF NICKEL NANOPARTICLES AND MIXED IONIC ELECTRONIC CONDUCTORS

YANCHEN LU

Boston University College of Engineering, 2019

Major Professor: Soumendra N. Basu, Ph.D., Professor of Mechanical Engineering, Professor and Associate Division Head of Materials Science and Engineering

ABSTRACT

Solid oxide fuel cells (SOFCs) are one of the most efficient and environment-friendly devices for electricity generation. One critical challenge of SOFC commercialization is high cell operating temperatures (800°C-1000°C), which lead to high material costs, high performance degradation rates, long start-up and shutdown times, and limited portable applications. Intermediate temperature (600°C-800°C) operation of SOFCs is limited by sluggish electrode reaction kinetics. The objective of this research is to improve intermediate temperature performance of commercially available Ni-YSZ cermet anode supported SOFCs by liquid infiltration of the anode.

One effective method to improve kinetics of electrochemical reactions at the anode is to increase the density of reaction sites, which are known as the triple phase boundaries (TPBs). The porous Ni-YSZ cermet anodes were liquid infiltrated with Ni nanoparticles, leading to a four-fold increase in TPB density in the anode. The improved electrochemical performance of the infiltrated cells compared to the uninfiltrated cells highlights the effectiveness of anode infiltration in facilitating improved anode

electrochemical reaction kinetics. However, the post-electrochemical testing characterization revealed that Ni nanoparticles were not stable due to Ni coarsening and were mostly isolated indicating that not all of the additional TPBs were fully utilized in electrochemical reactions due to the lack of an electronic pathway between the Ni nanoparticles.

In order to improve microstructural stability of the infiltrated Ni nanoparticles, and to fully utilize the added TPBs, co-infiltration of Ni with a mixed ionic and electronic conductor (MIEC) was carried out. Two MIEC materials are chosen based on their chemical stability and conductivity in the anode operating environments; $Gd_{0.1}Ce_{0.9}O_{2-\delta}$ (GDC), a predominantly an ionic conductor, and $La_{0.6}Sr_{0.3}Ni_{0.15}Cr_{0.85}O_{3-\delta}$ (LSNC), a predominantly electronic conductor, and cells were successfully co-infiltrated to form Ni-GDC and Ni-LSNC nanostructures with the MIEC phases connecting the Ni nanoparticles. Stability tests demonstrated that both MIECs inhibited Ni nanoparticle coarsening. Electrochemical studies showed that Ni-GDC is the most effective for improved anode kinetics. A long-term (120 hours) electrochemical test indicated that infiltration of Ni-GDC into Ni-YSZ cermet anode effectively improves overall cell performance at intermediate temperatures and maintains the performance gain for a long period of time.

TABLE OF CONTENTS

LIST OF TABLES

LIST OF FIGURES

LIST OF ABBREVIATIONS

2PB.....Double Phase Boundary

AAL .....Anode Active Layer

ACCL..... Anode Current Collector Layer

AFC.....Alkaline Fuel Cell

CAL .....Cathode Active Layer

CCCL.....Cathode Current Collector Layer

CTE.....Coefficient of Thermal Expansion

EDX .....Energy Dispersive X-Ray Spectroscopy

EIS ..... Electrochemical Impedance Spectroscopy

FIB ..... Focused Ion Beam

GDC.....Gadolinia-Doped Ceria

HAADF..... High Angle Annular Dark Field

HOR..... Hydrogen Oxidation Reaction

I-V..... Current-Voltage

LSCF..... Strontium Doped Lanthanum Cobalt Ferrite

LSM .....Lanthanum Strontium Manganite

LSNC ..... Ni Doped Lanthanum Strontium Chromite

MCFC .....Molten Carbonate Fuel Cell

MIEC .....Mixed Ionic Electronic Conducting

ORR ..... Oxygen Reduction Reaction

PAFC .....Phosphoric Acid Fuel Cell

PEMFC ..... Polymer Electrolyte Membrane Fuel Cell

ROI.....Region of Interest

SEM .....Scanning Electron Microscopy

SOFC ..... Solid-Oxide Fuel Cell

STEM..... Scanning Transmission Electron Microscopy

SZY .....Yttrium Doped Strontium Zirconate

TEM ..... Transmission Electron Microscope

TPBs..... Triple Phase Boundaries

XRD .....X-Ray Diffraction

YSZ..... Yttria-Stabilized Zirconia

1. Introduction

1.1 Fuel cells

Fuel cells are electrochemical devices that convert chemical energy directly to electrical energy, and generate power more efficiently and in a sustainable fashion compared to power generation systems that operate on fuel combustion. In a conventional combustion engine, the fuel is burned to generate heat. The resulting heat is first converted into mechanical energy, and finally into electrical energy. The efficiency of these processes is limited by the Carnot efficiency of the system, which depends on the temperatures of the hot source and the cold environment. Carnot efficiency is high only when the cold environmental temperature is very low and/or when the hot source temperature is very high.

In contrast to combustion engines, fuel cells have no intermediate energy conversion steps and can produce electricity directly from electrochemical reactions. Figure 1 shows a comparison of electrical efficiencies of fuel cells and energy generation systems based on internal combustion, at different ranges of power generation [1]. In general, fuel cells of various types have higher electrical efficiency than energy generation systems based on internal combustion, especially in the ‘local production’ (or on-site generation) regime. Another advantage of fuel cells is that due to the absence of direct combustion, fuels cells do not generate NO_x and SO_x, which are major contributors to air pollution. Finally, when using a hydrocarbon as fuel, carbon dioxide generated by fuel cells can be easily sequestered.

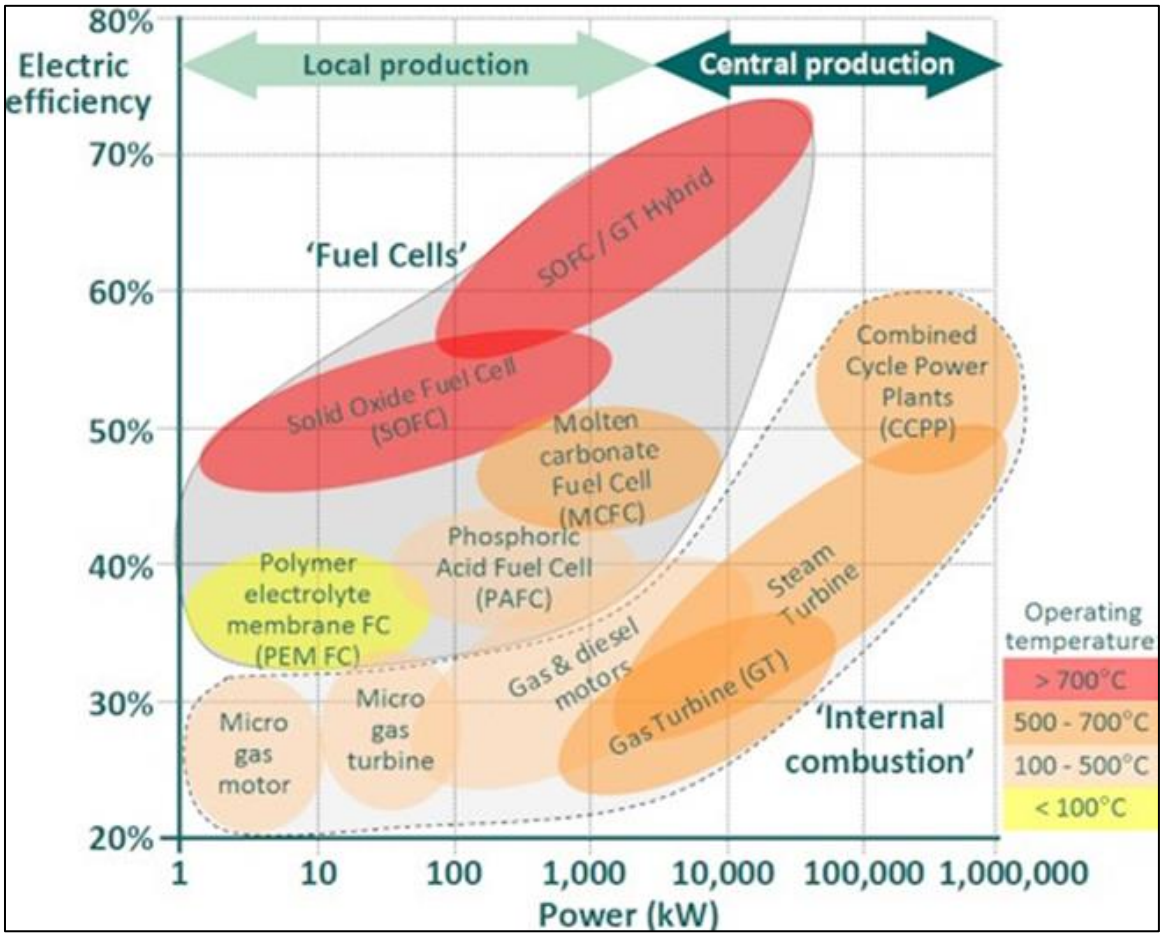

Figure 1. Plots of electrical efficiency versus power generation for various energy producing systems [1].

1.2 Types of fuel cells

There are five major types of fuel cells: i) phosphoric acid fuel cell (PAFC), ii) polymer electrolyte membrane fuel cell (PEMFC), iii) alkaline fuel cell (AFC), iv) molten carbonate fuel cell (MCFC), and v) solid-oxide fuel cell (SOFC). Table 1 shows typical characteristics of each type of fuel cells [2,3]. Among them, SOFCs have received significant attention due to better fuel flexibility, absence of precious metal catalysts, and relatively high-power output.

Table 1. Typical characteristics of different types of fuel cells [2,3].

	PEMFC	AFC	PAFC	MCFC	SOFC
Operating temperature (°C)	50-100	90-100	150-200	600-700	600-1000
Catalyst	Platinum	Platinum	Platinum	Nickel	Nickel/ Perovskite (Ceramic)
Fuel compatibility	H_2, methanol	H_2	H_2	H_2, CH_4	H_2, CH_4, CO
System Output (kW)	<1-250	10-100	50-1000	<1-1000	<1-3000

1.3 Working principle of SOFCs

Figure 2 shows a schematic of the working principle of a SOFC, with hydrogen as the fuel. The hydrogen combustion reaction is split into two electrochemical half reactions at the anode and the cathode, which are separated by a dense electrolyte. The oxidant (oxygen or air) is delivered to the porous cathode and reacts with electrons coming from the external electrical circuit forming oxygen ions at the electrolyte/cathode interface. This is known as the oxygen reduction reaction (ORR). The electrolyte is an ionic conductor allowing oxygen ions migration from the cathode to the anode. The fuel (hydrogen) is delivered to the porous anode and reacts with oxygen ions forming water and electrons at the anode/electrolyte interface. This is known as the hydrogen oxidation reaction (HOR). Electrons are transported through an external electrical circuit providing DC current. Excess fuel and generated water are removed from the anode and unused oxidant is removed from the cathode.

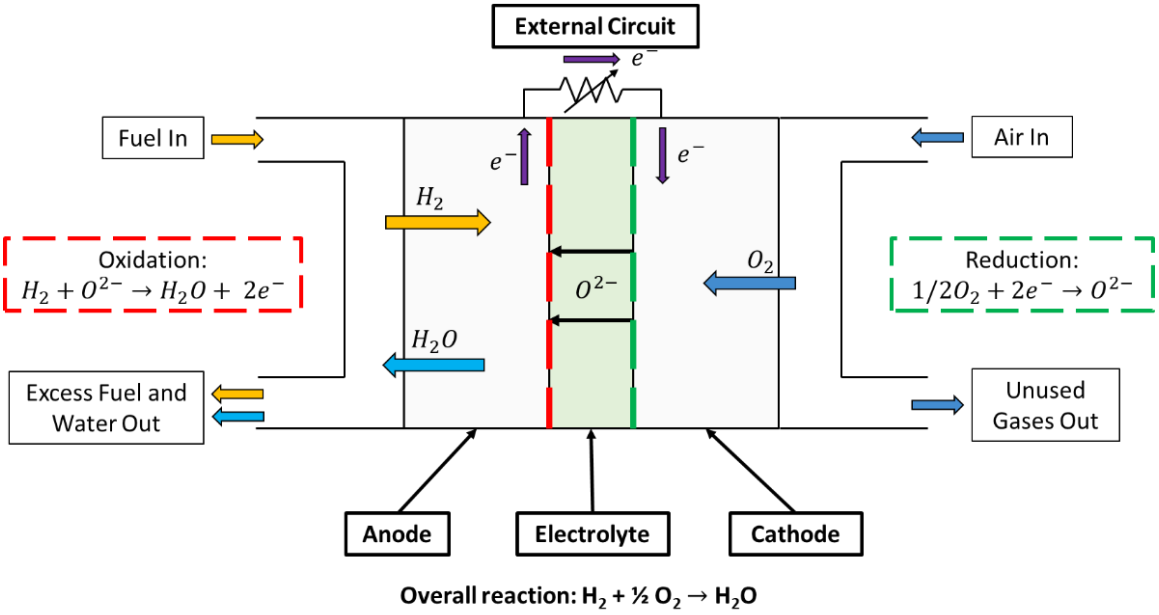

Figure 2. Schematic of the working principle of SOFCs.

1.4 SOFC materials

1.4.1 Electrolyte materials

The main function of the SOFC electrolyte is to allow ion transport between the anode and the cathode, and to physically separate the fuel and the oxidant to avoid gas mixing. Therefore, the electrolyte material selection needs to meet the following criteria:

1. High ionic conductivity and no electronic conductivity at cell operation temperatures. The oxygen ions are easily transported through the electrolyte and enable efficient electrochemical reactions. Furthermore, the electrolyte functions as an electron barrier meaning the electrons only travel through the external circuit to maintain a high current efficiency.

2. Excellent thermal stability at fabrication, and operating temperatures, along with high chemical stability in reducing and oxidizing atmospheres.
3. A good coefficient of thermal expansion (CTE) match with the electrodes to prevent cracking during thermal cycling.
4. Chemically stable when interacting with both electrodes in reducing and oxidizing atmospheres.
5. Good sinterability to form a fully dense electrolyte to prevent mixing of the fuel and oxidant at the anode and cathode, respectively.

The well-known candidates of SOFC electrolytes are yttria-stabilized zirconia (YSZ) and gadolinia-doped ceria (GDC). A typical YSZ electrolyte contains 8mol% Y_2O_3 in ZrO_2. The existence of Y_2O_3 helps to stabilize the zirconia cubic structure and, moreover, it increases oxygen vacancies in the zirconia crystal structure enabling more ionic transport. In contrast to YSZ, GDC has higher ionic conductivity, especially at lower temperatures. However, under reducing environments, the dopants are reduced from Ce^{4+} to Ce^{3+}, which causes n-type electronic conductivity that can trigger internal short circuits which lower the electrical efficiency [4].

1.4.2 Anode materials

The function of the SOFC anode is to provide reaction sites for electrochemical oxidation and efficient transport for reactants and products. A good anode material should meet the following criteria:

1. High catalytic activity for the fuel oxidation reaction.
2. High electronic conductivity.

3. Good chemical stability in reducing environments.
4. Good CTE match and material compatibility with the electrolyte.
5. Sufficient porosity for effective gas-phase diffusion of reactants and products without compromising mechanical strength.

Ni-YSZ cermet is the most commonly used anode material. Ni-YSZ cermet anodes are prepared by mixing and sintering NiO and YSZ powders. During cell operation, the NiO is reduced *in-situ* to Ni, which provides enough porosity for gas diffusion in and out of the porous anode. Ni is a very good electronic conductor allowing electrons to move from the anode/electrolyte interface to the external circuit. Ni is also an excellent catalyst for hydrogen adsorption [5]. Facile hydrogen adsorption lowers the activation energy barrier of the hydrogen oxidation reaction and improves the electrocatalytic activity. The YSZ provides a structural framework to match the thermal expansion of YSZ electrolyte and also functions as an inhibitor for Ni coarsening by pinning the percolating Ni grains. The high ionic conductivity of YSZ allows oxygen ions to be transported further away from the anode/electrolyte interface, thereby extending the electrochemically active region.

1.4.3 Cathode materials

The function of the SOFC cathode is to provide reaction sites for electrochemical reduction and proper gas-phase transport of the oxidant. A good cathode material should meet following criteria:

1. High catalytic activity for the oxygen reduction reaction.
2. High electronic conductivity.

3. Good chemical stability in oxidizing environments.
4. Good CTE match and material compatibility with the electrolyte.
5. Sufficient porosity for effective gas-phase diffusion of oxidant.

A perovskite-type lanthanum strontium manganite (LSM) is widely used as a cathode material. The LSM behaves as a p-type conductor due to its cation vacancies [6]. Doping Sr^{2+} into lanthanum manganite under oxidizing conditions results in the creation of Mn^{4+} species. The Mn^{3+}/Mn^{4+} pairs offer more electron transfer, which can further increase electronic conductivity. LSM also has good catalytic activity for oxygen reduction reaction due to the mixed valence states of the Mn ion. Due to the low ionic conductivity of LSM, a layer of LSM-YSZ composite is commonly used as the cathode active layer at the cathode/electrolyte interface. Another widely used cathode material is strontium doped lanthanum cobalt ferrite (LSCF), which is a mixed ionic electronic conducting (MIEC) material.

1.5 SOFC performance

The performance of a SOFC can be summarized by a current-voltage (I-V) curve, which is shown schematically in Figure 3 [7]. The curve shows the cell operating voltage as a function of current density. The horizontal line is the case for an ideal fuel cell with no irreversible losses occurring during cell operation.

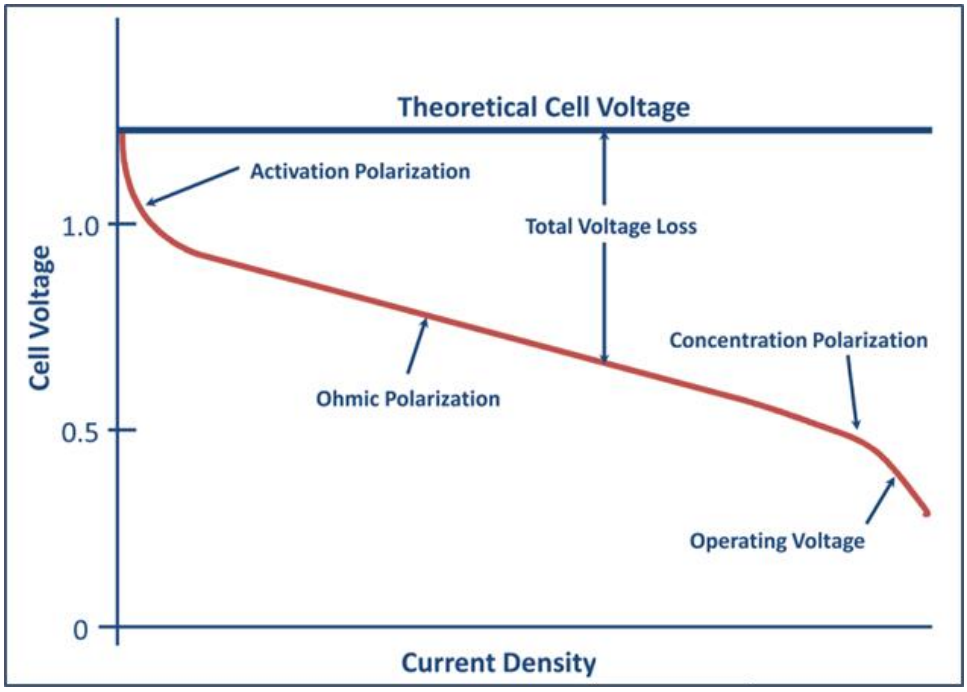

Figure 3. Schematic of a current-voltage curve showing regions dominated by activation, ohmic, and concentration polarizations [7].

However, for a real cell, there are three major losses that lower the cell voltage during operation. These losses are often referred to as polarization, resistance, or overpotential. These losses can be separated into the following categories:

1. Activation polarization (charge transfer resistance) is due to sluggish electrode kinetics. All electrochemical reactions need to overcome the activation energy barrier and the cell voltage is sacrificed to lower this activation energy barrier to accelerate the reaction rates. There are four ways to improve the kinetics of electrochemical reactions to decrease activation polarization. These are:
    a) Increase the reactant concentration.
    b) Decrease the activation energy barrier using catalysts.

c) Increase the temperature.

d) Increase the number of reaction sites.

2. Ohmic polarization (ohmic resistance) includes three major resistances contributing to ohmic polarization: contact resistance, electronic resistance, and ionic resistance. The contact resistance is due to incomplete physical contacts between interfaces of materials. The electronic and ionic resistances are caused by the resistance to the flow of electrons and ions in the electrode and electrolyte. In a SOFC application, the ohmic resistance of electrolyte is the dominating factor and it can be minimized by either decreasing the thickness or increasing the ionic conductivity of the electrolyte.
3. Concentration polarization is related to mass transfer resistance. The electrochemical reactions involve gas-phase supply and removal of reactants and products and poor mass transfer in the electrode causes concentration polarization. Mass transfer can be improved by increased gas diffusion. The gas diffusion coefficient is proportional to the porosity of the electrode, the volume fraction of the pore phase, and inversely proportional to the tortuosity (the extent of twist in a gas diffusion path) of pore phase. The concentration polarization can be mitigated by optimizing electrode microstructure by modifying both porosity and tortuosity to facilitate effective gas phase diffusion.

2. Technical issues related to SOFC operation

2.1 Lowering the temperature of SOFC operation

In 1899, YSZ was first discovered by Walther Nernst [8] and it has been used as the electrolyte of SOFCs since the 1930s due to its good ionic conductivity at high temperatures (1000°C) [9]. This high operation temperature caused multiple technical issues that impeded SOFC commercialization. These include: high material costs, high performance degradation rates, long start-up and shutdown times, and limited portable applications. Therefore, lowering SOFC operating temperature has been a key topic for SOFC research for many decades. At lower temperatures, the high polarization losses including high ohmic resistance of the electrolyte and slow electrode reaction kinetics are the primary concerns.

Early designs of SOFC cell configurations were electrolyte-supported, with an electrolyte thickness in excess of 100 μm. A high stability electrolyte material, like YSZ, minimizes the tendency for delamination of electrodes even with a CTE mismatch between the electrolyte and the electrodes [10]. However, the drawback of a thick electrolyte is high ohmic resistance, especially at lower temperatures. Therefore, SOFC manufactures have changed to an anode-supported cell design with thinner electrolytes (10 μm or less) enabling intermediate temperature (600-800°C) operation.

The slow electrode kinetics can be improved by optimizing electrode microstructure. As mentioned in Chapter 1.5, increasing the number of reaction sites is a promising method to improve electrode kinetics. The electrochemical reactions sites in

the anode and in LSM cathodes are called the triple phase boundaries (TPBs), which are one-dimensional regions where the gas phase, the ionically conducting phase, and the electronically conducting phase all meet. The TPB density is directly related to the feature size of electrode materials. By decreasing the feature sizes in the electrodes from the micro- to the nano-scale regime, the TPB density increases, leading to a dramatic increase in the electrode kinetics [11]. Liquid infiltration/wet impregnation is a technique to introduce immobilized and high-surface-area catalytic particles onto the surface of a substrate material [12]. This technique has been proved as an effective method to increase TPB density and maintain cell performance and reliability. The next section reviews literature on the modification of SOFC anodes by liquid infiltration.

2.2 Modification of SOFC anodes by liquid infiltration

As mentioned in Chapter 1.4.2, the state-of-the-art SOFC cell design uses Ni-YSZ cermet as an anode. However, Ni-YSZ cermet anodes still face the following technical issues: carbon coking and sulfur poisoning resulting from hydrocarbon fuels, low redox cycling ability, and poor electrode kinetics at lower temperatures. Researchers have explored liquid infiltration of the anode to overcome these issues.

2.2.1 Carbon coking

One of the major advantages of SOFCs is excellent fuel flexibility [13–16]. At high operating temperatures, the hydrocarbon fuels can be directly utilized by internal reforming. However, at intermediate operating temperatures in the absence of copious amounts of water vapor, Ni is a good catalyst for the formation of carbon fibers. The deposited carbon fibers near Ni grains can build up and block gas diffusion leading to cell

performance degradation and even cell cracking (Figure 4) [17]. This phenomenon is called carbon coking. Jin et al. found that the addition of a proton conducting material like $SrZr_{0.95}Y_{0.05}O_{3-\delta}$ (SZY) into Ni-YSZ cermet by infiltration can produce more water vapor near the TPBs, which effectively suppresses carbon deposition [18]. Jung et al. have shown that the carbon deposition can also be avoided by replacing Ni with Cu, which does not catalyze carbon formation. These anodes were prepared by infiltrating Cu using a copper nitrate solution into a YSZ backbone [19].

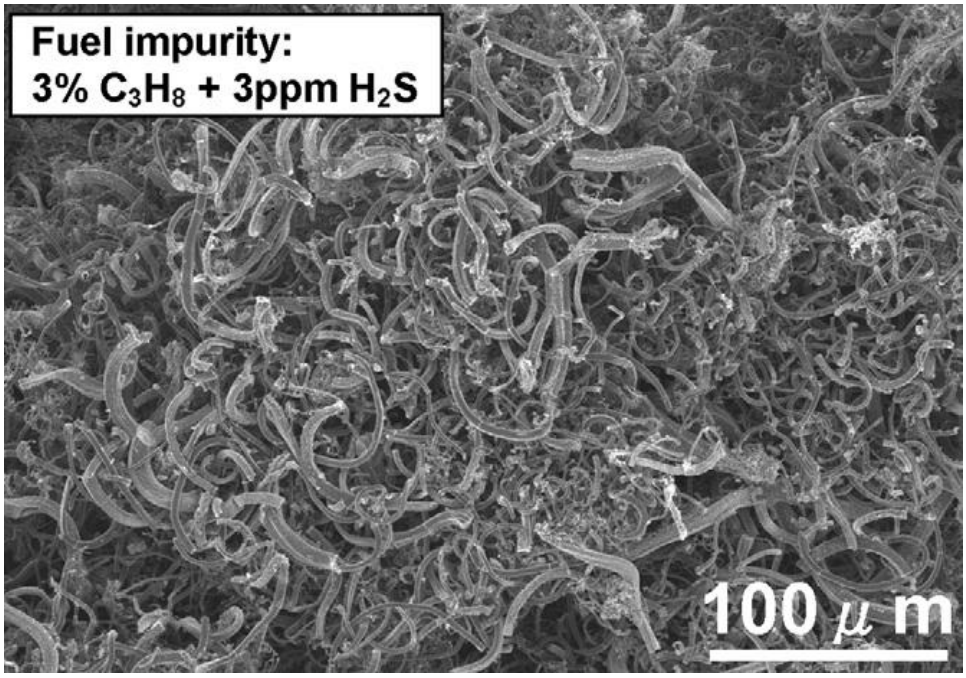

Figure 4. Deposited carbon fibers on the anode surfaces after 200h test using hydrocarbon fuels [17].

2.2.2 Sulfur poisoning

Another problem with using hydrocarbon fuels is the presence of sulfur as an impurity. Even a few ppm of sulfur compounds can negatively affect the Ni-YSZ anode performance [20,21]. At reduced temperatures, the sulfide impurities (mostly hydrogen

sulfide, H_2S) are easily adsorbed on Ni surfaces, as shown in Figure 5 [22]. This lowers the Ni catalytic activity and degrades the cell performance significantly, a phenomenon called sulfur poisoning [23]. Kurokawa et al. have shown that introducing CeO_2 nanocoatings by infiltration into Ni-YSZ cermet anodes effectively mitigates sulfur poisoning [24]. Chen et al. impregnated $Mo_{0.1}Ce_{0.9}O_2$ into Ni-YSZ cermet anodes and demonstrated long-term stability when exposed to H_2 with 50 ppm H_2S [25].

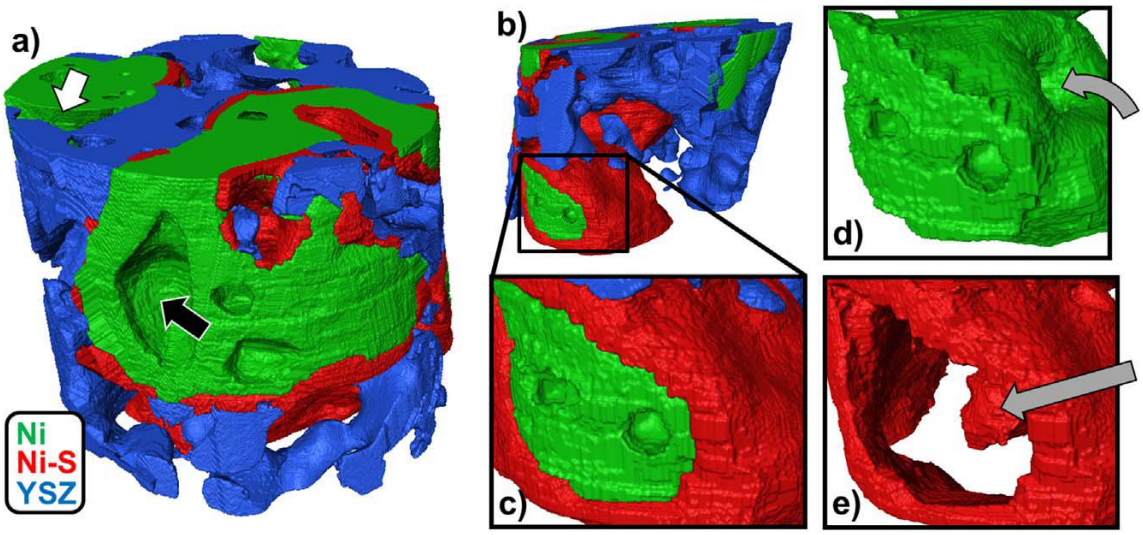

Figure 5. a) 3-D structure of the cylindrical sample after testing with exposure to 100 ppm H_2S for 1h. b) and c) Zoom-in views of the sample showing the d) Ni- and e) S-containing phases [22].

2.2.3 Redox cycling

During SOFC operation, accidental fuel shortages or operating at high fuel utilization may expose the anode to an oxidizing atmosphere which causes the Ni to oxidize to NiO, which is then reduced back to Ni when normal operation is resumed. The volume change between Ni and NiO can be detrimental to integrity of the cell microstructure, and can lead to cell cracking [26,27]. This mechanism is shown

schematically in Figure 6 [28]. Hua et al. showed (Ni,Mg)O-impregnated anodes with a YSZ backbone to have excellent redox cycling resistance, which is attributed to the addition of Mg lowering the reducibility of (Ni,Mg)O particles [29]. Futamura et al. has compared the redox cycling stability of a conventional Ni/scandia-stabilized zirconia cermet anode with two anodes consisting of a LSM/GDC backbone, one infiltrated with Ni and the other co-infiltrated with Ni-GDC. The Ni-GDC co-infiltrated anode showed the best redox stability, suggesting that the co-infiltrated GDC suppresses Ni agglomeration [30].

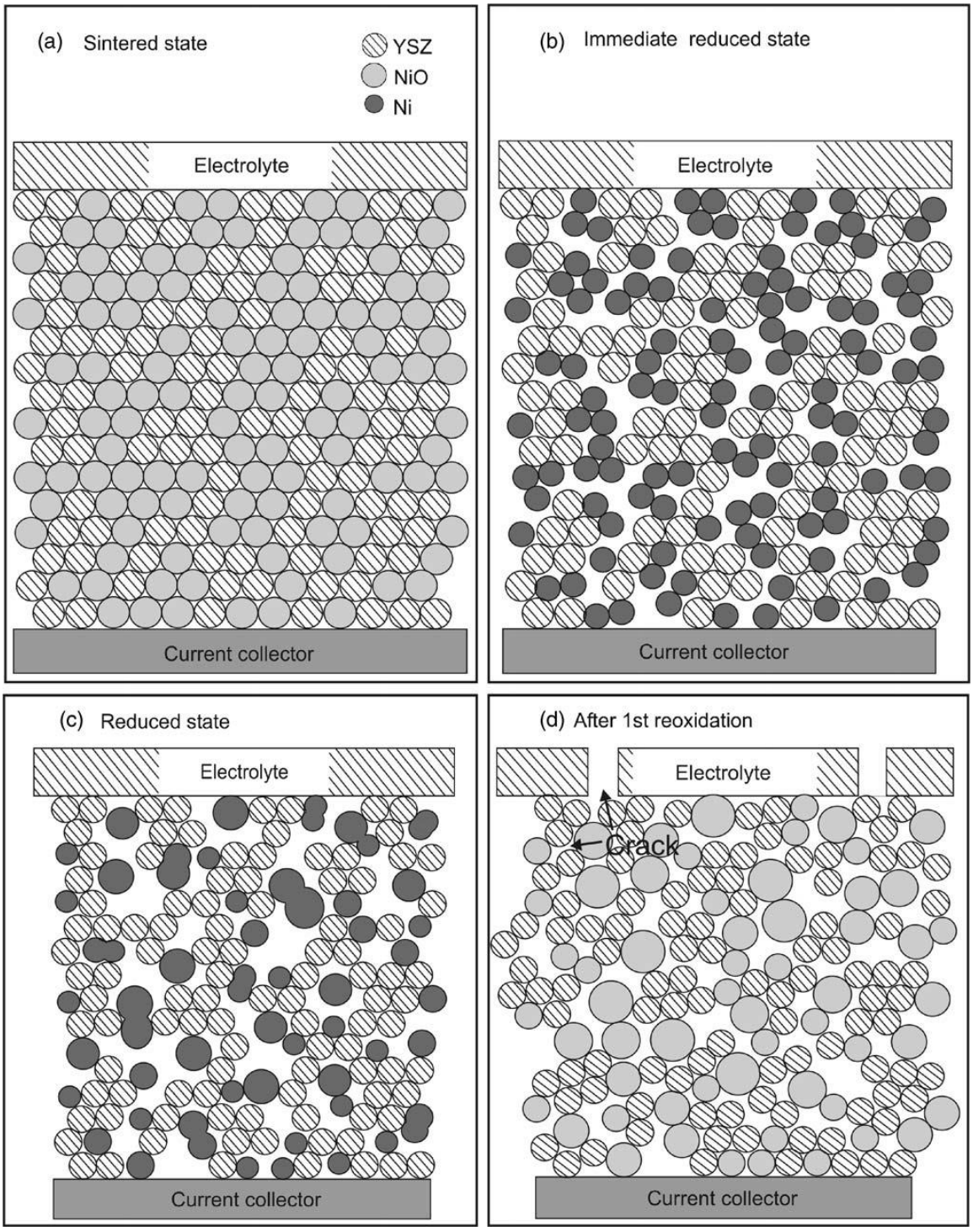

Figure 6.Model illustrating the redox mechanism in the Ni-YSZ cermet anode: a) the sintered state, b) long-term reduced state, c) the reoxidized state, d) crack formation in the cermet [28].

2.2.4 Electrode kinetics

Infiltration on the anode improves the electrode kinetics by increasing TPB density. The liquid precursor solutions are infiltrated and wet the substrate surface. After drying and decomposition, the nanostructured phases are formed *in-situ* at temperatures as low as 500°C, creating significantly more TPBs shown in Figure 7 [31]. Such features cannot be incorporated during a typical SOFC fabrication process, which requires sintering temperatures in excess of 1300°C, during which significant coarsening of any nanoscale microstructure would occur [32,33]. Bertei et al. used numerical modeling to reconstruct an infiltrated electrode showing that the infiltration of nanosized catalysts can increase the TPB density by two orders of magnitude compared to a conventional composite electrode [34]. Skafte et al. infiltrated GDC into Ni-YSZ cermet anodes, showing improvement in initial cell performance after both GDC infiltration and simultaneous infiltration of GDC and Cu nanoparticles. The addition of Cu substantially increased cell performance over the cell with only GDC, suggesting that simultaneous infiltration of metallic nanoparticles with a MIEC can greatly improve the charge transfer kinetics of Ni-YSZ cermet anodes [35].

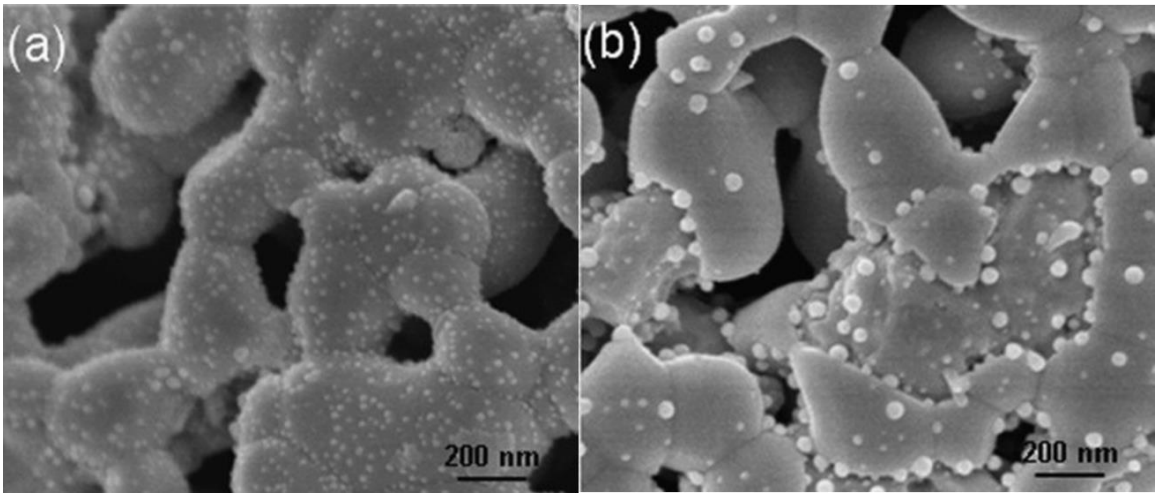

Figure 7. Scanning electron micrographs of Pd-impregnated $La_{0.75}Sr_{0.25}Cr_{0.5}Mn0.5O_{3-\delta}$/YSZ composite anodes a) before and b) after testing at 800°C in methane [31].

2.2.5 Objective of this work

The objective of this work is to improve intermediate temperature performance of commercial Ni-YSZ cermet anode supported SOFCs by liquid infiltration. This dissertation is divided into three major topics: i) improving the electrochemical performance of Ni-YSZ cermet anodes by infiltrating Ni nanoparticles, ii) co-infiltration of Ni and a MIEC in Ni-YSZ cermet anodes to improve stability and utilization of the nanoparticles over a longer time period, and iii) detailed study on effects of infiltration of Ni, GDC, and Ni-GDC in Ni-YSZ cermet anodes. This detailed study includes:

1. microstructural characterization of commercial Ni-YSZ anodes,
2. preparation of infiltration solutions and powder characterization,
3. microstructural characterization of infiltrated particles,
4. study of the stability of the infiltrated microstructure, and
5. electrochemical testing of uninfiltrated and infiltrated cells.

3. Infiltration of Ni nanoparticles

3.1 Introduction

As mentioned in the previous chapter, liquid phase infiltration of catalysts into porous ceramic substrates is commonly used in SOFC electrodes and it is attractive due to its simplicity and low additional cost. Ni nanoparticles can be infiltrated into an anode ceramic scaffold, which is itself an ionic conductor or a MIEC. When a purely ionic conducting scaffold is used, the infiltrated Ni nanoparticles must form a connected network to provide a pathway for electron conduction in the anode. It has been reported that this approach has many advantages, including: significant reduction in the molar fraction of Ni needed, enhanced tolerance to redox cycling, and very fine feature sizes of the deposited Ni [36–44]. The fine feature sizes of infiltrated Ni networks are often on the order of 0.1-1μm, creating a high TPB density of 10-30 μm μm^{-3} [36,45]. This higher density of electrochemically active reaction sites leads to an improved initial performance of the SOFC [41]. However, the performance of infiltrated Ni anodes drops quickly during operation, often within the first few days of exposure to high temperature. This has been attributed to the rapid coarsening of the infiltrated Ni nanoparticles [43,44,46,47].

In comparison, traditional Ni-YSZ cermets (formed by tape casting layers of mixed NiO and YSZ particles and then laminating layers to the desired thickness) have stable performance over long periods of operation [48,49]. However, the catalytic performance of traditional anodes is lower than the initial performance of the infiltrated Ni electrodes, because tape cast cermets have Ni particles that are on the order of 1 μm, leading to TPB

densities between 1-10 μm μm^{-3} [50–54]. The poorer catalytic performance of tape cast anodes are exacerbated at lower temperatures, where the electrode charge transfer kinetics are slower [39,53–56]. Liquid infiltration of tape cast Ni-YSZ cermets combines the benefits of long-term stability of Ni-YSZ cermets, and the high catalytic activity of Ni infiltration. Various other more complex methods have been attempted to stabilize infiltrated Ni structures, usually involving co-infiltration of an oxide phase [42,57]. However, the behavior of simple Ni infiltrated Ni-YSZ anodes have not been fully investigated, and is the subject of this study. The stability of the infiltrated Ni nanoparticles and their impact on electrochemical performance at 800°C, 700°C, and 600°C was observed using a new quantitative method based on image analysis of fracture cross sections. The performance (as measured by the I-V characteristics) of the Ni-infiltrated cells was compared to that of uninfiltrated cells at different temperatures.

3.2 Factors affecting anode polarization

By comparing the performance of cells with infiltrated anodes to identical cells without anode infiltration, any changes in cell performance can be directly attributed to changes in anodic contributions to the overall cell polarization. Anode polarization losses can be separated into two components: anodic concentration polarization due to resistance of mass transfer through pores, and anodic activation polarization due to the charge transfer resistance at electrochemical reaction sites. Anode infiltration will impact both these components.

Anode infiltration with Ni nanoparticles is expected to increase anodic concentration

polarization because the volume fraction of pores in the anode is being traded for additional Ni volume fraction. The slight reduction in the size of pores will decrease both the molecular gas diffusivity as well as the Knudsen gas diffusivity. Gas diffusion in SOFC anodes can be modeled using the Dusty Gas Model, which includes both molecular and Knudsen diffusion [54,58–60]. Qualitatively, it is clear that decreasing molecular and Knudsen diffusion rates will increase anodic mass transfer resistance. This is the most immediately obvious negative impact of anode infiltration.

The quantification of the positive effect of liquid infiltration on anodic activation polarization is not as straightforward. Activation polarization in SOFCs is usually modeled by the Butler-Volmer equation [53,54,59,61]. This approach does not provide a first-principle methodology to connect cell microstructure with electrochemical performance. It has been experimentally observed that increased catalytic site density (TPB length) reduces activation polarization in the anode [51]. This simple explanation is adequate for this study because no new materials with potentially different characteristics are being introduced. Introducing Ni nanoparticles in a Ni-YSZ anode increases the electrochemical reaction site density for the same set of anode materials for the infiltrated and uninfiltrated cells. Finally, the temperature dependence of anodic activation polarization is much stronger than that of anode concentration polarization. Thus, the relative importance of the two anodic components of the overall cell polarization will vary significantly with changing temperature.

3.3 Materials and methods

3.3.1 Infiltration of button cells

Button cells were purchased from Materials and Systems Research, Incorporated (MSRI, Salt Lake City, UT). The cells comprised of an 800 µm thick, 2.74 cm diameter NiO-YSZ anode current collector layer (ACCL), a more finely structured 10 µm thick NiO-YSZ anode active layer (AAL), a 8 µm thick dense YSZ electrolyte, a 15 µm thick and 1.70 cm diameter LSM-YSZ cathode active layer (CAL), and a 40 µm thick LSM cathode current collector layer (CCCL). The electrochemically active area of the cell, determined here by the cathode diameter, was 2.275 cm^2. The schematic of the MRSI cell configuration is shown in Figure 8.

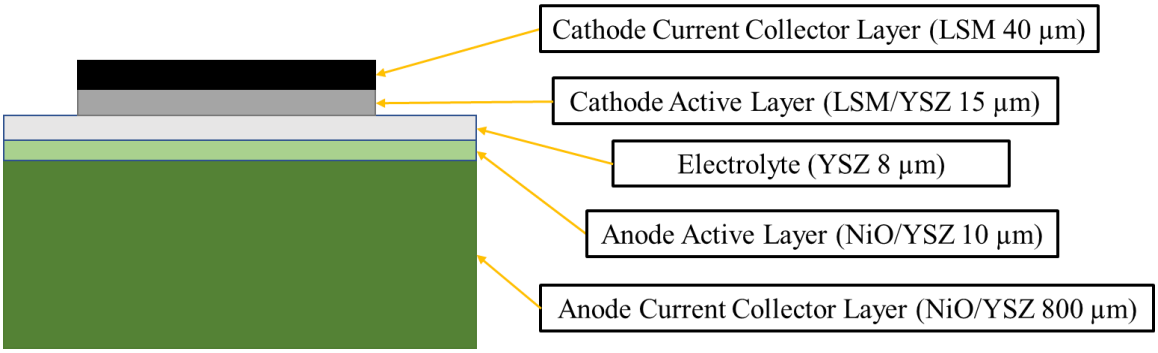

Figure 8. The schematic of the MRSI cell configuration.

All cells were prepared for infiltration and testing by pre-reducing the NiO-YSZ anode to Ni-YSZ. To reduce the anode, cells were mounted between two alumina tubes and protected using mica gaskets, with light spring load on the alumina tubes to ensure good contact between the tubes and cell. The assembly was placed in a tube furnace and heated to 800°C at 1°C min^{-1} with air flowing at 1000 sccm on the cathode side. After

equilibrating for 30 minutes at 800°C, forming gas (95% Ar – 5% H_2) was introduced on the anode side at 300 sccm for 12 hours, with air continuing to flow on the cathode side. The cell is then cooled at 1°C min^{-1} with gas flowing continuing on both sides.

The Ni-YSZ anodes were infiltrated using repeated cycles of vacuum impregnation of an aqueous Ni nitrate solution followed by drying and decomposition of $Ni(NO_3)_2$ to NiO at higher temperature. The aqueous 4M $Ni(NO_3)_2$ solution was prepared by mixing 23 g Ni nitrate (Chemsavers, 99.9%+), 1.8 ml Triton-X 100 surfactant (Talas), and 20 ml distilled water at 90°C. The solution was impregnated into the reduced anode in a vacuum flask at 5 mbar absolute pressure. The schematic of the liquid impregnation apparatus is shown in Figure 9. Excess liquid on the surface of the anode was wiped off to avoid blocking pores for the next round of infiltration. The infiltrated cell was heated to 100 °C at 2°C min^{-1} and held for 20 minutes to evaporate the water, then heated to 320°C at 2°C min^{-1} and held for 20 minutes to decompose the infiltrated $Ni(NO_3)_2$ to NiO. For cells used in this study, the above infiltration procedure was repeated five times.

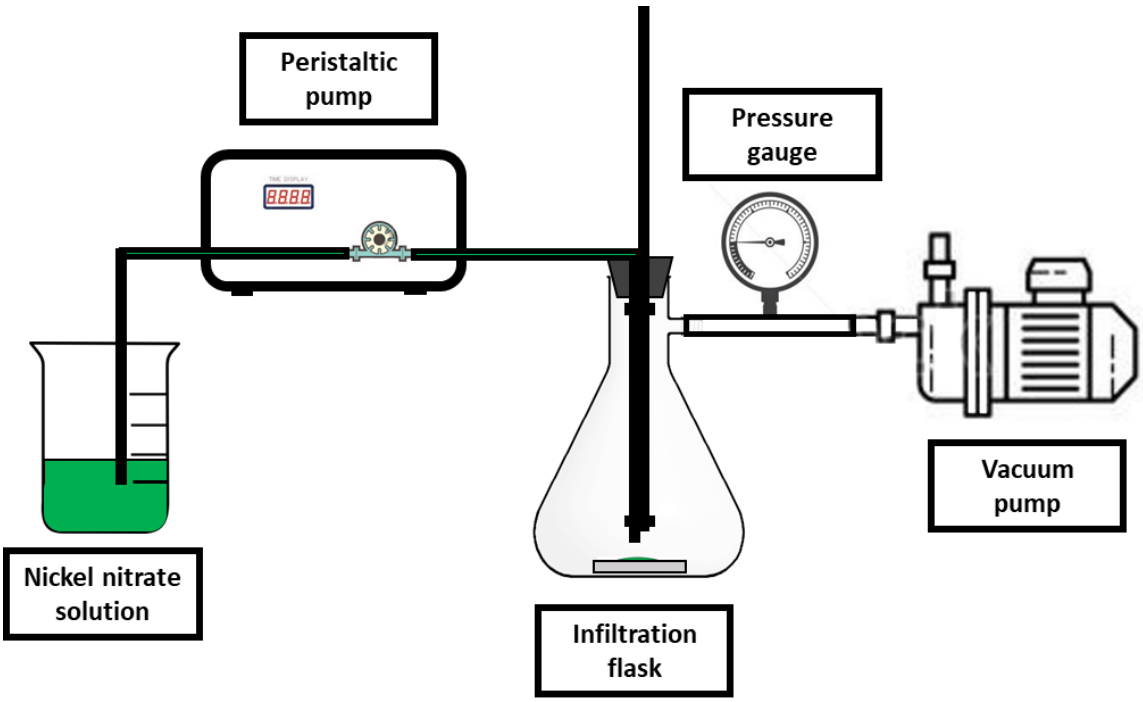

Figure 9. The schematic of the liquid impregnation apparatus.

3.3.2 Electrochemical testing[1]

To prepare for testing, metallic meshes were attached to the electrodes for use as electrical contacts using conductive inks. A nickel mesh current collector (Alfa Aesar, 99.5%) with nickel lead wires (Alfa Aesar, 99.5%) was adhered to the anode using nickel ink (Fuel Cell Materials). A silver mesh current collector (Alfa Aesar, 99.9%) with silver lead wires (Alfa Aesar, 99.9%) was adhered to the cathode using silver ink (Alfa Aesar). The cell was then loaded into the electrochemical test stand, shown schematically in Figure 10, between an Al_2O_3 tube and a machined Al_2O_3 plate with mica gaskets above and below the cell. A K-type thermocouple was fed inside the cathode side gas inlet tube to measure cell temperature during testing. The whole assembly was then compressed

[1] Electrochemical testing was carried out by Paul Gasper.

between the aluminum end plates using springs attached to the Al_2O_3 alignment rods on both the cathode and anode sides. A sealing glass paste (Fuel Cell Store) was applied around the edges of the cell to ensure a complete gas seal.

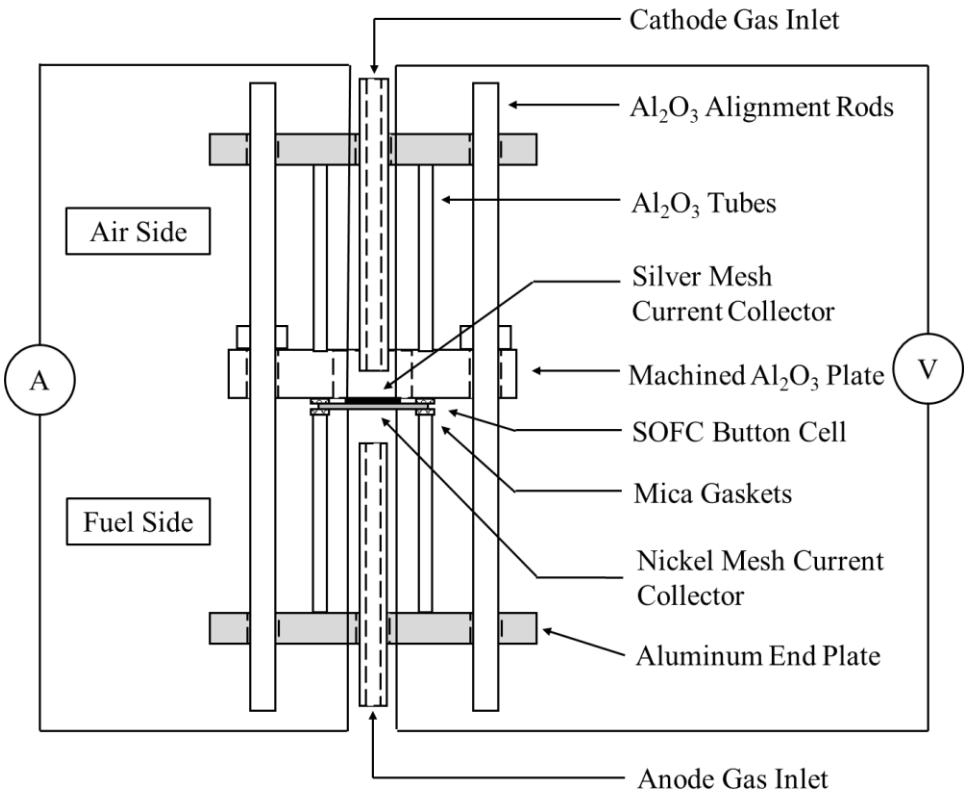

Figure 10. Schematic of the electrochemical testing stand.

The assembly was heated to 850°C at 1°C min^{-1} with forming gas flowing on the anode side at 300 sccm and air flowing on the cathode side at 1000 sccm. The furnace was held at 850°C for 12 hours to cure the glass paste, and then brought to the 800°C at 1°C min^{-1}. Cells were tested using a Parstat 2273A potentiostat and impedance analyzer (Ametek, Inc.) with a Kepco power booster. Cells underwent an electrochemical pretest procedure with 3% H_2O – 97% H_2 flowing on the anode side at 300 sccm and 1000 sccm

of air flowing on the cathode side. Electrochemical pretesting involved monitoring the open circuit voltage for 24 hours to ensure good sealing, and applying galvanostatic current of 0.5 A cm^{-2} for 24 hours to stabilize cell performance. Before measuring performance with dry air on the cathode, a 'nickel spreading procedure' [62] was conducted using I-V scans at 800°C with 100% O_2 on the cathode and 97% H2 – 3% H_2O on the anode. During these scans, cells were tested down to 400 mV at 800°C, which is in a regime where the limiting current density had been reached. This procedure is necessary to spread the Ni nanoparticles and connect them, thereby providing an electronic pathway between the Ni nanoparticles, and activating the new TPBs [62]. Stable cell performance was verified by three repeated identical I-V scans. All I-V scans were conducted galvanodynamically at a rate of 5 mA s^{-1}.

After performance stability was verified, the partial pressures of H_2O and H_2 in the H_2–H_2O gas mixtures were varied on the anode side to simulate cell performance at higher fuel utilization conditions. Hydrogen was humidified using a heated water bath. Gas lines downstream from the heated bath were heated to 130°C using rubber heat tape to prevent condensation of water. The partial pressure of water vapor was increased by heating the water bath while varying hydrogen flow to maintain a constant molar flow rate of the H_2–H_2O gas mixture. Fuel humidity was monitored using the cell OCV, as predetermined by the Nernst equation at different H_2–H_2O gas mixtures. I-V scans were conducted after the cell OCV values were stable at desired levels of fuel humidity.

In the case of multiple testing temperatures, the anode gas mix was returned to 3% H_2O – 97% H_2, held at OCV to stabilize for 6 hours, and then ramped to the new testing

temperature at 1°C min^{-1}. Stable cell performance was again verified using three repeated I-V scans, and then $p_{H_2O} - p_{H_2}$ variation was conducted. After electrochemical testing was completed, the cell was cooled to room temperature at 1°C min^{-1} under humidified hydrogen flow on the anode side and air flow on the cathode side to preserve the microstructure for post-test characterization.

Table 2 shows the nomenclature of the electrochemically tested cells. One uninfiltrated cell was sequentially tested at 800°C, 700°C and 600°C. Two other cells were liquid infiltrated (Infiltrated Cell 1 and Infiltrated Cell 2) with Ni nanoparticles. Infiltrated Cell 1 was tested at 800°C, while Infiltrated Cell 2 was tested sequentially at 700°C and 600°C. This was done to examine the impact of testing temperature on infiltrated Ni nanoparticle morphology.

Table 2. Nomenclature and electrochemical testing temperatures for uninfiltrated and infiltrated cells. Infiltrated cells 1 and 2 were prepared identically but were tested separately to examine the effect of temperature on the microstructure.

Test Temperature	**Cell Nomenclature**		
	Uninfiltrated Cell	**Infiltrated Cell 1**	**Infiltrated Cell 2**
800°C	X	X	
700°C	X		X
600°C	X		X

3.3.3 Microstructural characterization

Relevant microstructural parameters of the Ni-YSZ cermet anode, such as volume fraction of each phase, grain size of each phase, and triple phase boundary of the AAL were determined utilizing focused ion beam (FIB) sectioning and imaging of the cross

section using scanning electron microscopy (SEM). Many cross sections were taken and used to digitally reconstruct a 3-dimensional model of the anode, enabling quantitative measurement of the microstructural parameters, the exact details of which have been described previously by other researchers [48,52,63].

To prepare for FIB/SEM based 3-D reconstruction, a reduced cell was fractured between glass slides and its cross section was infiltrated with M-bond 610 epoxy (Agar) to maintain microstructural integrity during FIB sectioning. Since the AAL is the region of most electrochemical activity in the anode, this layer was chosen as the 'region of interest' (ROI) for characterization. A 1 μm thick carbon protective coating (deposited by 108C Auto, Ted Pella) followed by a 1 μm thick Au/Pd (deposited by 108 Manual Sputter, Ted Pella) were deposited on top of the ROI to avoid charging and beam drift bias during FIB milling.

The sequential FIB milling and SEM imaging was conducted using a FEI Quanta 3D FEG equipped with a channel detection electron multiplier detector and energy dispersive x-ray (EDX) detector. A 3 nA milling current and a 30kV acceleration voltage were used for FIB milling. The configuration of the sample in relation to the FIB and SEM electron beam is shown in Figure 11a. Two trenches were milled perpendicular to the face of the ROI on each side to mitigate shadowing effects and to avoid milling debris from redepositing on the ROI [64,65]. Figure 12 shows two examples of the FIB milling process with and without trenches, respectively, to demonstrate the shadowing effects. An 'X' shaped marker was cut through the electrolyte along the z-axis to enable image alignment. The 'cut and see' technique was used for capturing sequential images. A set of

200 SEM images of the ROI was taken at an acceleration voltage of 2kV for 3D reconstruction. The low acceleration voltage for SEM imaging was chosen to enhance contrast between the Ni and YSZ phases. The sample size and voxel size used in the procedure are listed in Table 3.

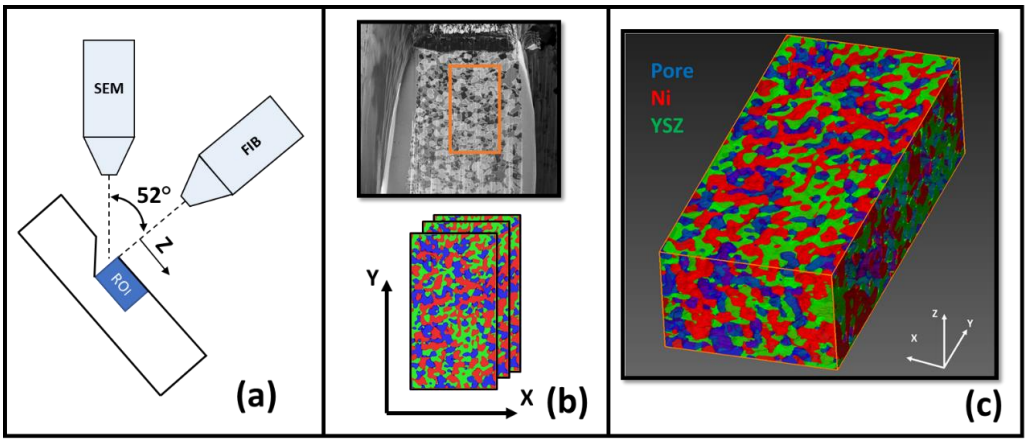

Figure 11. a) Configuration of FIB/SEM 'cut and see' technique. b) Examples of image acquisition and phase separation. c) 3D reconstruction of ROI.

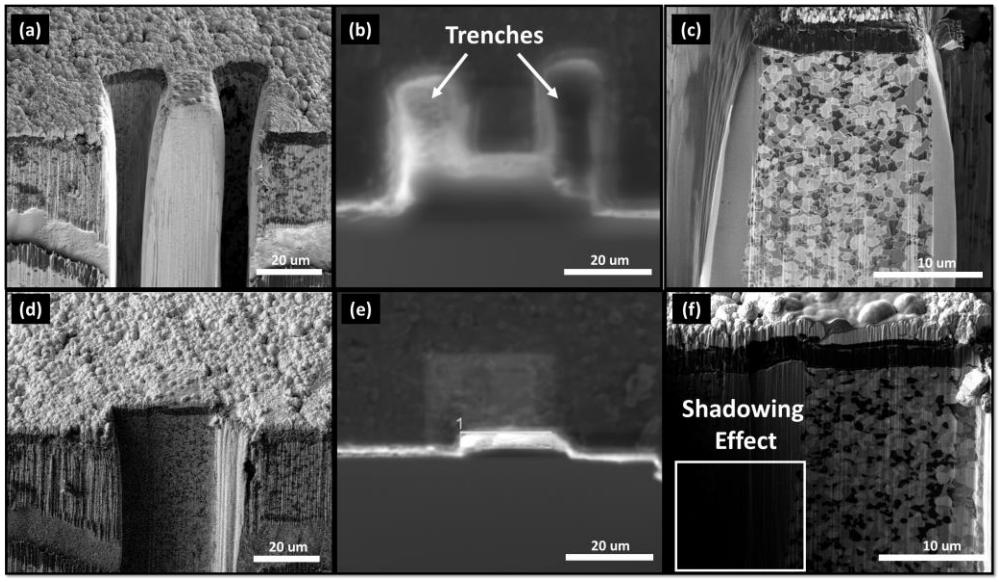

Figure 12. An example of the FIB milling process with trenches showing a) a front view of the ROI, b) a top view of the ROI, and c) a zoom-in view of the ROI. An example of the FIB milling process without trenches showing d) a front view of the ROI, e) a top view of the ROI, and f) a zoom-in view of the ROI highlighting the shadowing effect.

Table 3. Sample size and voxel size used for 3D reconstruction.

Axis	X	Y	Z
Sample size (μm)	10.29	23.11	6.40
Voxel size (nm)	29.14	36.98	32.00

The microstructure of the anode active layer was reconstructed by using Avizo 3D (ThermoFisher Scientific Inc.) [38,48,52]. Ni, YSZ, and pore phases appeared as light gray, dark gray and black regions, respectively, as shown in Figure 11b. Phase separation was based on these different gray levels, classified by Avizo's Interactive Thresholding module. Figure 13 shows an example of phase separation based on the intensity of gray levels.

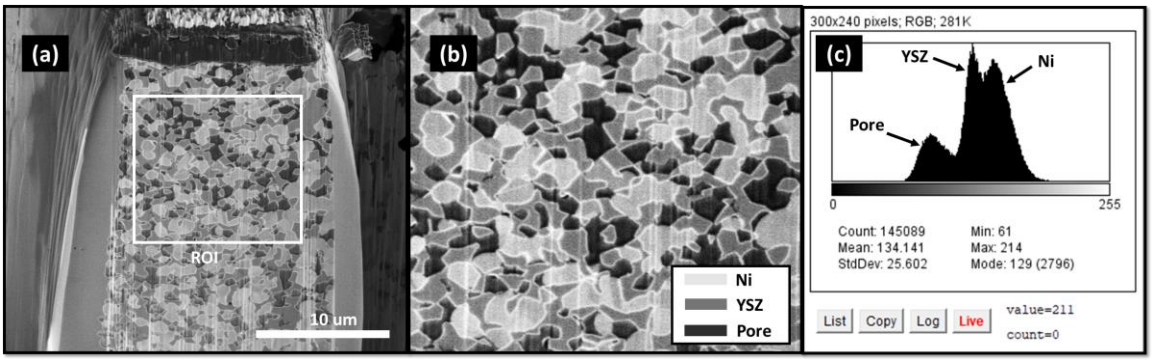

Figure 13. An example of phase separation based on the intensity of gray levels. a) The ROI for phase separation. b) The zoom-in view of the ROI showing three phases with corresponding grayscale colors. c) The histogram of the ROI to show the intensity peaks of three phases.

The TPB length in the 3D reconstruction of the Ni-YSZ cermet was calculated using the volume expansion method developed by Iwai et al [63]. The TPBs are lines in the 3D field. By expanding each phase outward by one voxel, the overlapped volumes are tube-like shapes and contain TPB lines inside. The length of the centerlines of the overlapped

volumes are characterized as the TPB length. The schematic of the volume expansion method is shown in Figure 14.

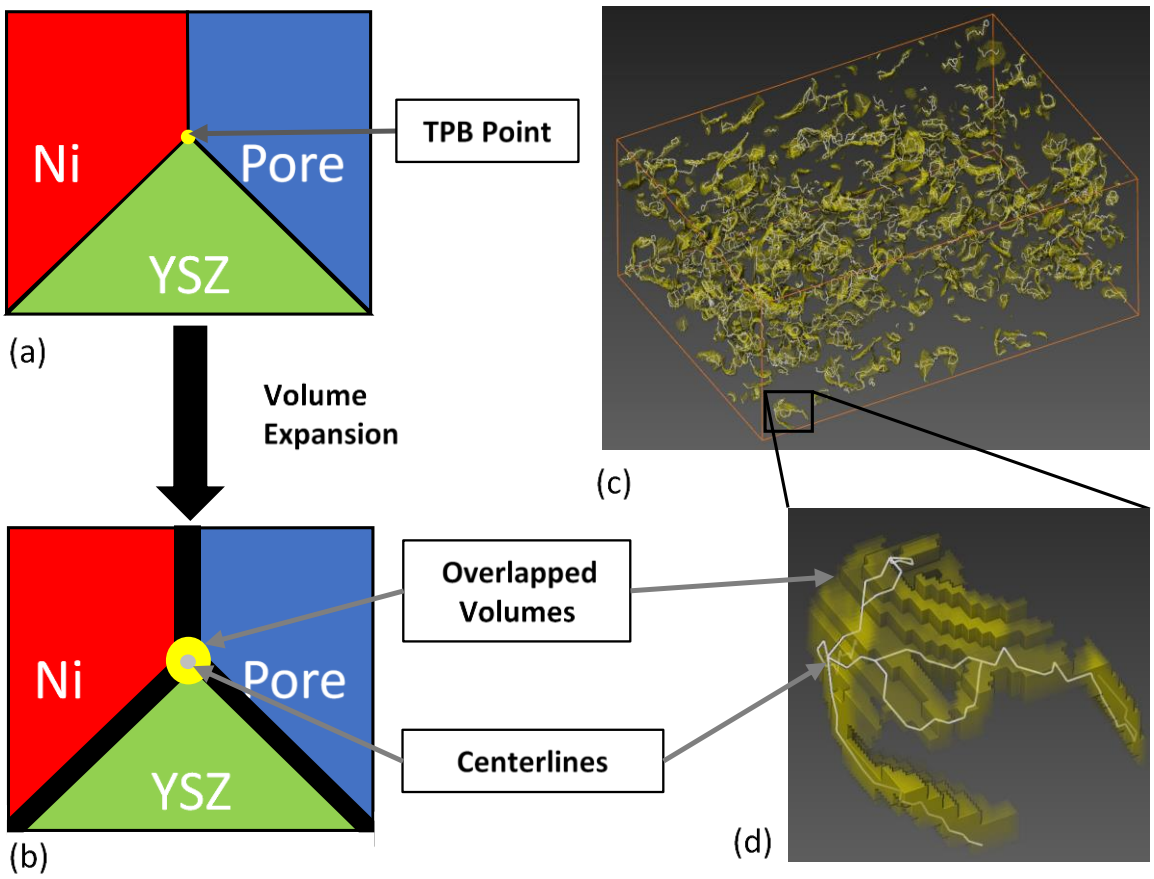

Figure 14.The schematic of the volume expansion method. a) A 2D schematic of the interaction point (TPB point) shared by three phases. b) A 2D schematic of the overlapped volumes with its centerline after volume expansion. c) A 3D reconstruction of the overlapped volumes. d) The zoom-in view of the overlapped volumes with the centerlines.

The Ni nanoparticles were characterized by SEM and EDX. Cells were fractured between glass slides and imaged using an SEM to observe infiltrated nanoparticles throughout the anode. The number of particles per unit area (# μm^{-2}) (referred hereto as the areal particle density) and particle size (nm) were measured by manually circling particles from a ROI using image editing software, and separating circled particles from

the rest of the image using Avizo 3D. The particle size, as measured by calculating the hydraulic diameter of each manually circled particle, and the areal particle density of the SEM micrograph were calculated using Avizo 3D. This process is shown in Figure 15. EDX elemental mapping was used to verify that deposited particles were indeed nickel and to determine the phase on which the particles were deposited on. Nanoparticle shape and contact angle were estimated by changing the sample tilt angle in the SEM after carefully choosing a ROI that revealed the particle morphology.

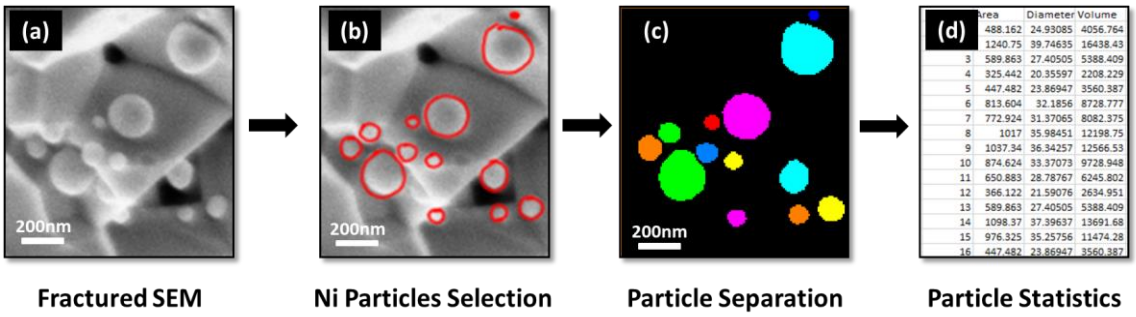

Figure 15. The schematic of the process to obtain particle statistics. a) A fractured SEM image of Ni nanoparticles. b) The image after circling Ni nanoparticles. c) Ni nanoparticle separation by using Avizo 3D. d) Obtaining particle statistics by using Avizo 3D.

3.4 Results and discussion

The results of the microstructural characterization of the Ni-YSZ anode substrate are listed below in Table 4. The volume fractions of each phase as determined by 3D reconstruction as well as the TPB density measured by the volume expansion method in this study are consistent with reported values for Ni-YSZ cermets [48–52]. The TPB density of the Ni-YSZ cermet backbone provides a baseline value for additional TPB length introduced by liquid infiltration of Ni nanoparticles.

Table 4. Characteristics of anode active layer microstructure from 3D reconstruction of the uninfiltrated sample.

Phase	Volume (μm^3)	Volume Fraction	TPB density ($\mu m\ \mu m^{-3}$)
Nickel	591	38.8%	2.39
YSZ	495	32.5%	
Pores	437	28.7%	

Figure 16 shows the accumulated Ni weight gain of an infiltrated cell after each infiltration cycle, measured after the decomposition of $Ni(NO_3)_2$. Since the efficacy of the infiltration decreased after each cycle, 5 infiltration cycles were chosen as the deposition process for each sample. This led to approximately 6 wt% increase of the overall Ni content due to the additional NiO deposited by infiltration.

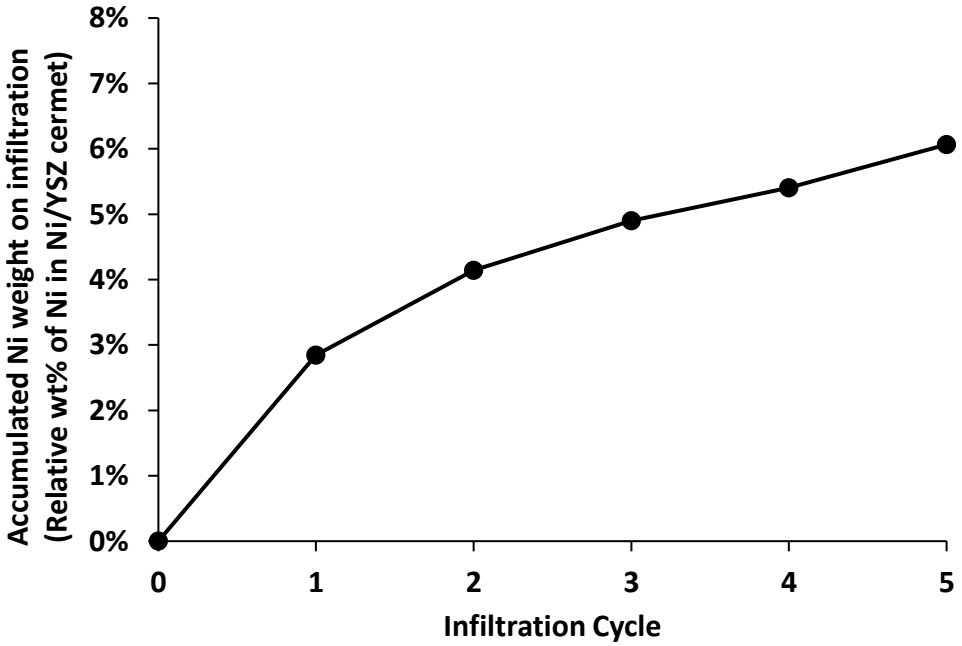

Figure 16. Plot of accumulated nickel weight due to NiO deposition after each infiltration cycle, normalized to the weight of nickel within the uninfiltrated anode.

After the fifth infiltration cycle, the deposited NiO was reduced to Ni under flowing H_2 at 800°C. Figure 17 shows SEM micrographs of a representative AAL before and after the infiltration procedure. The infiltrated Ni nanoparticles can be easily distinguished by their round shapes. A qualitative inspection of SEM images of five different areas distributed radially across the AAL and five different areas through the depth of the anode current collecting layer revealed homogenous deposition of Ni nanoparticles throughout the anode. Most importantly, uniform deposition throughout the AAL shows that the liquid infiltration solution can penetrate the fine pore structure of this layer and reach the electrode/electrolyte interface. Successful deposition of Ni nanoparticles at the electrode/electrolyte interface is critical for improving anodic charge transfer.

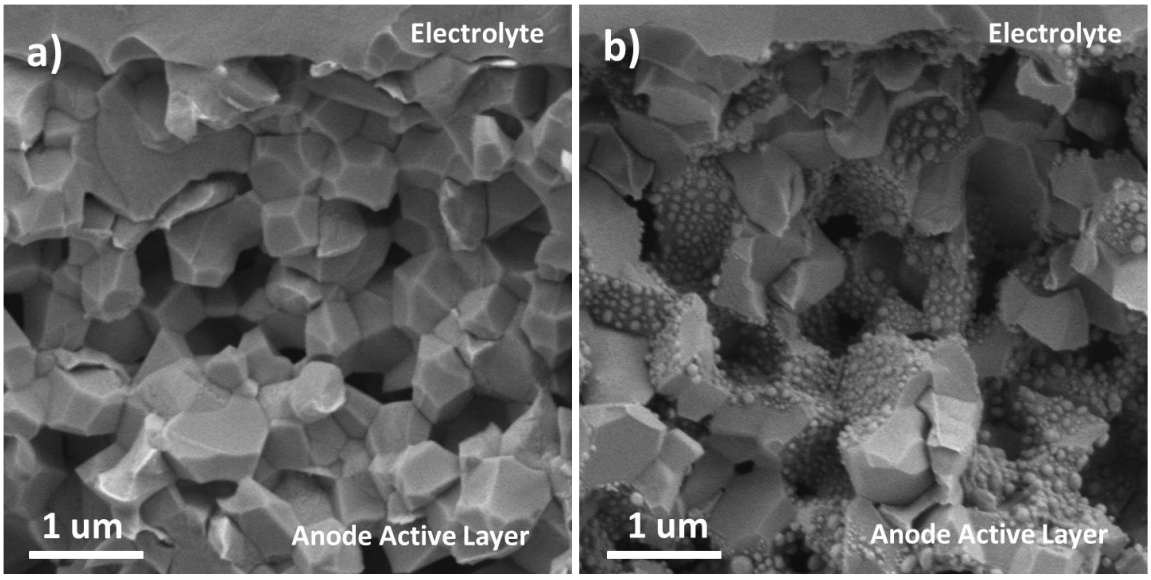

Figure 17. Microstructure of the anode active layer a) before infiltration and b) after the infiltration procedure and reduction of infiltrated NiO to Ni at 800°C under dry forming gas.

Figure 18a shows a high magnification secondary electron SEM micrograph of the AAL of an infiltrated sample, with the EDX elemental maps of Ni and Zr superimposed in Figure 18b. Figure 18b confirms that the rounded particles are indeed Ni. Interestingly, Figure 18b shows that the rounded Ni nanoparticles are exclusively observed on the YSZ phase. It is speculated that any Ni deposition on the Ni phase would provide continuous coverage, and thus be unobservable. In order to accurately calculate the increased TPB length due to infiltration, the particle shape and the contact angle between the particles and YSZ substrate need to be known. The particle morphology and contact angle was obtained by tilting the sample appropriately. Figure 18c shows some of the nanoparticles at the appropriate tilt before electrochemical testing, indicating that the assumption of a hemispherical shape with a 90° contact angle is a reasonable estimation. Figure 18d shows a similar image from Infiltrated Cell 1, showing no substantial change in Ni-YSZ contact angle after electrochemical testing at 800°C.

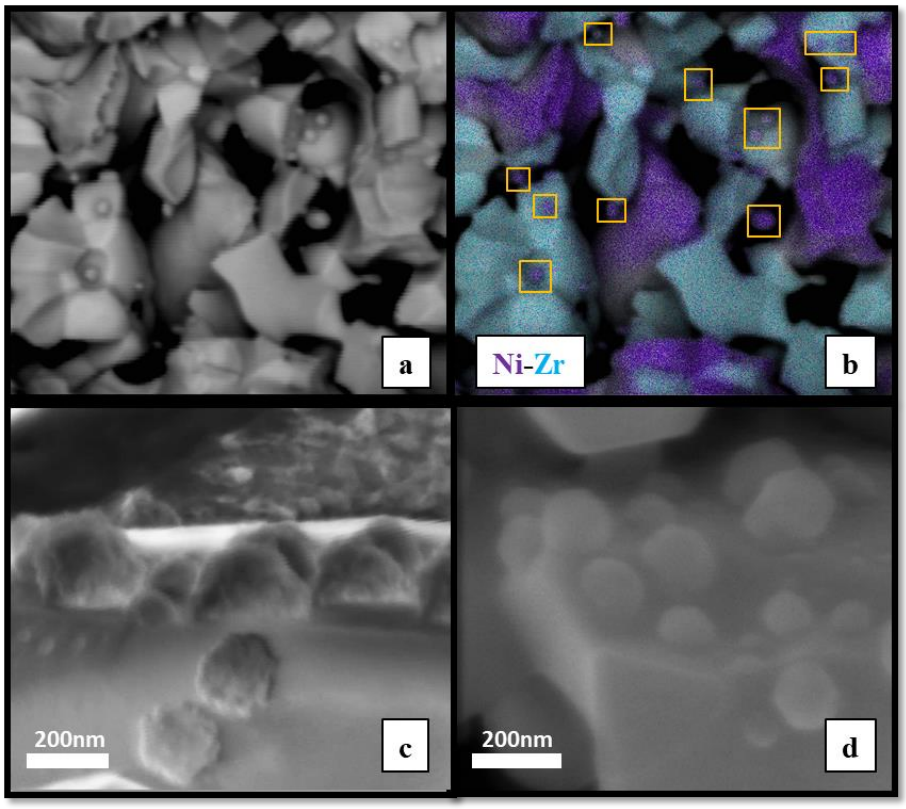

Figure 18. a) Secondary electron SEM micrograph of fracture cross-section of an infiltrated AAL showing rounded infiltrated Ni nanoparticles. b) EDX elemental maps of Ni and Zr, showing that the rounded particles (marked by rectangles) are indeed Ni and are present preferentially on the YSZ phase. c) and d) SEM images of particle morphology viewed at the appropriate sample tilt angle of c) an as-infiltrated cell, and d) Infiltrated Cell 1 after electrochemical testing.

Assuming that all particles are hemispherical in shape with a 90° contact angle, the increased TPB density is simply the summation of the perimeters of nanoparticles. This increased TPB density of anode active layer (μm μm^{-3}) as a result of infiltration (TPB_{inf}) can thus be calculated as:

$$TPB_{inf} = n\pi\bar{d}\left(\frac{S}{V}\right)v, \tag{1}$$

where n is the areal particle density (# μm^{-2}) of particles and $\bar{d}$ is the average nanoparticle diameter, (S/V) is the ratio of the pore surface area to the pore volume (μm^2

μm^{-3}), and v the pore volume fraction. The quantities, n and $\bar{d}$, can be quantified from the SEM observations, while (S/V) and v can be calculated from the 3D reconstruction of FIB-SEM data. The statistical results of microstructural characterization in the AAL of an un-infiltrated as well as an infiltrated but untested cell are in Figure 19. The figure shows that infiltration increases the AAL TPB density by approximately a factor of four (from 2.39 $\mu m\ \mu m^{-3}$ to 8.38 $\mu m\ \mu m^{-3}$).

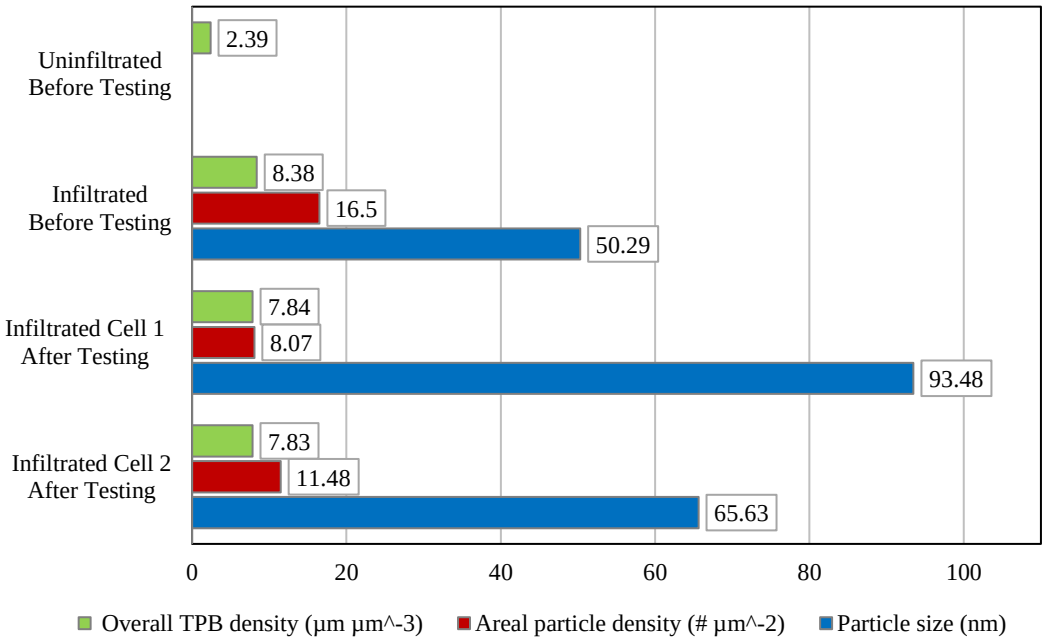

Figure 19. Nanoparticle statistics (TPB length, areal particle density and average particle diameter) of an infiltrated Ni-YSZ cermet anode substrate before and after infiltration, and after electrochemical testing (see Table 2 for description of electrochemical tests).

The calculated additional TPB density assumes that the infiltrated Ni nanoparticles sitting on the YSZ grains are percolating, and thus the additional TPBs formed due to the Ni nanoparticles participate in the electrochemical reaction. Bertei et al [34] discusses the

microstructural modeling of an infiltrating electronic conducting phase on a composite backbone. Even 20% of surface coverage fraction of electronic conducting phase leads to triple the overall TPB density. The surface coverage of the infiltrated nanoparticles on YSZ phase before testing the cell is 17.8%, which can likely account for the overall performance improvement.

However, the nanoparticles away from edge between Ni and YSZ grain appear to be non-percolated from SEM cross-sections in Figure 17. Nanoparticles can connect with one another and become percolated during testing due to wetting of Ni on YSZ in the AAL. Ni wetting on YSZ during the application of an electrochemical potential has been documented [66]. Thus, the measurement of Ni nanoparticle TPB density presented here is a useful way to estimate the percolated TPB length of Ni nanoparticles during testing. Other Ni nanoparticle statistics calculated by this method are also useful for characterizing the evolution of infiltrated Ni nanoparticles, in a more thorough manner than a visual comparison.

Electrochemical testing shows performance improvement of infiltrated cells at different temperatures (800°C, 700°C and 600°C) and anode gas compositions (3% H_2O – 97% H_2, 50% H_2O – 50% H_2, 75% H_2O – 25% H_2). The results of the electrochemical tests are summarized in Table 5. Two obvious trends are observed from the results; i.e., the relative performance improvement with infiltration decreases with increasing temperature and increasing water vapor partial pressure in the anode. Comparison of the I-V curves, shown in Figure 20, corroborates this conclusion. At 800°C, Figure 20a, the power density continues to increase until the cell reaches the saturation current density,

after which the polarization increases rapidly, causing a sharp drop in the power density. This suggests that charge transfer kinetics are fast, allowing the cell to reach the steady state mass transfer limit in the electrodes. At 700°C and 600°C, Figure 20b and Figure 20c respectively, the maximum power density occurs much before the saturation current density is reached, implying that the performance is limited by poor charge transfer kinetics. Ni nanoparticle infiltration should mostly impact charge transfer kinetics, and thus has a larger impact on cell performance as the operating temperature is reduced.

Table 5. Uninfiltrated and infiltrated cell performances at varying temperatures and anode gas compositions.

Testing Temperature	**Cell**	**Maximum Power Density (W cm^{-2}) at Different Anode Gas Mixtures**		
		3% H_2O – 97% H_2	**50% H_2O – 50% H_2**	**75% H_2O – 25% H_2**
800°C	Uninfiltrated	1.078	0.701	0.408
	Infiltrated Cell 1	1.281	0.831	0.414
	Change	+18.8%	+18.5%	+1.5%
700°C	Uninfiltrated	0.408	0.335	0.255
	Infiltrated Cell 2	0.606	0.455	0.289
	Change	+48.5%	+35.8%	+13.3%
600°C	Uninfiltrated	0.078	0.068	n/a
	Infiltrated Cell 2	0.123	0.099	n/a
	Change	+57.7%	+45.6%	n/a

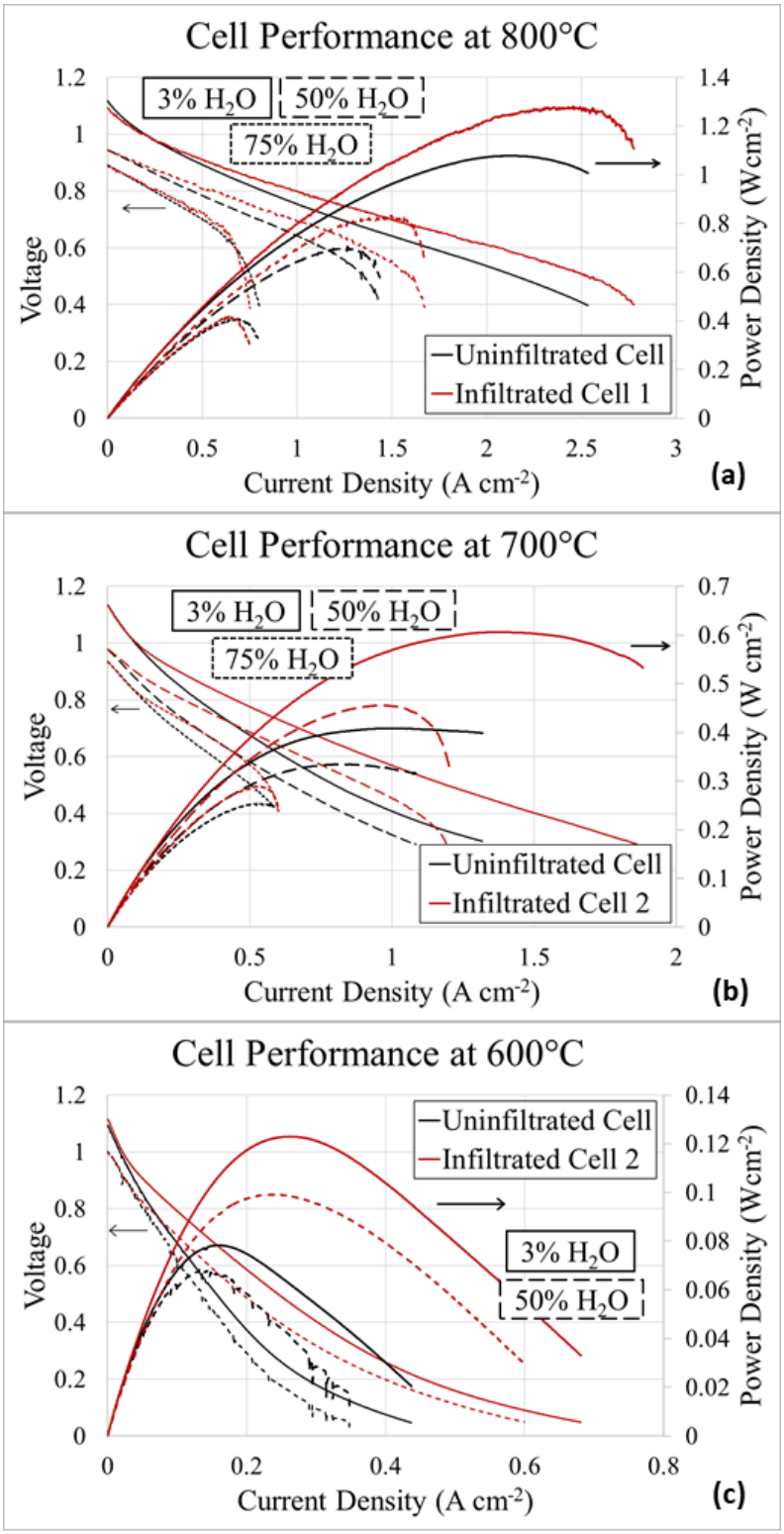

Figure 20. Electrochemical performance data at a) 800°C, b) 700°C, c) 600°C.

The trend of performance improvement decreasing with increasing anode gas humidity requires a different explanation. A simple reason is that the cells do not reach as high current densities in high p_{H_2O} atmospheres compared to those tested in low p_{H_2O} atmospheres, resulting in less polarization difference between the infiltrated and uninfiltrated cells. Qualitatively, it also appears that overall anode polarization is less at higher water vapor pressures, corroborating more detailed examinations of anode reaction kinetics discussed in Chapter 3.2 [53,54,59]. Because the anode polarizations are lower at higher p_{H_2O}, improving anode reaction kinetics will have less effect than at conditions with lower p_{H_2O}.

SEM micrographs of the fracture cross-sections of the two infiltrated cells after electrochemical testing are shown in Figure 21. Figure 21 shows that after testing, Ni nanoparticles are still present in the AAL. The areal particle density, average particle diameter, and the TPB length in the infiltrated cells after electrochemical testing are listed in Figure 19. Figure 19 shows that there is coarsening of the infiltrated Ni nanoparticles and a reduction in the areal particle density after electrochemical testing, with these effects being more pronounced in the Infiltrated 1 cell (tested at 800°C) as compared to the Infiltrated Cell 2 (tested at 700°C and 600°C). However, there is less than a 10% decrease in the calculated TPB densities for both samples as compared to the untested infiltrated cell. After cell testing, the overall TPB length is still significantly larger than the uninfiltrated cell, indicating that beneficial effects of anode infiltration remain. This assumes that infiltrated Ni nanoparticles sitting at the edge of Ni and YSZ grain are percolated, also the isolated nanoparticles on the YSZ grain are percolating during

electrochemical testing because of Ni spreading on YSZ. This Ni spreading may also be the cause of Ni nanoparticle coarsening. The isolated Ni nanoparticles away from the edge are not contributed to electrochemical reactions.

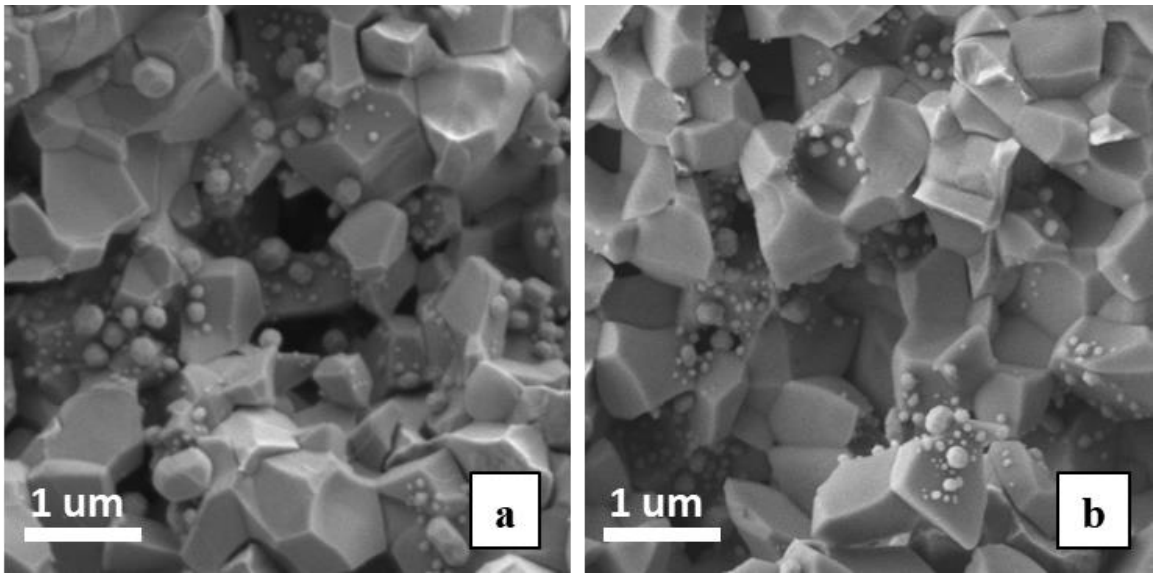

Figure 21. Microstructure of the AAL of (a) Infiltrated Cell 1 and (b) Infiltrated Cell 2 after electrochemical testing.

3.5 Conclusions

Liquid phase infiltration of Ni nanoparticles into Ni-YSZ cermet anodes of solid oxide fuel cells increases the electrochemical reaction site density of the anode, resulting in electrochemical performance improvement. In this study, the TPB density in the AAL in a commercially available SOFC was measured using FIB-SEM sectioning and 3D reconstruction. The increase in the TPB density in the anode active layer due to infiltrated Ni nanoparticles was calculated using image analysis of fractured SEM cross sections. Using EDX, it was observed that hemispherical Ni nanoparticles were deposited on the YSZ phase, meaning nanoparticles contribute additional TPBs to the anode. Infiltration

of Ni nanoparticles increased the electrochemical reaction site density by approximately a factor of four, provided the Ni nanoparticles were connected by an electrochemical Ni-spreading procedure prior to testing. Electrochemical testing of uninfiltrated and infiltrated cells at different temperatures and water vapor content of the inlet anode gas mixture showed performance improvement due to increased TPB density due to infiltration. The two major trends from the electrochemical results are that the relative performance improvement due to infiltration increases with decreasing temperature and with decreasing anode p_{H_2O}. Since charge transfer kinetics are strongly dependent on temperature, this suggests that infiltration primarily lowers charge transfer resistance in the anode. The increase in relative performance improvement with decreasing p_{H_2O} is harder to deconvolute. It is speculated that the increased impact could simply be due to the higher maximum current densities when testing at high anode p_{H_2O}, increasing the maximum power densities reached during testing. While liquid infiltration of nanoparticles clearly improves anode performance in Ni-YSZ cermets, stability of infiltrated Ni nanoparticles is still an issue, as some coarsening was observed in the fracture cross sections after electrochemical testing. In addition, it is necessary to electronically connect the isolated Ni nanoparticles away from the edge of Ni and YSZ grain that more TPBs can be activated. The solution of these issues will be explored in the next chapter.

4. Co-infiltration of Ni with a MIEC phase

4.1 Introduction

In the previous chapter, the introduction of the Ni nanoparticles into Ni-YSZ cermet anodes increases TPBs and improves cell performance, especially at lower operating temperatures. However, these infiltrated Ni nanostructures suffer from coarsening after just a few hours of operation. This result also agrees with other SOFC studies [67–69]. In addition, the infiltrated Ni deposits as roughly hemispherical nanoparticles only on the YSZ grains. If these nanoparticles are isolated from one another, they are not electrically connected to the Ni-YSZ cermet, unless the Ni nanoparticle is located directly on a Ni-YSZ cermet TPB. As a result most of the additional TPBs remain inert to (or do not participate in) electrochemical reactions, and thus the advantages of liquid infiltration are not fully utilized [34,70]. In order to address the issues of Ni nanoparticle coarsening and formation of non-active TPBs, simultaneous infiltration of Ni with a MIEC phase was explored. The introduction of an MIEC material into Ni infiltrated Ni-YSZ cermet anodes should both physically constrain the infiltrated Ni nanoparticles to prevent coarsening as well as electrochemically connect the Ni nanoparticles to the Ni-YSZ cermet, thereby improving cell performance and stability of infiltrated Ni nanoparticles.

Two groups of MIEC materials used often in SOFC anodes due to their high conductivity and chemical stability in the anode-operating environment are fluorites and perovskites [71]. Of these two groups, fluorites have high ionic conductivity, while perovskites have high electronic conductivity [12]. GDC ($Gd_{0.1}Ce_{0.9}O_{2-\delta}$) is a good

fluorite candidate for infiltration because it has higher ionic conductivity than YSZ as well as reasonable electronic conductivity at low oxygen partial pressures [4]. Also, a liquid solution of Gd and Ce nitrate salts can be easily infiltrated into Ni-YSZ anodes, and the nitrates can then be decomposed at around 500°C to form GDC nanostructures. Infiltrated GDC nanostructures have been utilized by several researchers and show consistent performance improvement compared to that of YSZ or traditionally sintered electrodes [33,34]. The improvement in cell performance after infiltration of GDC is attributed to the increased ionic conductivity of GDC compared to YSZ, which enables oxygen ions to travel farther away from the electrolyte, increasing the number of electrochemical reaction sites and improving anodic charge transfer [33,72]. Simultaneous infiltration of GDC with metallic nanoparticles has been less studied. Skafte et al. infiltrated GDC into Ni-YSZ cermet anodes, showing improvement in initial cell performance after both GDC infiltration and simultaneous infiltration of GDC and copper nanoparticles [73]. The addition of copper substantially increased cell performance over the cell with only GDC, suggesting that simultaneous infiltration of metallic nanoparticles with an MIEC can greatly improve the charge transfer kinetics of Ni-YSZ cermet anodes [73].

The infiltration of conducting perovskite oxides into Ni-YSZ cermet anodes has not received much research interest. Because of their high electrical conductivity, perovskite oxides have mainly been studied for the development of fully ceramic fuel cell anodes [12,44,74]. For selecting a perovskite composition that is suitable for infiltration into Ni-YSZ anodes, the first consideration is the chemical stability of the material in the anode

operating environment with oxygen partial pressures as low as 10^{-17} Pa at 800°C. Many cobaltite, ferrite, manganite, and nickelate perovskites become unstable at oxygen partial pressures lower than 10^{-2} Pa, 10^{-12} Pa, 10^{-10} Pa, and 10 Pa at 800°C, respectively [75]. However, many chromite, titanate, and vanadate perovskites are suitable for use in SOFC anodes. A chromite perovskite is the most suitable candidate for liquid infiltration because the nitrate precursors of titanium and vanadium are not readily available. For this study, an A-site deficient Ni-doped lanthanum strontium chromite ($La_{0.6}Sr_{0.3}Ni_{0.15}Cr_{0.85}O_{3-\delta}$) (LSNC) was chosen. LSNC has high electrical conductivity in the anode-operating environment, and it has been previously utilized as a material for an all-ceramic anode, exhibiting good electrochemical performance [76]. LSNC cannot be synthesized using the nitrate decomposition process, and the nitrate solution has to be mixed with citric acid to carry out the citric-nitrate auto combustion process as described in the next chapter.

Cells with Ni-YSZ cermet anodes were co-infiltrated with Ni-GDC and Ni-LSNC to study their performance and the stability of the Ni-MIEC nanostructures. The GDC and LSNC phases were utilized both for physically stabilizing the infiltrated Ni nanoparticles as well as electrochemically connecting them to the Ni-YSZ substrate. GDC and LSNC were chosen for their suitability for use in SOFC anodes and to compare the impact of ionic and electronic conductivity of the MIEC phase (primarily ionic for GDC versus primarily electronic for LSNC) and processing technique (nitrate decomposition for GDC versus citric-nitrate auto combustion for LSNC) on cell performance. This study first validated the chemical stability of each material for use in the anode operating environment, then examined the physical stability of the infiltrated

microstructures by exposing infiltrated anodes to 2% H_2 – 98% Ar and 25% H_2 – 75% H_2O gas mixtures at 800°C for 48 hours. The electrochemical performance of Ni-GDC and Ni-LSNC infiltrated Ni-YSZ anodes were evaluated using I-V scans and electrochemical impedance spectroscopy (EIS). Performance measurements were analyzed to determine the relative contributions of the Ni-GDC and Ni-LSNC infiltration to the mass transfer and charge transfer resistances of the electrode. Comparison of the electrode microstructures after testing was used to examine the stability of the infiltrated phases after exposure to electrochemical current.

4.2 Materials and methods

4.2.1 Preparation of infiltration solutions and powder characterization

Ni, Ni-GDC and Ni-LSNC liquid infiltration solutions were synthesized using nickel nitrate ($Ni(NO_3)_2{\cdot}6H_2O$, Chemsavers, USA), gadolinium nitrate ($Gd(NO_3)_3{\cdot}6H_2O$, Alfa Aesar, USA), cerium nitrate ($Ce(NO_3)_3{\cdot}6H_2O$, Alfa Aesar, USA), lanthanum nitrate ($La(NO_3)_2{\cdot}6H_2O$, Sigma-Aldrich, USA), strontium nitrate ($Sr(NO_3)_2$, Sigma-Aldrich, USA), chromium nitrate ($Cr(NO_3)_3{\cdot}9H_2O$, Alfa Aesar, USA), and citric acid ($C_6H_8O_7$, Alfa Aesar, USA). For each solution, stoichiometric amounts of metal nitrates and citric acid were dissolved in ethanol on a hot plate at 70°C while stirring. The compositions of precursor solutions used are listed in Table 6.

To ensure proper formation of the MIEC phases, the liquid infiltration solutions were used to form powders in a container. The phase purity of the MIEC powders can be easily verified by x-ray diffraction (XRD) measurements. The powders were formed

under the same environmental conditions the precursors would encounter for nanoparticle formation in infiltrated cells. Ni-MIEC powders were formed by heating the liquid precursor in air to 320°C. This allows for the formation of GDC and NiO by the nitrate decomposition process for the Ni-GDC case, and for the formation of LSNC and NiO via the citric-nitrate auto-combustion process for the Ni-LSNC case. The NiO is then reduced to Ni by heating it to 800°C while flowing the 2% H_2 – 98% Ar gas mixture at 300 cm^3 min^{-1} and holding at temperature for 8 hours. The phases of the synthesized powders were then characterized by XRD using a D8 DISCOVER X-ray diffractometer (Bruker, USA) with Cu K-α radiation and analyzing the resulting spectra using DIFFRAC.EVA software (Bruker, USA).

Table 6. Details of precursor solutions used in liquid infiltration.

Infiltrant	Formula	Ni to MIEC molar ratio	Synthesis method	Citric acid to MIEC metal cations molar ratio	Metal solution molarity	Rounds of infiltration	Weight gain normalized by cell weight	
							For particle stability testing	For electro-chemical testing
Ni	Ni	N/A	Nitrate decomposition	N/A	4M	1	1.34%	N/A
Ni-GDC	Ni - $Gd_{0.1}Ce_{0.9}O_{2-\delta}$	1:1	Nitrate decomposition	N/A	4M	1	1.33%	1.24%
Ni-LSNC	Ni - $La_{0.6}Sr_{0.3}Ni_{0.15}Cr_{0.85}O_{3-\delta}$	1.5:1	Citrate-nitrate auto-combustion	3:1	1M	5	1.88%	1.91%

4.2.2 Infiltration and microstructural characterization of button cells

Anode-supported SOFC button cells were purchased from SOFCMAN Energy (Ningbo, China). The cells were composed of a 400 μm thick, 3 cm diameter NiO-YSZ

anode bulk layer, a 5 µm thick NiO-YSZ AAL, an 8 µm thick dense YSZ electrolyte, a 15 µm thick and 1.6 cm diameter LSM-YSZ composite cathode active layer, and a 30 µm thick LSM cathode current collector layer. The electrochemically active area of the cell, determined by the cathode diameter, was 2 cm^2.

All cells were prepared for infiltration followed by electrochemical testing by pre-reducing the NiO-YSZ anode to Ni-YSZ. This process opens the pores of the anode, allowing the infiltrant to penetrate all the way through the anode and into the AAL. The procedures for anode pre-reduction and infiltration of the precursor solutions into the anode under vacuum have been detailed in Chapter 3.3.1. After infiltration of the precursor solution, both the Ni-GDC and Ni-LSNC cells were heated up in air to 100°C and held for 20 minutes to evaporate the ethanol, then heated to 320°C and held for 20 minutes to react with the metal nitrate precursors. For the Ni-GDC solution, heating to 320°C in air causes the decomposition of the Gd, Ce, and Ni nitrates into their respective oxides. For the Ni-LSNC solution, heating to 320°C in air causes the decomposition of the Ni nitrate into NiO, and also causes the citric acid and nitrates to combust, forming the LSNC phase.

For initial characterization of the microstructure of infiltrated cells, the infiltrated anodes were heated to 800°C while flowing the 2% H_2 – 98% Ar gas mixture at 300 cm^3 min^{-1} and held at temperature for 1 hours, allowing the Ni-GDC and Ni-LSNC to completely equilibrate to the anode operating environment before returning to room temperature. Cells processed in this way are referred to as ‘as-reduced’. The microstructures of the uninfiltrated, Ni-GDC infiltrated, and Ni-LSNC infiltrated cells

were examined on fractured cross sections of the cells using a field emission Zeiss (Carl Zeiss AG, Germany) SUPRA 55-VP SEM. High spatial resolution images and elemental mapping of the Ni-GDC and Ni-LSNC microstructure on the nanoscale were also obtained on an FEI ThermoFisher Scientific Inc., USA (formerly FEI Tecnai Osiris transmission electron microscope (TEM) equipped with an EDX detector and operated at 200 keV in scanning transmission electron microscopy (STEM) mode. Samples for STEM/EDX analysis were prepared by a conventional 'lift-out' technique in a ThermoFisher Scientific Inc., USA (formerly FEI) Quanta 3D FEG FIB system [77].

4.2.3 Particle stability testing

Three pre-reduced cells were infiltrated with Ni, Ni-GDC, and Ni-LSNC, respectively, for particle stability testing. The weight gain of each cell after infiltration and heating to 320°C in air is reported in Table 6. Each infiltrated cell was then fractured into three pieces. Each piece was first heated to 800°C under the 2% H_2 – 98% Ar gas mixture flowing at 300 cm^3 min^{-1} and then exposed to different atmospheric conditions at 800°C. One piece from each type of infiltrated cell was held under the same atmosphere (flowing the 2% H_2 – 98% Ar gas mixture) for 1 hour, at which point all NiO was reduced to Ni. These will hereon be referred to as 'as-reduced' samples. The second piece from each type of cell was held under the same atmosphere for a longer period of 48 hours. The third piece of each type of sample was exposed to a 25% H_2 – 75% H_2O gas mixture flowing at 300 cm^3 min^{-1} for 48 hours. Fracture cross-section SEM images of the AAL were recorded from each piece for analysis.

4.2.4 Electrochemical testing[2]

Uninfiltrated, Ni-GDC infiltrated, and Ni-LSNC infiltrated cells were electrochemically tested to study the effect of Ni-MIEC infiltration on electrode performance. All cells were pre-reduced, and then the Ni-GDC and Ni-LSNC cells were infiltrated using their respective precursor solutions. The rounds of infiltration and weight gain after the heating procedure in air are listed in Table 6. In preparation for electrochemical testing, a silver mesh (Alfa Aesar, USA) was then adhered to the cathode surface using silver ink (Alfa Aesar, USA) and dried in air at 80°C. Nickel ink (Fuel Cell Materials, USA) was then painted onto the anode surface and the cell was placed on top of the nickel mesh current collector (Alfa Aesar, USA) before assembling the full electrochemical testing stand, which has been detailed in Chapter 3.3.2. The cell was placed between two Al_2O_3 tubes and the anode and cathode electrodes were gas sealed by using mica gaskets and glass paste. The entire assembly was spring-loaded between two aluminum end plates using Al_2O_3 rods for rigidity and to compress the mica gaskets. Nickel lead wires (Alfa Aesar, USA) on the anode side and silver lead wires (Alfa Aesar, USA) on the cathode side were protected by feeding them through small Al_2O_3 tubes. Al_2O_3 tubes were also used for inlet and outlet gas tubes on both anode and cathode sides. Cell temperature was monitored during electrochemical testing using a K-type thermocouple placed in the cathode side chamber approximately 1 cm away from cell.

After assembly, the electrochemical testing stand was placed in a furnace and heated to 800°C, as measured by the cathode side thermocouple, at 1°C min^{-1}. During

[2] Electrochemical testing was carried out by Paul Gasper.

heating, 1 L min^{-1} of dry air was flowed on the cathode side and 300 cm^3 min^{-1} of the 5% H_2 – 98% Ar gas mixture was flowed on the anode side. Once at the set temperature, the cell was held under open circuit condition for 12 hours to allow time for the glass paste to cure, and then the anode gas mixture was changed to 97% H_2 – 3% H_2O. The quality of the gas sealing was then evaluated by monitoring the cell's open circuit potential for the following 12 hours. The cell was then activated by applying 0.5 A cm^{-2} of current for 48 hours. Cell performance was measured at temperatures of 800°C, 750°C, and 700°C. I-V scans and EIS were used to evaluate cell performance. I-V scans were recorded from OCV to 700 mV at a rate of 5 mA s^{-1}. EIS scans were recorded at open circuit conditions using an AC amplitude of 30 mV between 200000 Hz and 0.02 Hz. After performance measurement, cells were cooled to room temperature and prepared for microstructural characterization.

4.2.5 Microstructural characterization after electrochemical testing

Fracture cross-section SEM images of the AAL were recorded from the uninfiltrated, Ni-GDC infiltrated, and Ni-LSNC infiltrated cells after electrochemical testing. Two distinct regions within the AAL: under the cathode, which is electrochemically active, and not under the cathode, which is not electrochemically active, were examined to evaluate the stability of the infiltrated nanoparticles after exposure to both the testing environment and electrochemical current.

To measure the porosity of the uninfiltrated, Ni-GDC infiltrated, and Ni-LSNC infiltrated cells after electrochemical testing, pieces of the fractured cells were infiltrated with epoxy and allowed to cure at room temperature. Epoxied samples were then

polished, and SEM images were taken at 50 micron intervals, starting at the anode/electrolyte interface, all the way across the 400 micron thick anode. At each depth, three images were taken at 40 kX magnification. The porosity was measured by segmenting out the pores from each image using Avizo 3D (ThermoFisher Scientific Inc., USA), shown in Figure 22, calculating the fraction of pore area from each image, and then calculating the average value of the three measurements. The pore occupation ratio, which is a simple measure of how much pore volume is occupied by the infiltrants, was then calculated using Equation 2.

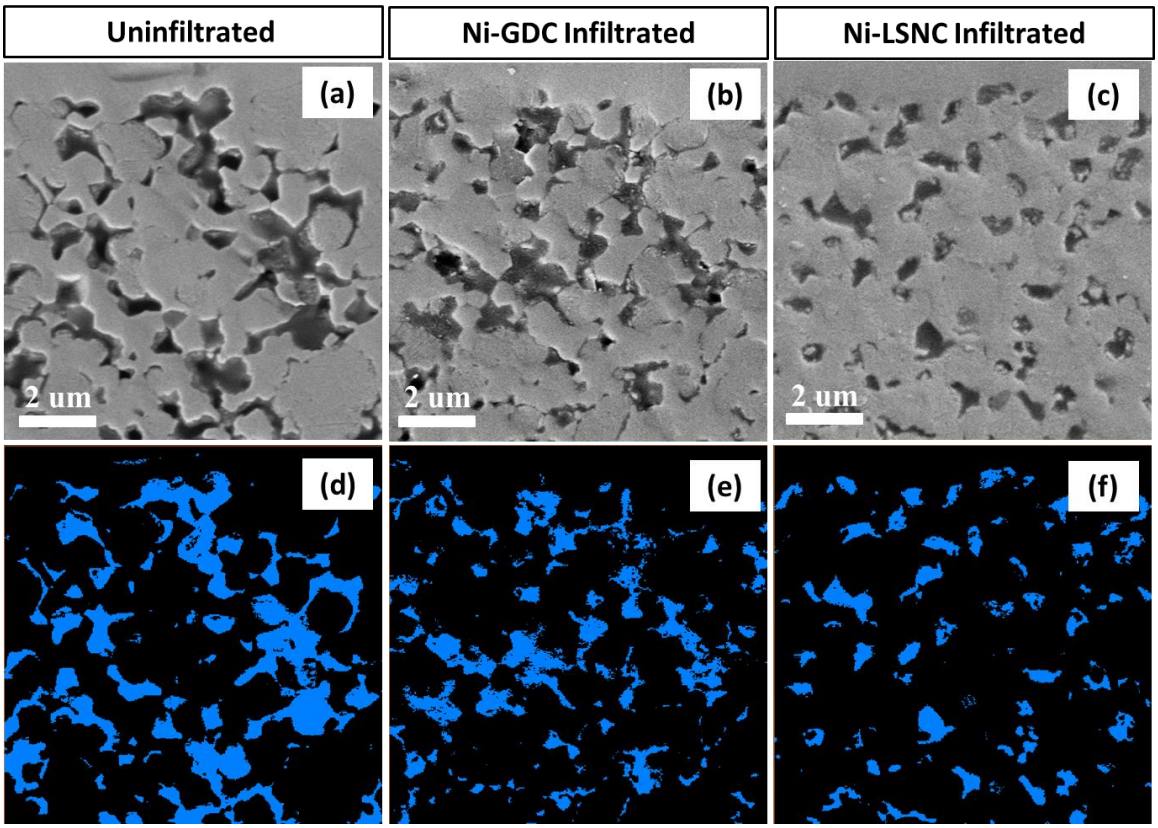

Figure 22. SEM micrographs of (a) uninfiltrated, (b) Ni-GDC infiltrated, and (c) Ni-LSNC infiltrated epoxied samples. The images of (d) uninfiltrated, (e) Ni-GDC infiltrated, and (f) Ni-LSNC infiltrated cells showing segmented pores.

$$Pore\ Occupation\ Ratio$$

$$= \frac{Porosity\ of\ Uninfiltrated\ Cell - Porosity\ of\ Infiltrated\ Cell}{Porosity\ of\ Uninfiltrated\ Cell}$$

$$= \frac{Volume\ of\ Infiltrant}{Porosity\ of\ Uninfiltrated\ Cell} \quad (2)$$

4.3 Results and discussion

4.3.1 Validation of MIEC synthesis

Validation of Ni-GDC and Ni-LSNC as suitable materials for infiltration into Ni-YSZ cermet anodes requires that they meet the following four criteria: i) the Ni-MIEC precursors can be dissolved in a liquid solution; ii) the Ni-MIEC composite can be synthesized in the anode operating environment; iii) the infiltration solutions successfully penetrate through the entire anode and deposit nanoparticles within the AAL; and iv) the Ni nanoparticles are in contact with and stabilized by the MIEC. The first criterion is met by simply finding a solvent that can dissolve the precursors, ideally in a high concentration, and maintain a low enough viscosity to enable infiltration. Both GDC and LSNC nitrate precursors dissolve readily into ethanol at 70°C. Details of the precursor solutions are listed in Table 6. A critical difference between the Ni-GDC and Ni-LSNC precursor solutions is the inclusion of citrate into the LSNC solution. This is added because the perovskite phase requires combustion between the citrate and nitrate to form, while the GDC phase will form readily from decomposition of the nitrate precursors [72,78,79]. The inclusion of citric acid makes the molarity of the Ni-LSNC metal ion precursors to be lower than that of the citric acid free Ni-GDC metal ion precursors. This requires more infiltration cycles for the Ni-LSNC infiltration.

The second criterion is validated by measuring the crystal phase using powder XRD after exposure to the reducing gas at 800°C. The θ-2θ x-ray diffraction scans of Ni-GDC and Ni-LSNC powders are shown in Figure 23a and Figure 23b, respectively. The scans match the nickel plus fluorite and nickel plus perovskite target product patterns, respectively, confirming that the Ni-GDC and Ni-LSNC composites are properly formed from their respective precursor solutions. The third criterion is validated by infiltrating pre-reduced Ni-YSZ anodes with the Ni-MIEC precursor solution. Figure 24b-c show SEM micrographs of the AAL of the Ni-GDC infiltrated and Ni-LSNC infiltrated cells after reduction at 800°C. A high density of infiltrant and good nanoparticle area coverage is clearly observed in both cells, confirming that both Ni-MIEC infiltration solutions successfully penetrate through the anode.

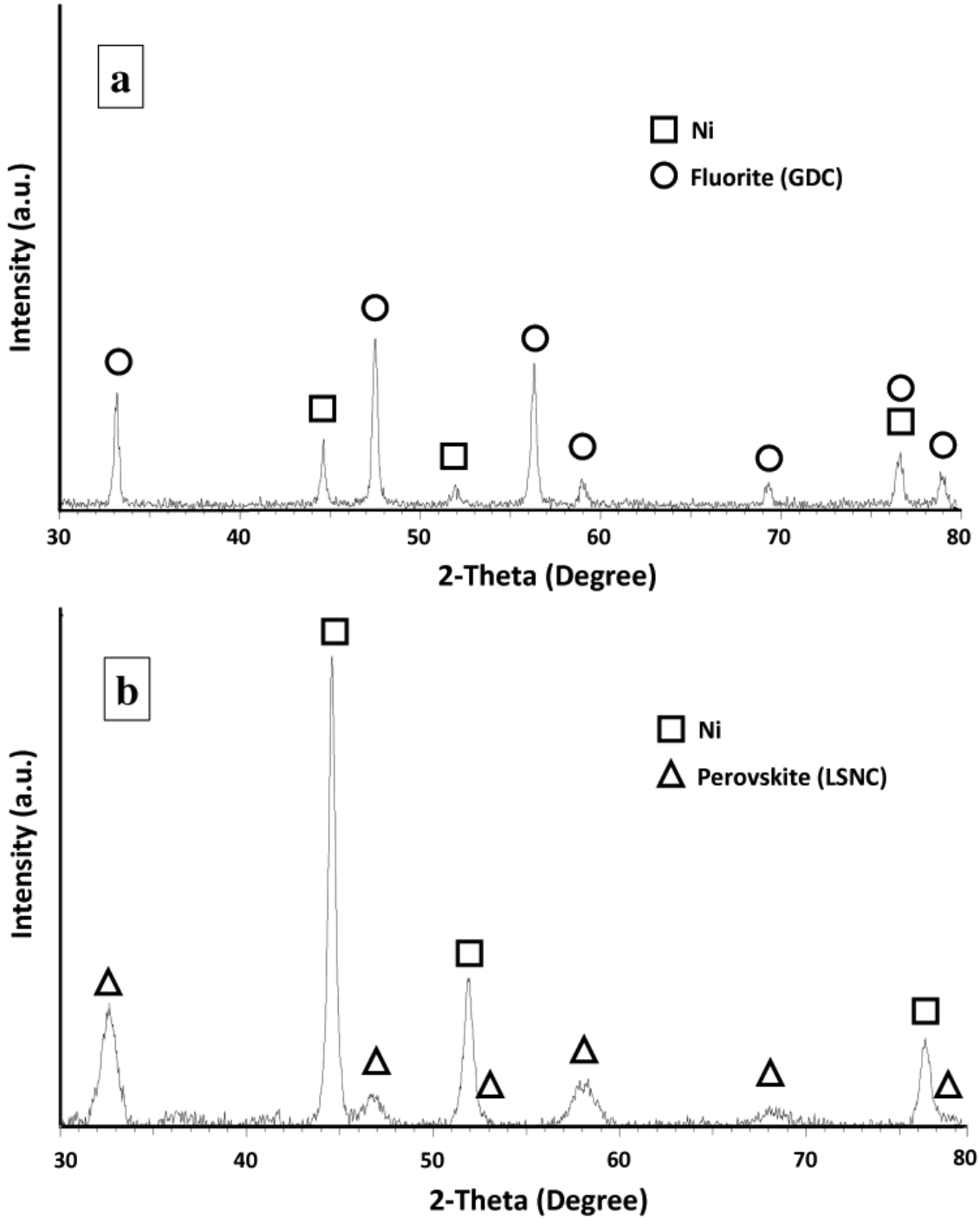

Figure 23. θ-2θ x-ray diffraction scans of a) Ni-GDC and b) Ni-LSCN powders synthesized from their respective precursor solutions confirming the formation of the pure phase of Ni-GDC and Ni-LSNC powder mixtures.

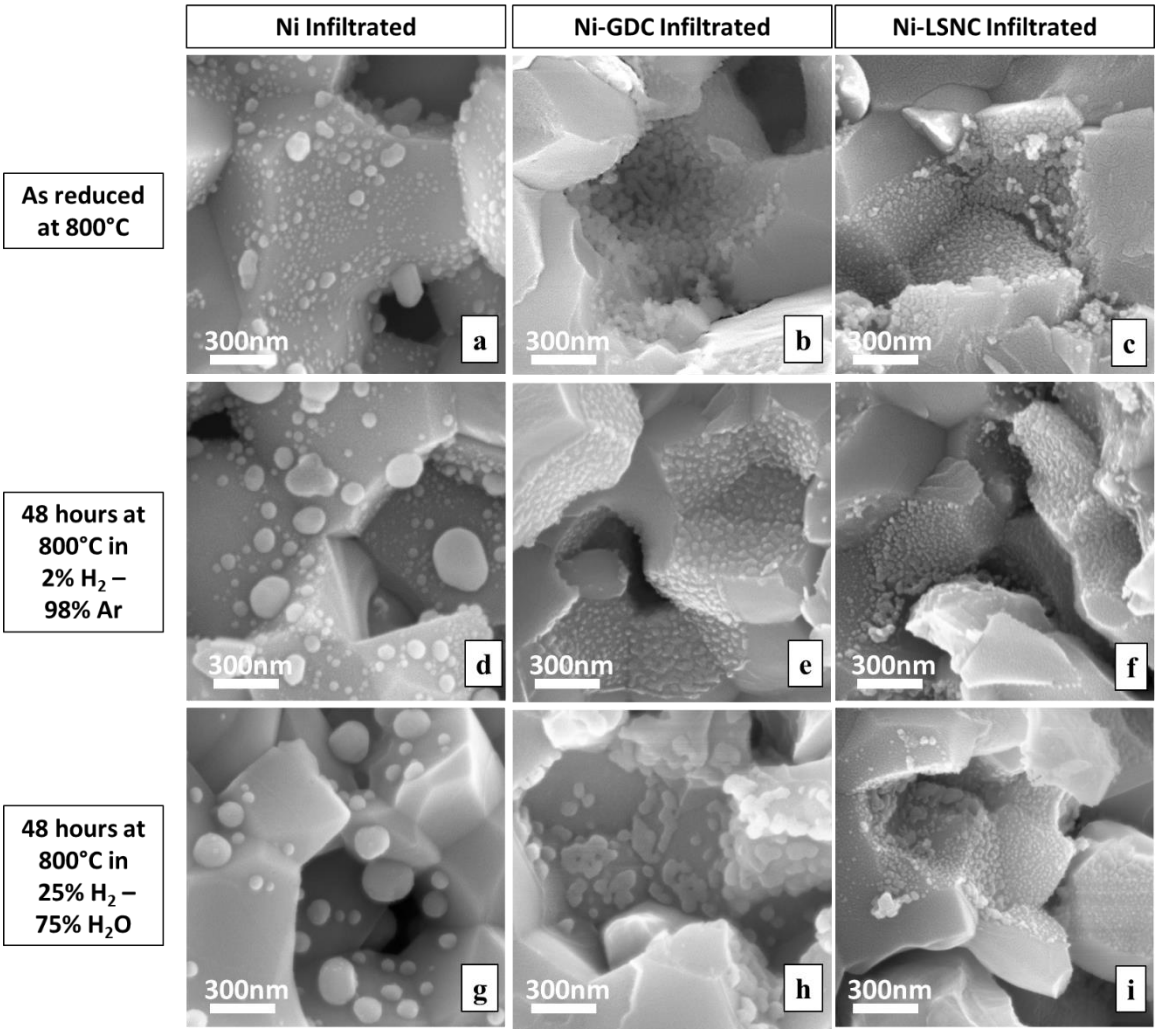

Figure 24. SEM micrographs of the AAL regions in fracture cross-sections of Ni infiltrated, Ni-GDC infiltrated, and Ni-LSNC infiltrated cells. a)-c) show the nanoparticles in the as reduced state; d)-f) show the nanoparticles after a 48 hour exposure in flowing 2% H_2 – 98% Ar gas mixture at 800°C; and g)-i) show the nanoparticles after a 48 hour exposure in flowing 25%H_2 – 75%H_2O gas mixture at 800°C.

In order to validate the fourth criterion, the individual Ni and MIEC particles need to be distinguishable. Cross-sectional high angle annular dark field (HAADF) STEM images of the pores and adjacent grains with elemental distributions in the AAL layer for the Ni-GDC and Ni-LSNC infiltrated cells after electrochemical testing are presented in

Figure 25. The nanoparticles in Ni-GDC and Ni-LSNC infiltrated cells are essentially connected with each other and also with cermet Ni grains. The results of the STEM/EDX elemental mapping shown in Figure 25 also suggest that while Ni-GDC simply wets the surface of the Ni-YSZ grains, the Ni-LSNC fills a substantial amount of space within the pore. Also, in the Ni-GDC infiltrated cell, the rounded Ni nanoparticles are only deposited on YSZ grains, while in the Ni-LSNC infiltrated cell, the Ni nanoparticles can be found in the vicinity of both YSZ and Ni grains. These differences are likely due to the citrate-nitrate combustion reaction needed to form the LSNC phase, which causes a rapid gas expansion during the heating procedure.

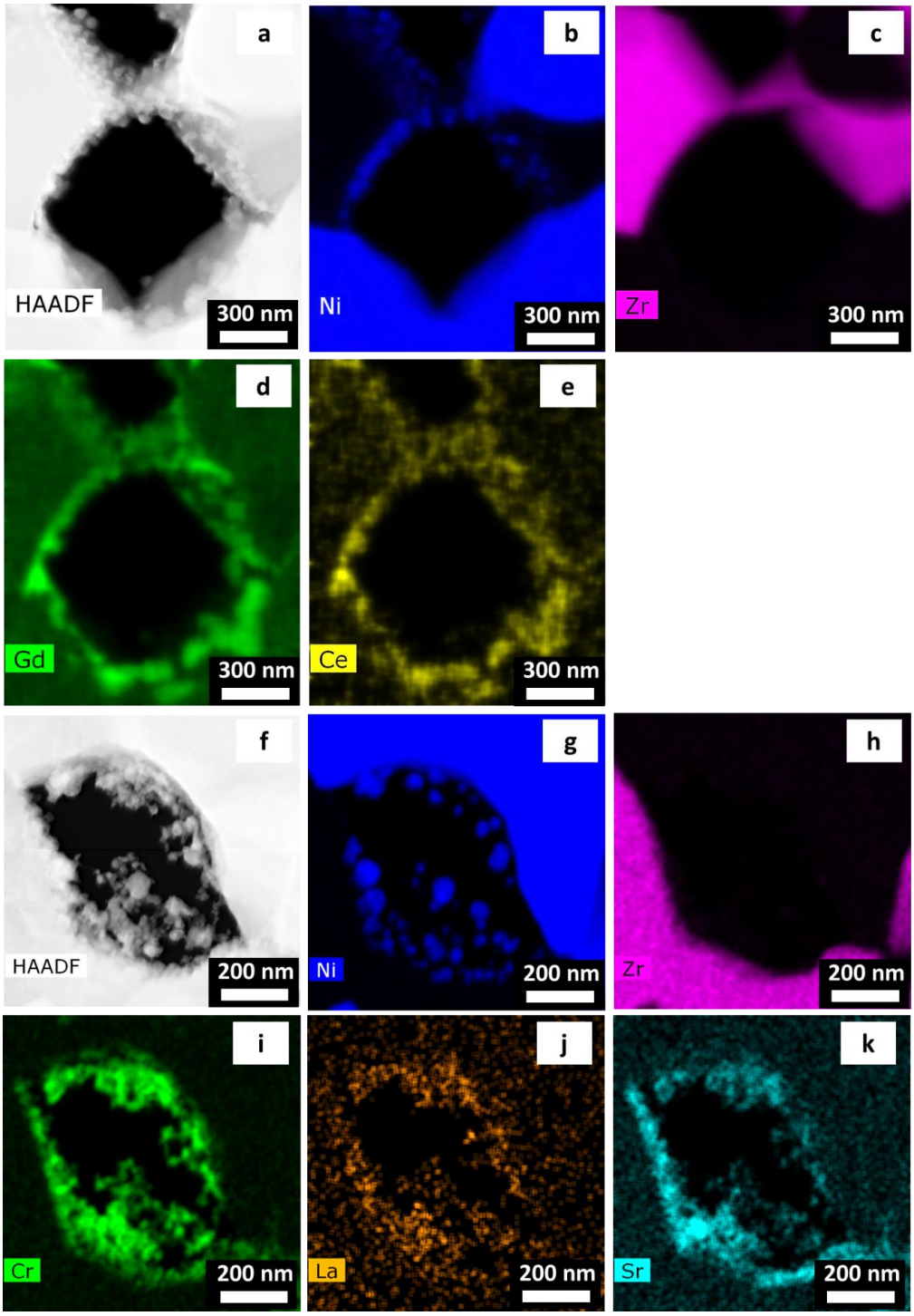

Figure 25. a) HHADF STEM micrograph of the AAL of the Ni-GDC infiltrated cell after electrochemical testing, with elemental EDX maps of b) Ni, c) Zr, d) Gd, and e) Ce. f) HAADF STEM micrograph of the AAL of the Ni-LSNC infiltrated cell after electrochemical testing, with elemental EDX maps of g) Ni, h) Zr, i) Cr, j) La, and k) Sr.

4.3.2 Stability of infiltrated nanoparticles

In order to qualitatively show the effects of MIEC infiltration on the stability of the Ni nanoparticles, the microstructures of Ni infiltrated, Ni-GDC infiltrated, and Ni-LSNC infiltrated anodes are compared after a reduction at 800°C, after a 48 hour exposure to the reducing environment at 800°C, and after a 48 hour exposure to a 25% H_2 – 75% H_2O at 800°C. The humid atmosphere accelerates the coarsening of Ni nanoparticles, primarily due to the increased wetting of Ni on YSZ surfaces, although the contact angle decreases sharply only when humidity levels go above 95% [11,80–82]. Investigation of the Ni infiltrated anode (Figure 24a, Figure 24d, Figure 24g) reveals that infiltrated Ni nanoparticles with diameters less than 50 nm are unstable after the 48 hour exposure to high temperature in dry hydrogen (Figure 24d). After the 48 hour exposure to a humid gas mixture (Figure 24g), nearly all nanoparticles with diameters less than 100 nm disappeared. By comparison, nanoparticles in both the Ni-GDC infiltrated (Figure 24b, Figure 24e, Figure 24h) and Ni-LSNC infiltrated (Figure 24c, Figure 24f, Figure 24i) samples maintain stable and percolated features of less than 100 nm, demonstrating that the additional oxide phases inhibit Ni nanoparticle coarsening. This is likely because the oxide phases pin the Ni nanoparticles, thereby blocking direct contact between them.

4.3.3 Electrochemical performance

The results of electrochemical testing of the uninfiltrated, Ni-GDC infiltrated, and Ni-LSNC infiltrated cells are shown in Figure 26, and performance data from these measurements is listed in Table 7. The I-V plots (Figure 26a-c) and the power density data (Table 7) show that the Ni-GDC infiltrated cell has the best performance and that the

Ni-LSNC cell has a slightly higher performance compared to the uninfiltrated cell. The most obvious trend is that the performance of the Ni-GDC cell relative to the uninfiltrated cell increases as the operation temperature of the cell decreases; at 800°C, the Ni-GDC infiltrated cell has 30% greater power at 750 mV, while at 700°C it has 56% greater power at 750 mV. This implies that the infiltration of Ni-GDC into the anode improves charge transfer kinetics, because charge transfer resistance increases quickly when cell temperature is lowered, while the increase in mass transfer resistance is very small [53,83]. The Ni-GDC infiltration appears to have only a small impact on mass transfer resistance, because the cell performance is improved at 800°C, when cell performance is most sensitive to the kinetics of mass transfer. This is in contrast to the Ni-LSNC infiltrated cell, which shows a negligible performance increase at 800°C. The Ni-LSNC infiltrated cell does have some small improvement compared to the uninfiltrated cell as the operation temperature reduces, showing an 11% increase in power at 700°C. This suggests that Ni-LSNC does improve the charge transfer of the cell, but clearly at the cost of the increased mass transfer resistance.

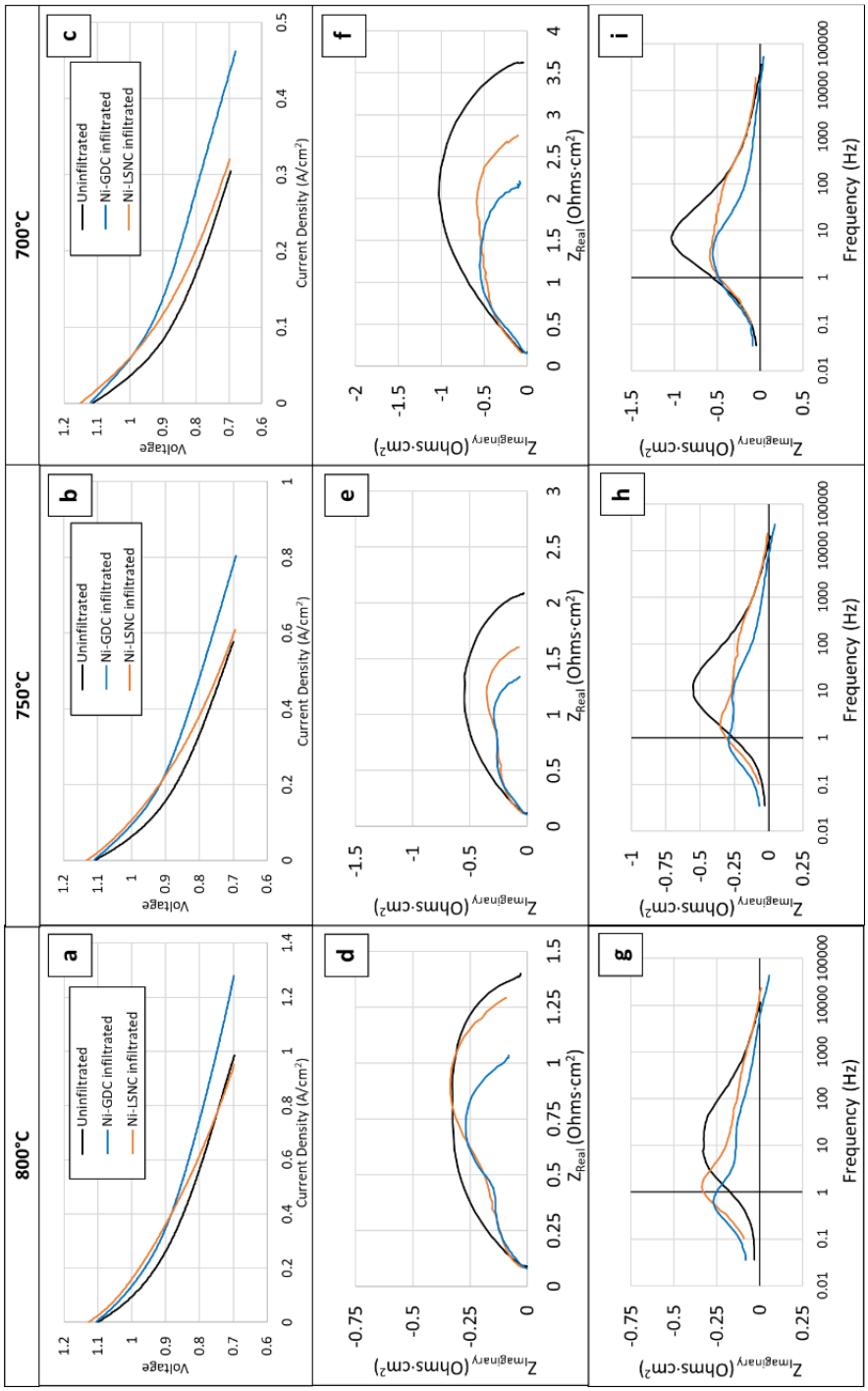

Figure 26. Electrochemical performance measurements of uninfiltrated, Ni-GDC infiltrated, and Ni-LSNC infiltrated cells recorded at 800°C, 750°C, and 700°C with 3% humidified hydrogen flowing over the anode and dry air flowing over the cathode. Measurements include a)-c) I-V scans, and EIS measurements plotted in d)-f) Nyquist, and g)-i) and Bode formats.

Analysis of the EIS measurements supports these conclusions. The improvement of the polarization resistance for both Ni-GDC infiltration and Ni-LSNC infiltrated cell increases as the operation temperature decreases, as shown by the Nyquist plots in Figure 26d-f and in Table 7. This trend corresponds to an improvement of the anodic charge transfer kinetics after infiltration of the Ni-MIEC composites. However, Ni-LSNC shows less improvement than Ni-GDC. The Bode plots, shown in Figure 26g-i, reveal that at 800°C, the Ni-LSNC infiltrated cell has a noticeably larger peak at about 1 Hz than either the Ni-GDC infiltrated or uninfiltrated cells. This peak corresponds to the anodic mass transfer process, which is the slowest physical process of the cell. This demonstrates that the Ni-LSNC infiltrated cell suffers from poor mass transfer characteristics, limiting cell performance at higher temperatures. The Ni-GDC cell also has a peak around 1 Hz, but the peak height is much smaller than that for the Ni-LSNC cell. This indicates that the mass transfer resistance of the Ni-GDC infiltrated cell has not been increased substantially compared to the uninfiltrated cell. As operation temperature is reduced, both anodic and cathodic charge transfer resistances increase and the mass transfer peaks becomes less distinct. However, Ni-LSNC still exhibits lower performance than Ni-GDC. From this result, it is clear that the Ni-GDC is a more effective infiltrant than the Ni-LSNC.

Table 7. Performance data from EIS and I-V measurements of uninfiltrated, Ni-GDC infiltrated, and Ni-LSNC infiltrated cells.

$R_{Polarization}$ ($\Omega \cdot cm^2$) (97% H_2 – 3% H_2O anode, 21% O_2 cathode)					
Temperature	Uninfiltrated	Ni-GDC infiltrated	Change	Ni-LSNC infiltrated	Change
800°C	1.31	0.95	-27%	1.20	-8%
750°C	1.97	1.23	-38%	1.49	-24%
700°C	3.47	2.05	-41%	2.60	-25%
R_{Ohmic} ($\Omega \cdot cm^2$) (97% H_2 – 3% H_2O anode, 21% O_2 cathode)					
Temperature	Uninfiltrated	Ni-GDC infiltrated	Change	Ni-LSNC infiltrated	Change
800°C	0.09	0.08	-10%	0.10	+6%
750°C	0.12	0.11	-8%	0.12	-1%
700°C	0.16	0.15	-5%	0.16	-2%
Power Density at 750 mV ($W \cdot cm^{-2}$) (97% H_2 – 3% H_2O anode, 21% O_2 cathode)					
Temperature	Uninfiltrated	Ni-GDC infiltrated	Change	Ni-LSNC infiltrated	Change
800°C	0.57	0.74	+30%	0.57	+0%
750°C	0.34	0.47	+39%	0.36	+6%
700°C	0.17	0.27	+56%	0.19	+11%

The decrease in polarization resistance for the Ni-MIEC (GDC/LSNC) infiltrated samples can be explained by the presence of additional activated TPBs and possible expansion of the region of charge transfer around the active TPBs. Both result in increased charge transfer reactions per unit area of the anode and effective lowering of the polarization resistance. Depending on the spacing between the Ni nanoparticles and the Ni-YSZ backbone, the LSNC being primarily electronically conducting could provide an electronic pathway, thereby activating additional TPBs. Although GDC is not considered a good electronic conductor, its partial electronic conductivity is substantially higher than YSZ and its ionic conductivity is also higher than YSZ. In this case, the likely mechanisms for improved performance are due to the expansion of the charge transfer region around the active TPBs associated with GDC, as well as an increase in the

thickness of the effective AAL due to enhanced oxygen ion diffusion. GDC is also reported to have a higher catalytic activity which could also be responsible for the improved performance.

4.3.4 Anode microstructures after electrochemical testing

In Chapter 3, it was shown that infiltrated Ni nanoparticles coarsen during electrochemical testing, resulting in a reduction of the added TPB density, leading to a decrease in cell performance. To analyze the impact of the cell testing procedure on the stability of the infiltrated features, two different facture cross-section regions of the AAL of each cell after electrochemical testing were studied by SEM: the ‘electrochemically inactive region’ that is not under the cathode, and the ‘electrochemically active’ region which is under the cathode (Figure 27a). The ‘electrochemically inactive’ region has been exposed to the testing environment, but does not experience any electrochemical current and anodic reactions due to the lack of a cathode above this region. The ‘electrochemically active’ region is exposed to both the testing environment and the effects of electrochemical current and anodic reactions. SEM micrographs taken from the ‘electrochemically inactive’ regions are shown in Figure 27b-c, while those from ‘electrochemically active’ regions are shown in Figure 27d-e. Comparing these microstructures to the ‘as-reduced’ microstructures (Figure 24b-c) shows the effects of exposure to high temperature, reducing environment, and electrochemical current and reactions on the stability of the infiltrated Ni-GDC and Ni-LSNC nanostructures.

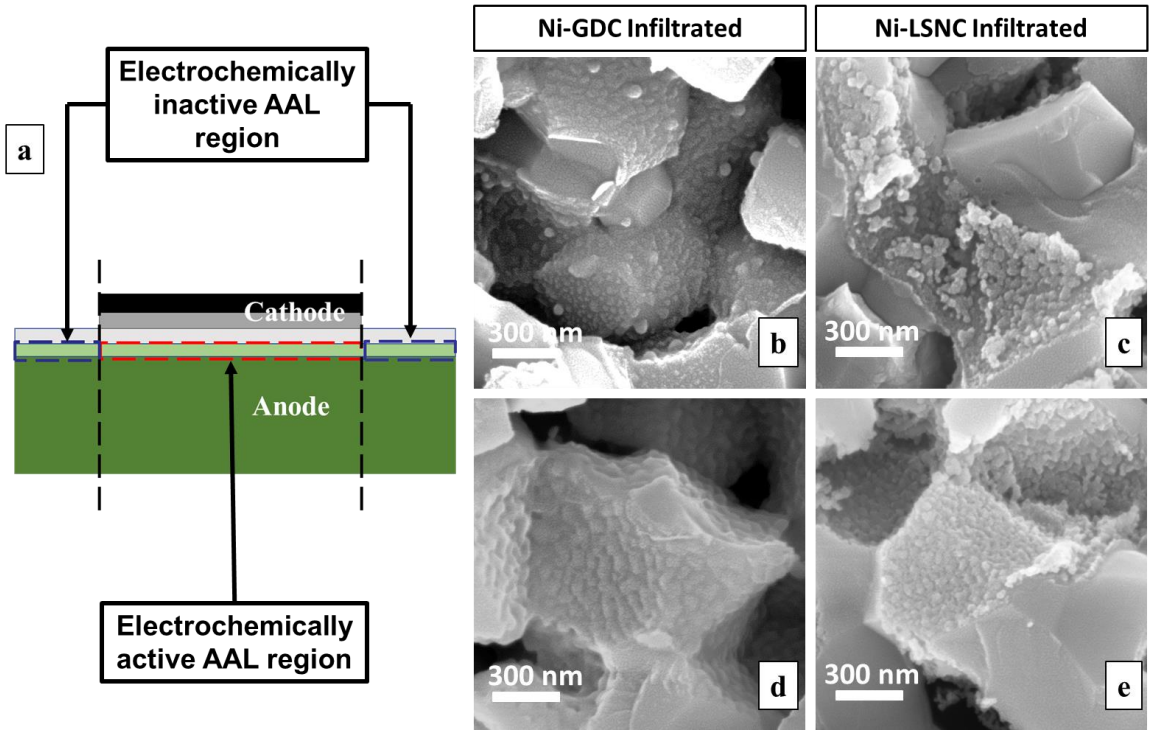

Figure 27. a) Schematic of the cell showing the locations of 'electrochemically inactive' (not under cathode) and 'electrochemically active' (under cathode) regions in the AAL. Fracture cross-section SEM images of infiltrated Ni-GDC and Ni-LSNC nanoparticles in the b)-c) 'electrochemically inactive', and d)-e) 'electrochemically inactive' regions of the AAL.

Comparing Figure 24c to Figure 27c shows some evidence of increased agglomeration (since individual nanoparticles are still clearly visible, this is a case of agglomeration rather than coarsening) of Ni-LSNC nanoparticles after the additional 72 hours of exposure of these nanoparticles to the atmosphere at 800°C during the electrochemical testing (see Chapter 4.2.4 for details of electrochemical testing procedure) without exposure to the electrochemical current and chemical reactions. Comparing Figure 24b to Figure 27b shows significantly less agglomeration of the Ni-GDC nanoparticles after the additional high temperature exposure. Interestingly, Figure 27d-e show that exposure to electrochemical current and reactions cause both the Ni-GDC and

Ni-LSNC nanostructures to spread evenly across the Ni-YSZ grains. This may actually be beneficial for the stability of the electrode, because the infiltrated nanoparticles are now more homogenously distributed, preventing the formation of hot spots with very high local current density that may lead to accelerated nanoparticle coarsening. Such 'spreading' due to lowering of the contact angle has been previously observed for infiltrated Ni nanoparticles during electrochemical testing [62], and similar principles are likely at play for the Ni-GDC and Ni-LSNC microstructures. Generally, both Ni-GDC and Ni-LSNC nanoparticles appear to be stable in the 'electrochemically active' AAL regions, which is where the majority of the anodic electrochemical reactions occurs. This is good for persistence of the long-term benefits of anode infiltration.

In order to better understand the increase of mass transfer resistance observed during electrochemical testing (Chapter 4.3.3), the porosity distribution throughout the anodes of different cells was obtained from the SEM images taken on polished cross-sections. The resulting porosity profiles for the uninfiltrated, Ni-GDC infiltrated, and Ni-LSNC infiltrated cells are shown in Figure 28a. Each data point corresponds to the average porosity measured from three images with the uncertainty bars representing the maximum and minimum porosity. The uninfiltrated cell shows a nearly uniform porosity, while both the Ni-GDC and Ni-LSNC cells have a lower porosity throughout the entire anode. In general, the citrate-nitrate combustion process forms Ni-LSNC in a 3-D microstructure that occupies a larger volume fraction of the pores. The nitrate decomposition process forms Ni-GDC in a 2-D microstructure on the pores surface causing more modest pore filling. In particular, the Ni-LSNC cell shows dramatically

reduced porosity near the anode-electrolyte interface. This could be expected because the individual pores of the AAL are smaller than the pores of the bulk anode.

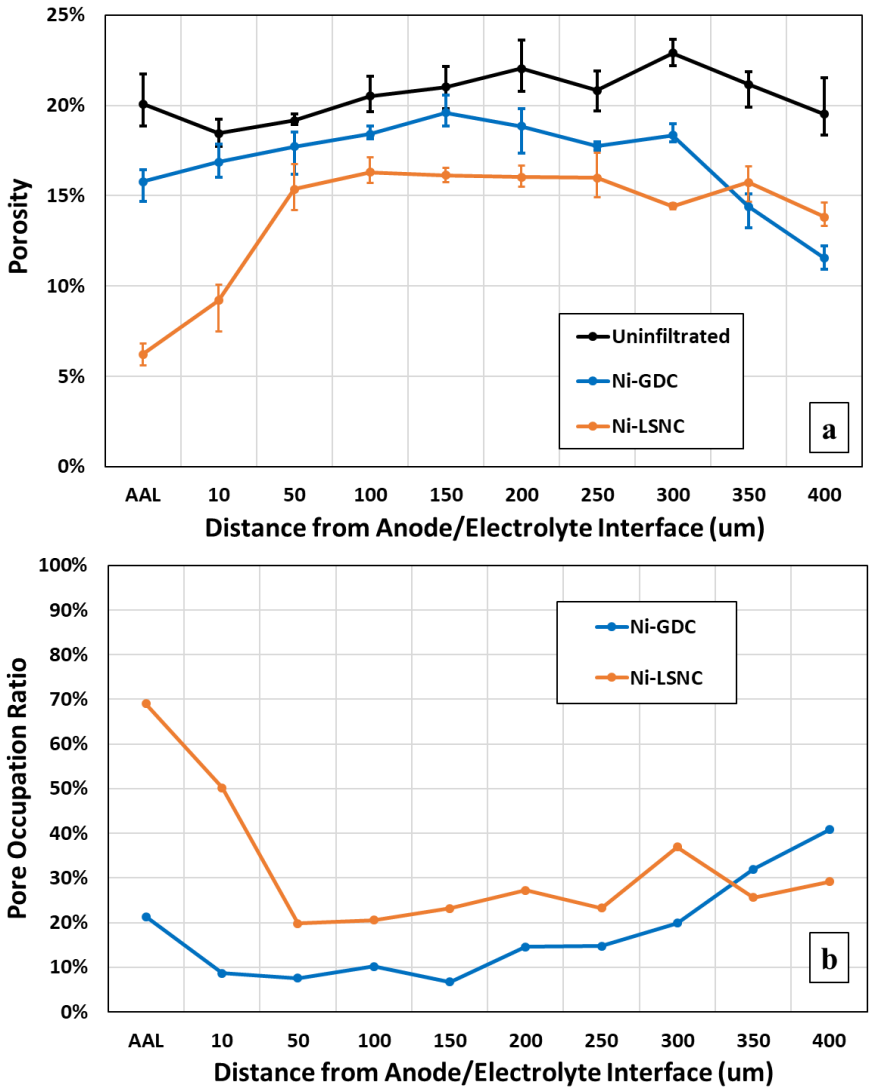

Figure 28. a) Measured porosity profile across the anode cross-section of uninfiltrated, Ni-GDC infiltrated, and Ni-LSNC infiltrated cells. B) Calculated pore occupation ratio distribution across the anode cross-section for Ni-GDC infiltrated and Ni-LSNC infiltrated cells.

The extent of pore filling can be seen clearly from the pore occupation ratio, which is calculated using Equation 2 and shown in Figure 28b. The pore occupation ratio is a

measure of how much pore volume is filled by the infiltrants. When averaged across the whole electrode, the infiltration of Ni-GDC reduced the pore volume by 17.1% while the infiltration of Ni-LSNC reduced the pore volume by 28.6%. Assuming that the effective diffusivity of the $H_2 - H_2O$ gas mixture varies linearly with the electrode porosity, this corresponds to a 17.1% and 28.6% reduction in the effective diffusivity of the Ni-GDC infiltrated and Ni-LSNC infiltrated cells, respectively. Assuming Fickian diffusion mechanism in the anode, the mass transfer resistance of the electrode is inversely proportional to the effective diffusivity [58]. Thus, the filling of pores by infiltration results in a 20.6% increase in mass transfer resistance for the Ni-GDC infiltrated cell compared to the uninfiltrated cell, and a 40.1% increase in mass transfer for the Ni-LSNC infiltrated cell compared to the uninfiltrated cell.

4.4 Conclusions

Ni-YSZ cermet anodes have been co-infiltrated with nanoparticles of Ni and a MIEC oxide phase. The roles of the conductive oxides were to provide a conductive pathway to electrically connect some or all the Ni nanoparticles with each other and the Ni-YSZ cermet anode, and to physically isolate them to avoid coarsening. Two oxides were chosen based on their chemical stability and conductivity in the anode operation environments: $Gd_{0.1}Ce_{0.9}O_{2-\delta}$, a predominantly an ionic conductor, and $La_{0.6}Sr_{0.3}Ni_{0.15}Cr_{0.85}O_{3-\delta}$, a predominantly electronic conductor. Cells were successfully infiltrated to form Ni-GDC and Ni-LSNC nanostructures. The Ni-GDC and Ni-LSNC nanostructures were both more stable to 48 hour exposures to dry and 75% humid hydrogen atmospheres at 800°C, compared to only infiltrated Ni nanostructures.

The Ni-GDC infiltrated cell demonstrated substantially improved electrochemical performance at 800°C, 750°C, and 700°C, while the Ni-LSNC infiltrated cell only demonstrated a clear performance improvement at 700°C. Both Ni-GDC and Ni-LSNC infiltrated cells exhibited improved anodic charge transfer kinetics, but the Ni-LSNC cell also suffered from substantially increased mass transfer resistance. This was attributed to a 28.6% pore filling with a 3-D microstructure for the Ni-LSNC, as compared to a 17.1% pore filling with a 2-D microstructure for the Ni-GDC. The nanostructures in the 'electrochemically active' AAL regions of the cells remained resistant to significant coarsening and agglomeration, ensuring that the long-term benefits of the infiltration persist. The next chapter is a detailed study on impacts of Ni, GDC, and Ni-GDC infiltration on Ni-YSZ electrode performance.

5. Effects of different infiltrations

5.1 Introduction

As mentioned in Chapter 4, co-infiltration of Ni and a MIEC in Ni-YSZ cermet anode improves Ni particle stability and cell performance. Ni-GDC has been shown to be a more effective infiltrant than Ni-LSNC since it significantly improves charge transfer kinetics with modest increase of mass transfer resistance. In this chapter, uninfiltrated, Ni infiltrated, GDC infiltrated, and Ni-GDC infiltrated cells is studied to understand the impact of each infiltrant on Ni-YSZ cermet anode performance. The long-term (120 hours) cell performances and the cell microstructures before and after electrochemical testing was compared to demonstrate the stability of infiltrants.

5.2 Materials and methods

5.2.1 Infiltration of button cells

The anode-supported SOFC button cells from SOFCMAN Energy (Ningbo, China) were used. All cells were prepared by pre-reducing the NiO-YSZ anode to Ni-YSZ. The reduction of NiO to Ni opens pores enabling anode infiltration. For each infiltrant, two infiltrated cells were used, one for the particle stability testing and the other for electrochemical testing. Each round of infiltration was followed by a heat treatment to thermal decompose the liquid precursors into oxides and then the cell weight gain was measured. The procedures of anode pre-reduction, anode infiltration, and heat treatments of the infiltrated cells has been detailed in Chapter 3.3.1. The number of rounds of infiltration and the compositions of precursor solutions used are listed in Table 8.

Table 8. Details of precursor solutions and infiltrated cells.

Cell:	Ni infiltrated		GDC infiltrated		Ni-GDC infiltrated	
Testing:	Stability testing	Electro-chemical testing	Stability testing	Electro-chemical testing	Stability testing	Electro-chemical testing
Weight gain:	1.57%	1.62%	1.21%	1.3%	1.33%	1.29%
Rounds of infiltration:	5	5	1	1	1	1
Infiltration solution molarity:	1M Ni		2M GDC		2M Ni, 2M GDC	

5.2.2 Particle stability testing

Three conditions were used to test particle stabilities of the Ni infiltrated, GDC infiltrated, and Ni-GDC infiltrated. Each infiltrated cell was fractured into three pieces. The first piece was heated to 800°C while flowing 2% H_2 – 98% Ar gas at 300 cm^3 min^{-1} and held for 1 hours. This condition is referred to ‘as reduced’. The second piece was heated to 800°C while flowing 2% H_2 – 98% Ar gas at 300 cm^3 min^{-1} and held for 48 hours. This condition is referred to as ‘high temperature’ exposure. The third piece was heated to 800°C while flowing 25% H_2 – 75% H_2O gas mixture at 300 cm^3 min^{-1} and held for 48 hours. This condition is referred to as ‘high temperature and humidity’ expsoure. Fracture cross-section SEM images of the AAL of the uninfiltrated and all pieces of the infiltrated cells were recorded for microstructural comparison.

5.2.3 Electrochemical testing[3]

A two-chamber atmosphere design was used for the electrochemical testing shown in Chapter 3.3.2. The button cell was sandwiched by two alumina tubes creating two separated compartments for anodic and cathodic gas environment. Both electrodes of the button cell were attached with metallic meshes and connected with two lead wires for current and potential measurements. The anode side was exposed to H_2O-H_2 gas mixtures and the cathode side was exposed to air. All cells have followed the same preparation and electrochemical testing procedures detailed in Chapter 4.2.4. The cell performances of the uninfiltrated, Ni infiltrated, GDC infiltrated and Ni-GDC infiltrated were measured by using I-V scans and EIS at temperatures of 800°C, 750°C, and 700°C with 97% H_2 – 3% H_2O on the anode side and 21% O_2 on the cathode side. Then all cells were conducted to a long-term stability test using a galvanostatic mode with the current density of 1 A cm^{-2} at a temperature of 800°C with 97% H_2 – 3% H_2O on the anode side and 21% O_2 on the cathode side. The cell voltages were monitored for 120 hours.

5.2.4 Microstructural characterization after electrochemical testing

Fracture cross-section SEM images of the AAL were recorded from the uninfiltrated, Ni infiltrated, GDC infiltrated, and Ni-GDC infiltrated cells after electrochemical testing. Two distinct regions within the AAL: under the cathode, which is electrochemically active, and not under the cathode, which is not electrochemically active, were examined to evaluate the stability of the infiltrated nanoparticles after exposure to both the testing environment and electrochemical current. The porosity

[3] Electrochemical testing was carried out by Paul Gasper.

profiles of the whole anode of the uninfiltrated, Ni infiltrated, GDC infiltrated, and Ni-GDC infiltrated cells after electrochemical testing were measured. The procedures are detailed in Chapter 4.2.5.

5.3 Results and discussion

5.3.1 Stability of infiltrated nanoparticles

The cell weight gains of all infiltrated cells are shown in Table 8 and are similar to the infiltrated cells in Chapter 4.2.1 indicating successful anode infiltration. The microstructures of the uninfiltrated cell, and the infiltrated cells with exposure to different atmosphere conditions have been shown in Figure 29. For the uninfiltrated cell (Figure 29a, 29e, 29i), there were no significant microstructural changes in the Ni-YSZ cermet, implying that the grain sizes larger than 1 um are very stable at these conditions. The infiltrants have been analyzed based on three properties: particle size, surface coverage on substrate and connectivity with each other and with substrate. For the Ni infiltrated cell, the Ni particle size under the ‘as reduced’ condition was mostly around 30-50 nm (Figure 29b). After exposure to the high temperature condition, the particle size increased to 50-100 nm (Figure 29f). After exposure to the high temperature and humidity condition, the particle size increases substantially. Particles with sizes less than 100 nm have disappeared (Figure 29j), which implies the humidity condition exacerbates particle coarsening. The Ni particles at all three conditions show high surface coverage and very low connectivity, and thus need the Ni spreading procedure to connect them at high temperatures. For the GDC infiltrated cell (Figure 29c, 29g, 29k), the GDC particles remain fine, highlighting the high microstructural stability of GDC at reducing and humid

conditions. Also, the GDC particles had good surface coverage and decent connectivity, which is presumably due to the good wettability of GDC on YSZ. Therefore, GDC is capable of maintaining the nano-sized microstructures and percolated networks. For the Ni-GDC infiltrated cell, the particles also remain nano-sized at the ‘as reduced’ condition (Figure 29d) and after high temperature exposure (Figure 29h). Even though the particle sizes increase slightly under the high temperature and humidity exposure (Figure 29l), they were still much smaller than the case of Ni infiltration alone (Figure 29j). This indicates that the existence of GDC inhabits Ni particle coarsening by mitigating the direct contact between Ni particles.

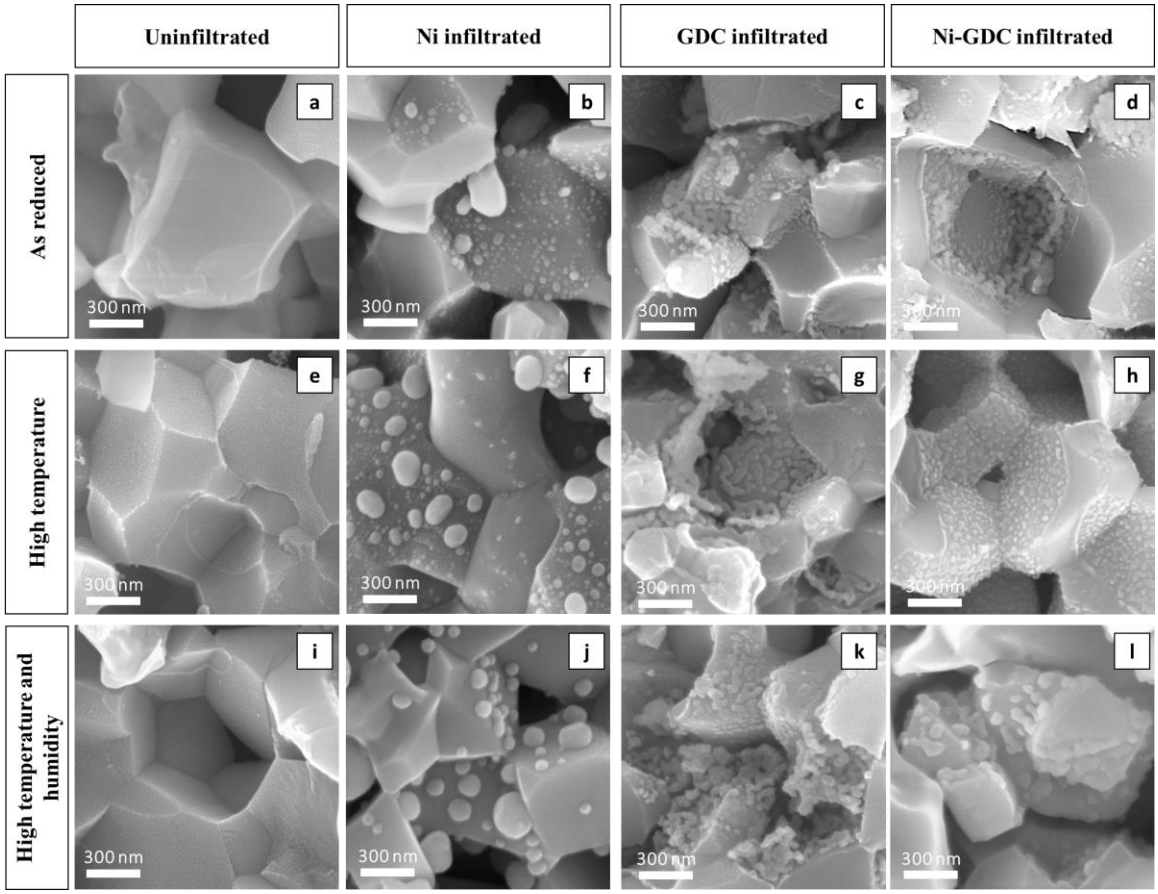

Figure 29: SEM micrographs of the AAL regions in fracture cross-sections of uninfiltrated, Ni infiltrated, GDC infiltrated, and Ni-GDC infiltrated cells a)-d) show the 'as reduced' state; e)-h) show the state after 'high temperature' exposure; and i)-l) show the state after 'high temperature and humidity' exposure.

5.3.2 Electrochemical performance

The cell performances of the uninfiltrated, Ni infiltrated, GDC infiltrated, and Ni-GDC infiltrated cells are shown in Figure 30 and performance data of these measurements are listed in Table 9. The I-V plots (Figure 30a-c) and the power density data demonstrate that, as temperatures decrease, the power density gains of all infiltrated cells increased compared to the uninfiltrated cell. It has the same trend in Chapter 3.4 and proves the infiltrants effectively increase the active TPB density. However, at 800°C, the power density gains of the Ni infiltrated and GDC infiltrated were less than one-half

compared to that of the Ni-GDC infiltrated cell. At 750°C and 700°C, the power densities of the Ni infiltrated and GDC infiltrated cell gradually approach to the Ni-GDC infiltrated cells. This indicates that GDC itself has catalytic properties and the GDC nanoparticles also contribute additional TPBs. In a relative sense, since additional TPBs become more active at lower temperatures, the nature of the TPBs matter less, making the performance of Ni-infiltrated and GDC-infiltrated samples to converge.

The Nyquist plots (Figure 30d-30f) agree with I-V results and show that the polarization resistances of all infiltrated cells decrease dramatically as operation temperature decreases. The ohmic resistances of the GDC infiltrated and Ni-GDC infiltrated cell are slightly improved. This suggests that the existence of GDC is beneficial to the flow of oxygen ions in the anode to mitigate the electrode ohmic loss. However, the Bode plots shown in Figure 30g-30i reveal that the infiltrants cause the slowest peak to shift to lower frequency indicating an increase in mass transfer resistance, especially for the GDC infiltrated cell. As mentioned in Chapter 2.2.3, when exposed to a reducing atmosphere, the volume reduction from NiO to Ni opens pores for better gas diffusion and leads to a decrease in mass transfer resistance. However, there is no volume change of GDC during reduction process leading to a higher mass transfer resistance.

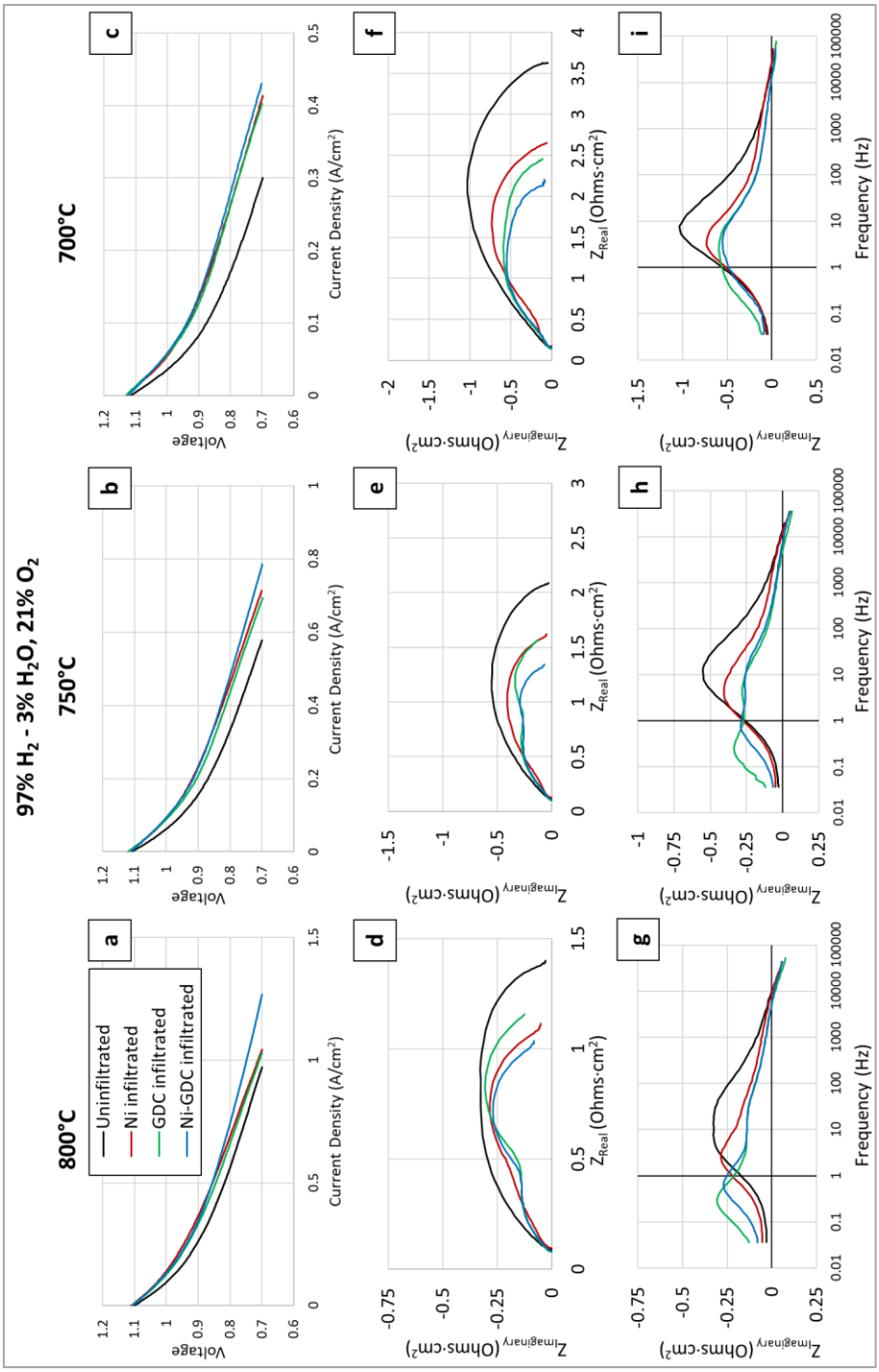

Figure 30. Electrochemical performance measurements of uninfiltrated, Ni infiltrated, GDC infiltrated, and Ni-GDC infiltrated cells recorded at 800°C, 750°C, and 700°C with 3% humidified hydrogen flowing over the anode and dry air flowing over the cathode. Measurements include a)-c) I-V scans, and EIS measurements plotted in d)-f) Nyquist, and g)-i) and Bode formats.

Table 9. Performance data from EIS and I-V measurements of uninfiltrated, Ni infiltrated, GDC infiltrated, and Ni-GDC infiltrated cells.

Cell:		Uninfiltrated	Ni infiltrated		GDC infiltrated		Ni-GDC infiltrated	
Measurement:	Temp.:	Value:	Value:	Change:	Value:	Change:	Value:	Change:
R_{Pol} ($\Omega \cdot cm^2$) (97% H_2 - 3% H_2O, 21% O_2)	800°C	1.31	1.02	-22%	1.08	-18%	0.95	-27%
	750°C	1.97	1.49	-24%	1.47	-26%	1.23	-38%
	700°C	3.47	2.49	-28%	2.31	-33%	2.05	-41%
R_{Ohmic} ($\Omega \cdot cm^2$) (97% H_2 - 3% H_2O, 21% O_2)	800°C	0.09	0.09	+5%	0.08	-14%	0.08	-10%
	750°C	0.12	0.12	+7%	0.10	-15%	0.11	-8%
	700°C	0.16	0.17	+5%	0.14	-13%	0.15	-5%
Power density at 750 mV ($W \cdot cm^{-2}$) (97% H_2 - 3% H_2O, 21% O_2)	800°C	0.57	0.65	+14%	0.63	+11%	0.74	+30%
	750°C	0.34	0.44	+30%	0.42	+25%	0.47	+39%
	700°C	0.17	0.25	+47%	0.25	+46%	0.27	+56%

The results of the long-term stability test are shown in Figure 31. All cells experience competing effects of activation and degradation during the stability study. The initial voltages of all cells are consistent with the voltages in Figure 30a. The Ni infiltrated cell and uninfiltrated cell have almost the same performance at the end of 120 hours suggesting that Ni nanoparticles are mostly degraded. The GDC infiltrated cell shows better performance than the Ni infiltrated after 40 hours of operation. This

indicates that GDC has better stability than Ni, and that GDC itself has good catalytic properties for the anodic electrochemical reaction. The Ni-GDC infiltrated cell maintains the best performance. It implies both Ni and GDC are beneficial to cell performance and GDC effectively stabilize the Ni nanoparticles.

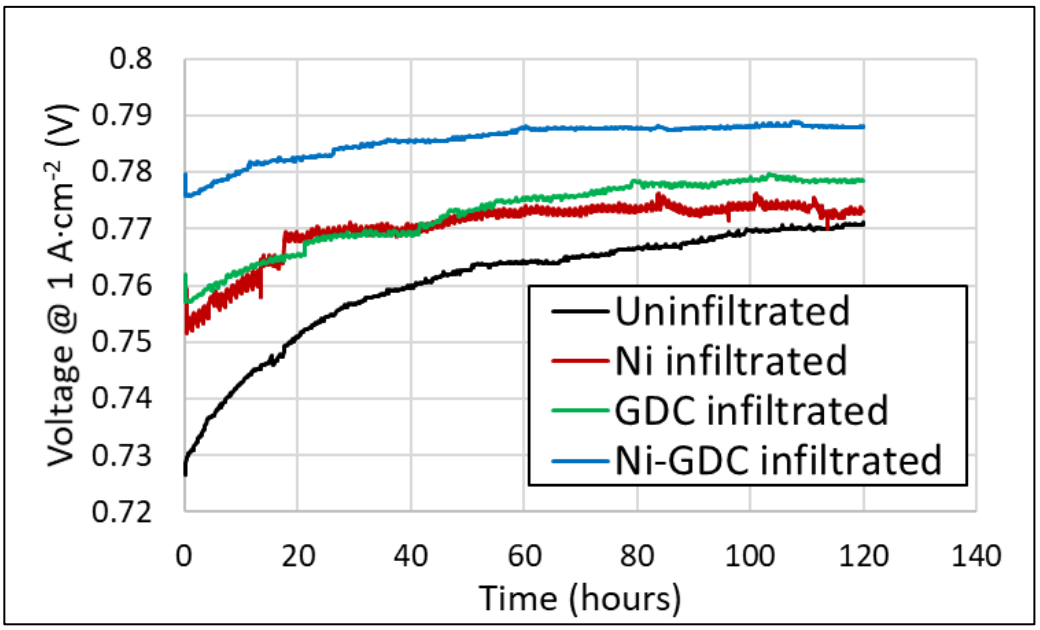

Figure 31. Long-term electrochemical performance of uninfiltrated, Ni infiltrated, GDC infiltrated, and Ni-GDC infiltrated cells.

5.3.3 Anode microstructures after electrochemical testing

By comparing the microstructural differences between the electrochemically active and inactive region of all infiltrated cells, the effects of the electrochemical current and the anodic reactions on particle microstructure can be revealed. For the Ni infiltrated cell, the electrochemical current and the anodic reactions cause well distributed nano-sized Ni particles to aggregate into larger ones (Figure 32b-32c). The Ni particles surface coverage decreases dramatically leading to loss in functionality. This corroborates with the long-term stability results that the electrochemical performance of the Ni infiltrated

cell approaches to that of the uninfiltrated cell at the end of 120 hours. However, for the GDC infiltrated and Ni-GDC infiltrated cell, the electrochemical current and the anodic reactions cause the infiltrants to wet on the Ni-YSZ substrate surface forming well-connected and film-shaped networks (Figure 32d-32g). This is potentially beneficial for maintaining the stability of infiltrants, because the well-connected networks distribute the electrochemical reactions into larger area. The heat and humidity generated from the electrochemical reactions, accelerating the coarsening of Ni particles [11,80–82], are distributed to a wider space instead of some hot spots.

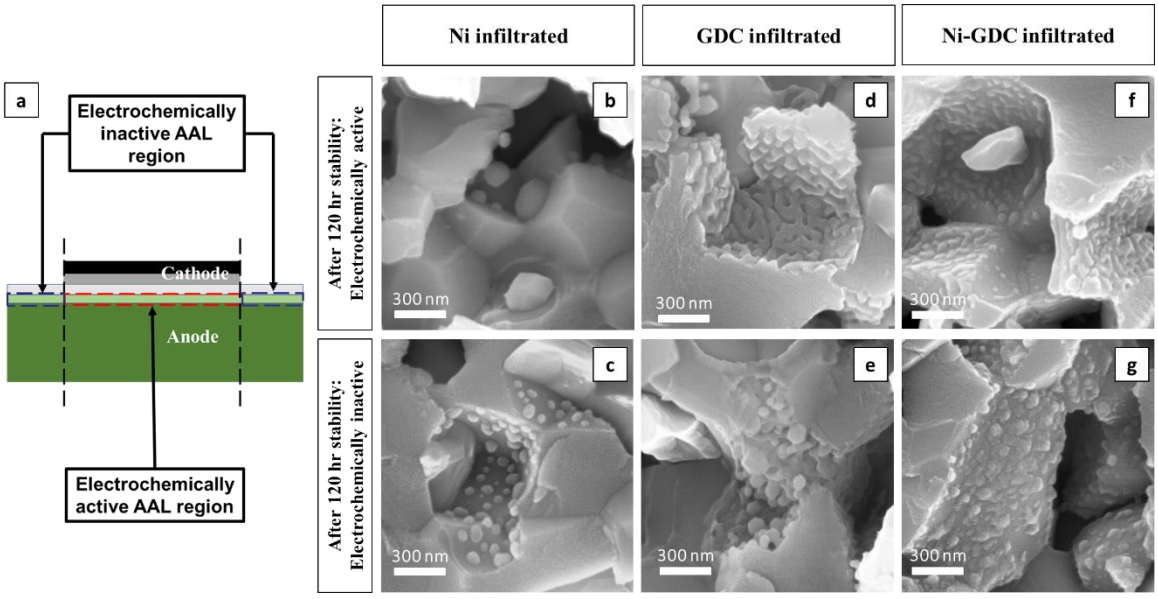

Figure 32. a) Schematic of the cell showing the locations of 'electrochemically active' (under cathode) and 'electrochemically inactive' (not under cathode) regions in the AAL. Fracture cross-section SEM images of infiltrated Ni, GDC, and Ni-GDC nanoparticles in the b) d) f) 'electrochemically active', and c) e) g) 'electrochemically inactive' regions of the AAL.

The porosity profile of the entire anode, shown in Figure 33, highlights the effect of infiltrants on pore volume throughout the electrode. The average porosities of all cells and the porosity changes of the infiltrated cells compared to the uninfiltrated cell are listed in

Table 10. The uninfiltrated cell in general has a uniform porosity profile. The porosity profiles of all infiltrated cells have similar trends. The porosity change of the GDC infiltrated cell is the highest among all infiltrated cells, and the porosity change of the Ni-GDC infiltrated cell is higher than that of the Ni infiltrated cell. The relationship of porosity profiles of the three infiltrated cells corroborates well with results of the Bode plots.

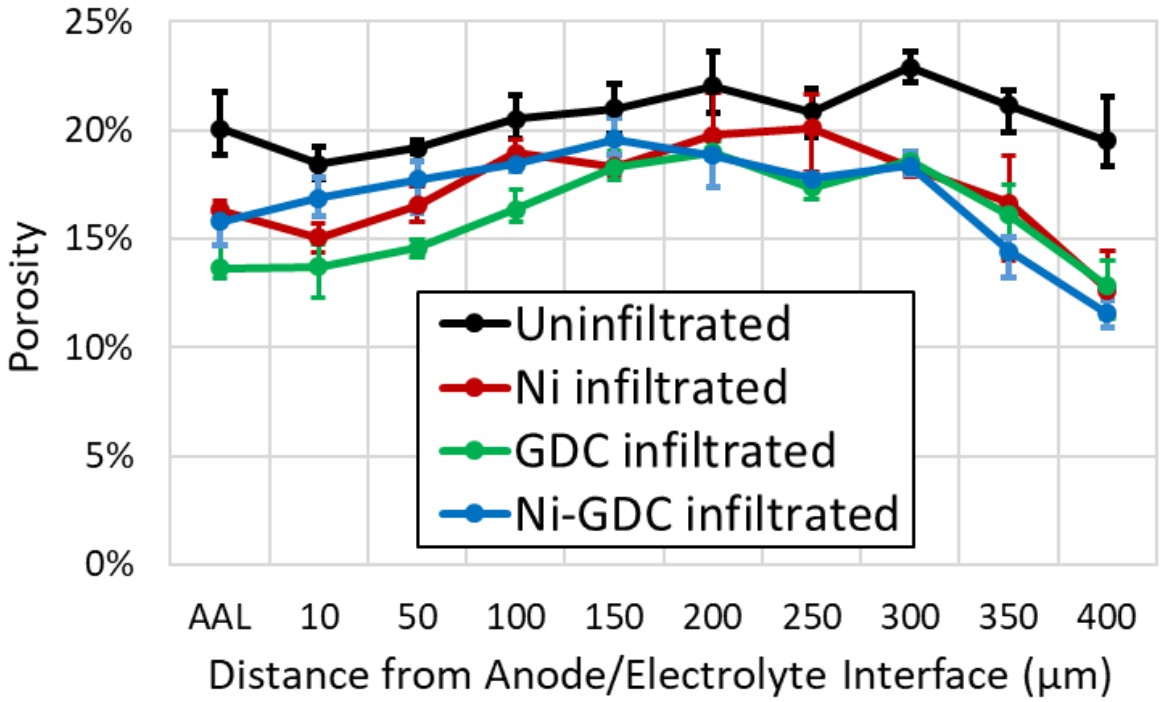

Figure 33. Measured porosity profile across the anode cross-section of uninfiltrated, Ni infiltrated, GDC infiltrated, and Ni-GDC infiltrated cells.

Table 10. Porosity profile data of uninfiltrated, Ni infiltrated, GDC infiltrated, Ni-GDC infiltrated cells.

Cell:	Un-infiltrated	Ni infiltrated		GDC infiltrated		Ni-GDC infiltrated	
Measurement	Value	Value	Change	Value	Change	Value	Change
Average porosity	20.6%	17.4%	-15.8%	16.3%	-20.9%	17.1%	-17.3%

5.4 Conclusions

Uninfiltrated, Ni infiltrated, GDC infiltrated, and Ni-GDC infiltrated Ni-YSZ cermet anode cells were studied. Particle microstructures of AALs exposed to as reduced, high temperature, and high temperature and humidity conditions were recorded and compared. The results show that infiltrants of GDC and Ni-GDC maintain small particle sizes and good connectivity under all conditions. The initial electrochemical performance indicates that all infiltrated cells exhibit increased active TPB density and improved cell performance at temperatures of 800°C, 750°C, and 700°C. The existence of GDC mitigates the ohmic loss, but increases mass transfer resistance. Both initial and long-term electrochemical performance shows Ni-GDC has the best performance. This is because the infiltration of Ni-GDC provides more active TPB density than Ni or GDC so that it significantly increases charge transfer kinetics. Also, GDC effectively stabilizes Ni particles to mitigate Ni coarsening, thereby maintaining superior cell performance. Therefore, infiltration of Ni-GDC into Ni-YSZ cermet anode can effectively improve overall cell performance at intermediate temperatures and maintain the performance gains from anode infiltration for a long period of time.

6. Conclusions

In this work, Ni-YSZ cermet anodes were liquid infiltrated with Ni, Ni-LSNC, GDC, and Ni-GDC to increase the anodic TPB density for improvement in cell performance. Table 11 summarizes the materials property of all infiltrants and the substrates used in this work. Figure 34 summarizes in schematic form, the mechanisms of increased active TPBs due to the different infiltrations. In a Ni-YSZ cermet anode, the active TPBs are located within the range between the anode/electrolyte interface and the farthest distance that the oxygen ions can be transported away from the interface. The active TPBs in a Ni-YSZ cermet anode is marked as red dots in Figure 34a and 34b. For the Ni infiltration in Chapter 3 (Figure 34c), in the as deposited state, the Ni nanoparticles next to edges between Ni and YSZ grain are activated and their interfaces with YSZ grain are active TPBs (Figure 34d). After the Ni spreading procedure, at temperature, the Ni nanoparticles connect, and all the newly formed TPBs associated with the connected nanoparticles become active (Figure 34e and 34f). For the Ni-LSNC infiltrated cell (Figure 34g) in Chapter 4, the LSNC electronically connects the Ni nanoparticles to Ni grain extending the electronic transport distance (Figure 34h). Therefore, more Ni nanoparticles are activated and contribute to the electrochemical reactions. For the GDC infiltrated cell in Chapter 5 (Figure 34i), since the ionic conductivity of GDC is higher than YSZ, the oxygen ions can move further away from the anode/electrolyte interface activating more TPBs in the Ni-YSZ substrate. In addition, as GDC is a MIEC, the interface between GDC and gas phase, known as double phase boundary (2PB), can potentially be sites for electrocatalysis as well (Figure 34j) [84,85]. For the Ni-GDC

infiltrated cell in Chapter 5 (Figure 34k), the GDC is able to both extend the oxygen ion transport distance and electronically connect the Ni nanoparticles near to Ni/YSZ interface (Figure 34l). Therefore, the substantially increased 2PB area in the presence of Ni leads to the Ni-GDC infiltrated cell having the best cell performance.

Table 11. Material properties of Ni, YSZ, LSNC, and GDC.

Material	Electronic conductivity	Oxygen ionic conductivity	Electrocatalytic activity
Ni	High [86]	None	High [87]
YSZ	None	High [88]	None
LSNC	Middle [76]	N/A	N/A
GDC	Low [4]	High [88]	Low [84,85]

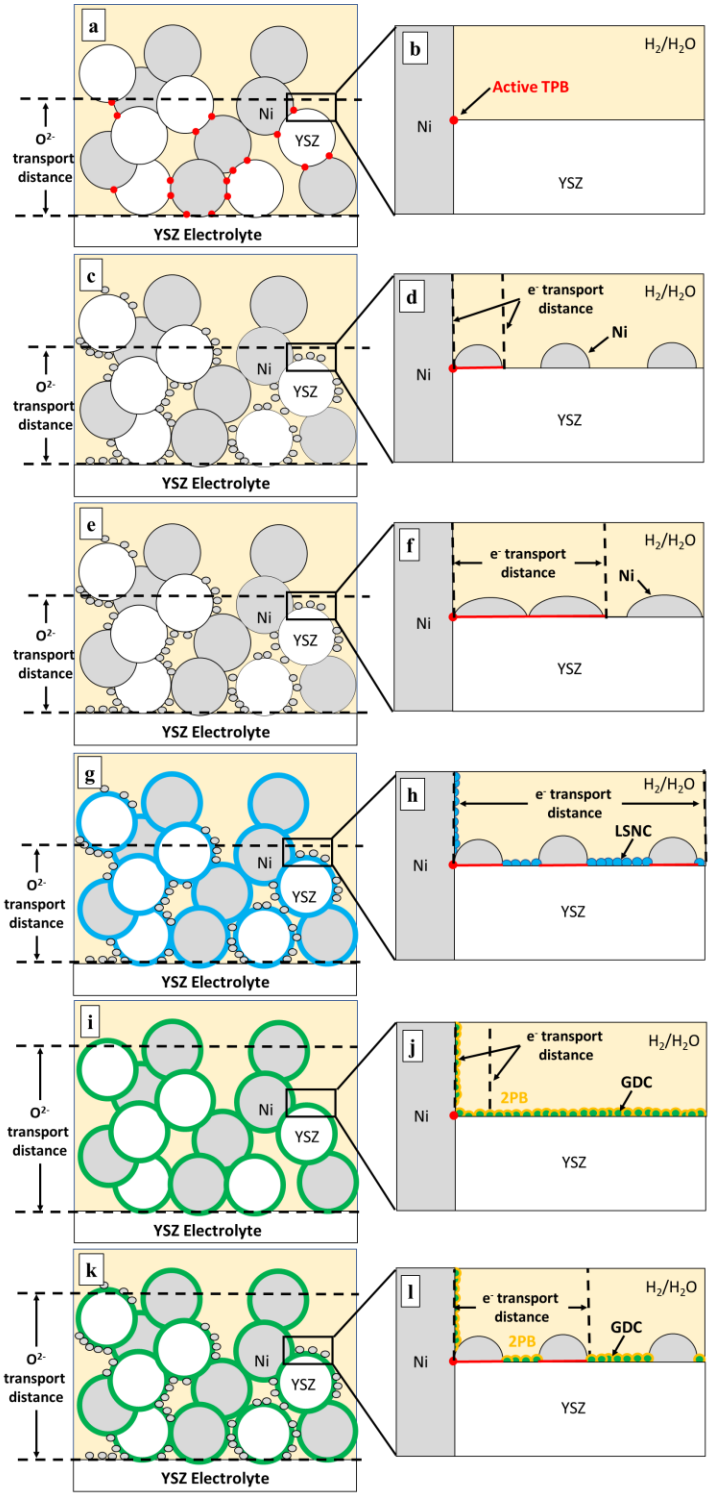

Figure 34. Schematics and zoomed-in views of a)-b) uninfiltrated, c)-d) as-infiltrated Ni, e)-f) infiltrated Ni after Ni spreading, g)-h) co-infiltrated Ni-LSNC, i)-j) infiltrated GDC, and k)-l) co-infiltrated Ni-GDC in Ni-YSZ cermet anodes.

Results presented in Chapter 3 show that Ni-YSZ cermet anodes infiltrated with Ni nanoparticles improve the electrochemical performance of the cell. The Ni nanoparticles increase the TPB density of the Ni-YSZ anode by a factor of four. The improved electrochemical results indicate that infiltration primarily lowers charge transfer resistance in the anode. However, the particle statistics reveals that Ni nanoparticle coarsening occurs during the electrochemical testing. And also, the isolated Ni nanoparticles away from the edge of Ni and YSZ grain need to be electronically connected by the Ni-spreading procedure to activate the additional TPBs.

Results presented in Chapter 4 show that Ni can be co-infiltrated with a MIEC into Ni-YSZ cermet anode with good surface coverage to improve stability and utilization of the nanoparticles. Two oxides were chosen based on their chemical stability and conductivity in the anode operation environments: GDC, a predominantly an ionic conductor, and LSNC, a predominantly electronic conductor. The exposures to dry and humid hydrogen atmospheres demonstrated that the additional oxide phases inhibit Ni nanoparticle coarsening. The electrochemical results show that both Ni-GDC and Ni-LSNC infiltrated cells exhibited improved anodic charge transfer kinetics, but the Ni-LSNC cell also suffers from substantially increased mass transfer resistance. Ni-GDC was shown to be a more effective infiltrant for Ni-YSZ cermet anodes.

Chapter 5 discusses the effects of infiltration of Ni, GDC, and Ni-GDC in Ni-YSZ cermet anodes on the long-term electrochemical performance of the cells. The initial electrochemical performance indicates that all infiltrated cells exhibit increased active TPB density and improved cell performance at 800°C, 750 °C, and 700°C. GDC

infiltration mitigates ohmic loss, but increases anodic mass transfer resistance due to significant pore coverage, especially in the AAL. Both initial and long-term electrochemical performance shows infiltration of Ni-GDC infiltration into Ni-YSZ cermet anodes can best improve overall cell performance at intermediate temperatures and maintain the performance gains over long periods of time.

7. Suggestions for future work

Future work on this topic can focus on:

1. Optimization of the needs to consider the optimal molar ratio between Ni and GDC; the optimal molarity of infiltration solution to balance the viscosity of infiltration solution and the number of rounds of infiltration; and the optimal load of infiltrants to balance the effects of charge transfer and mass transfer resistance.

2. Explore the resistance of Ni-GDC infiltrated Ni-YSZ cermet anode to fuel impurities. The infiltrated GDC shows good coverage on both Ni substrates and Ni nanoparticles. This behavior may mitigate the effects of carbon coking and sulfur poisoning caused by fuel impurities.

3. Explore alternative MIECs to co-infiltrated with Ni for Ni-YSZ anode infiltration. The desired MIECs should have higher electronic and ionic conductivity than GDC. The aim is to facilitate the flow of electrons and oxygen ions for better cell performance.

BIBLIOGRAPHY

[1] Energy Transition Group, Electric efficiency vs. power generation of fuel cells and internal combustion, (2013). http://www.energytransitiongroup.com/vision/localenergy.html.

[2] F.P. R. O'Hayre, S. Cha, W. Colella, Fuel Cell Fundamentals, 2016. doi:10.1002/9781119191766.

[3] S. Mekhilef, R. Saidur, A. Safari, Comparative study of different fuel cell technologies, Renewable and Sustainable Energy Reviews. 16 (2012) 981–989. doi:10.1016/j.rser.2011.09.020.

[4] T. Shimonosono, Y. Hirata, Y. Ehira, S. Sameshima, T. Horita, Electronic conductivity measurement of Gd and Sm doped ceria ceramics by Hebb-Wagner method, Journal of the Ceramic Society of Japan. 621 (2004) 616–621.

[5] X. Gao, J. Liu, S. Ye, D. Song, Y. Zhang, Hydrogen adsorption of metal nickel and hydrogen storage alloy electrodes, Journal of Alloys and Compounds. 254 (1997) 515–519.

[6] C. Sun, R. Hui, J. Roller, Cathode materials for solid oxide fuel cells : a review, Journal of Solid State Electrochemistry. (2010) 1125–1144. doi:10.1007/s10008-009-0932-0.

[7] U.S. Department of Eenrgy, Technology Program Plan Solid Oxide Fuel Cells, Solid Oxide Fuel Cell Technology Program Plan. (2013).

[8] W. Nernst, US Patent 685:730, 1899.

[9] H. Baur, E. and Preis, Über Brennstoff-Ketten mit Festleitern, Zeitschrift Für Elektrochemie Und Angewandte Physikalische Chemie. 43 (1937) 727–732. doi:10.1002/bbpc.19370430903.

[10] F. Fleischhauer, R. Bermejo, R. Danzer, A. Mai, T. Graule, J. Kuebler, Strength of an electrolyte supported solid oxide fuel cell, Journal of Power Sources. 297 (2015) 158–167. doi:10.1016/j.jpowsour.2015.07.075.

[11] L. Holzer, B. Münch, B. Iwanschitz, M. Cantoni, T. Hocker, T. Graule, Quantitative relationships between composition, particle size, triple phase boundary length and surface area in nickel-cermet anodes for solid oxide fuel cells, Journal of Power Sources. 196 (2011) 7076–7089. doi:10.1016/j.jpowsour.2010.08.006.

[12] J.T.S. Irvine, D. Neagu, M.C. Verbraeken, C. Chatzichristodoulou, C. Graves,

M.B. Mogensen, Evolution of the electrochemical interface in high-temperature fuel cells and electrolysers, Nature Energy. 1 (2016) 15014. doi:10.1038/nenergy.2015.14.

[13] S. Li, A.C. Lee, R.E. Mitchell, T.M. Gür, Direct carbon conversion in a helium fluidized bed fuel cell, Solid State Ionics. 179 (2008) 1549–1552. doi:10.1016/j.ssi.2007.11.006.

[14] M. Ihara, S. Hasegawa, Quickly rechargeable direct carbon solid oxide fuel cell, Journal of The Electrochemical Society. (2006) 1544–1546. doi:10.1149/1.2203948.

[15] D. Cao, Y. Sun, G. Wang, Direct carbon fuel cell: Fundamentals and recent developments, Journal of Power Sources. 167 (2007) 250–257. doi:10.1016/j.jpowsour.2007.02.034.

[16] S.L. Jain, Y. Nabae, B.J. Lakeman, K.D. Pointon, J.T.S. Irvine, Solid state electrochemistry of direct carbon/air fuel cells, Solid State Ionics. 179 (2008) 1417–1421. doi:10.1016/j.ssi.2008.01.078.

[17] K. Sasaki, K. Haga, T. Yoshizumi, D. Minematsu, E. Yuki, R. Liu, Chemical durability of Solid Oxide Fuel Cells: Influence of impurities on long-term performance, Journal of Power Sources. 196 (2011) 9130–9140. doi:10.1016/j.jpowsour.2010.09.122.

[18] Y. Jin, H. Yasutake, K. Yamahara, M. Ihara, Improved electrochemical properties of Ni/YSZ anodes infiltrated by proton conductor SZY in solid oxide fuel cells with dry methane fuel: Dependence on amount of SZY, Chemical Engineering Science. 65 (2010) 597–602. doi:10.1016/j.ces.2009.06.033.

[19] S. Jung, C. Lu, H. He, K. Ahn, R.J. Gorte, J.M. Vohs, Influence of composition and Cu impregnation method on the performance of Cu/CeO2/YSZ SOFC anodes, Journal of Power Sources. 154 (2006) 42–50. doi:10.1016/j.jpowsour.2005.04.018.

[20] K. Sasaki, K. Susuki, A. Iyoshi, M. Uchimura, N. Imamura, H2S poisoning of solid oxide fuel cells, Journal of The Electrochemical Society. (2006) 2023–2029. doi:10.1149/1.2336075.

[21] S. Zha, Z. Cheng, M. Liu, Sulfur poisoning and regeneration of Ni-based anodes in solid oxide fuel cells, Journal of The Electrochemical Society. (2007) 201–206. doi:10.1149/1.2404779.

[22] J. Vila-comamala, M. Liu, M. Liu, W.K.S. Chiu, Imaging of sulfur poisoning-induced degradation in a Ni-YSZ anode of solid oxide fuel cells, Scientific Reports. (2014) 1–7. doi:10.1038/srep05246.

[23] R.J. Gorte, J.M. Vohs, Nanostructured anodes for solid oxide fuel cells, Current Opinion in Colloid and Interface Science. 14 (2009) 236–244. doi:10.1016/j.cocis.2009.04.006.

[24] H. Kurokawa, T.Z. Sholklapper, C.P. Jacobson, L.C. De Jonghe, S.J. Visco, Ceria nanocoating for sulfur tolerant Ni-based anodes of solid oxide fuel cells, Electrochemical and Solid-State Letters. (2007) 135–138. doi:10.1149/1.2748630.

[25] Y. Chen, J. Bunch, C. Jin, C. Yang, F. Chen, Performance enhancement of Ni-YSZ electrode by impregnation of Mo0.1Ce0.9O2, Journal of Power Sources. 204 (2012) 40–45. doi:10.1016/j.jpowsour.2012.01.019.

[26] M. Cassidy, G. Lindsay, K. Kendall, The reduction of nickel-zirconia cermet anodes and the effects on supported thin electrolytes, Lournal of Power Sources. 61 (1996) 189–192.

[27] D. Sarantaridis, A. Atkinson, Redox cycling of Ni-based solid oxide fuel cell anodes : a review, Fuel Cells. (2007) 246–258. doi:10.1002/fuce.200600028.

[28] T. Klemensø, C. Chung, P.H. Larsen, M. Mogensen, The mechanism behind redox instability of anodes in high-temperature SOFCs, Journal of The Electrochemical Society. (2005) 2186–2192. doi:10.1149/1.2048228.

[29] B. Hua, W. Zhang, M. Li, X. Wang, B. Chi, J. Pu, J. Li, Improved microstructure and performance of Ni-based anode for intermediate temperature solid oxide fuel cells, Journal of Power Sources. 247 (2014) 170–177. doi:10.1016/j.jpowsour.2013.08.060.

[30] S. Futamura, Y. Tachikawa, J. Matsuda, S.M. Lyth, Y. Shiratori, Alternative Ni-impregnated mixed ionic-electronic conducting anode for SOFC operation at high fuel utilization, Journal of the Electrochemical Society. 164 (2017) 3055–3063. doi:10.1149/2.0071710jes.

[31] S.P. Jiang, Y. Ye, T. He, S.B. Ho, Nanostructured palladium–La0.75Sr0.25Cr0.5Mn0.5O3/Y2O3–ZrO2 composite anodes for direct methane and ethanol solid oxide fuel cells, Journal of Power Sources. 185 (2008) 179–182. doi:10.1016/j.jpowsour.2008.06.099.

[32] S.P. Jiang, Nanoscale and nano-structured electrodes of solid oxide fuel cells by infiltration: Advances and challenges, International Journal of Hydrogen Energy. 37 (2011) 449–470. doi:10.1016/j.ijhydene.2011.09.067.

[33] Z. Liu, B. Liu, D. Ding, M. Liu, F. Chen, C. Xia, Fabrication and modification of solid oxide fuel cell anodes via wet impregnation/infiltration technique, Journal of Power Sources. 237 (2013) 243–259. doi:10.1016/j.jpowsour.2013.03.025.

[34] A. Bertei, J.G. Pharoah, W. Gawel, C. Nicolella, Microstructural modeling and effective properties of infiltrated SOFC electrodes, ECS Transactions. 57 (2013) 2527–2536, 10 pp. doi:10.1149/05701.2527ecst.

[35] T. Løye, J. Hjelm, P. Blennow, C. Graves, Reactivating the Ni-YSZ electrode in solid oxide cells and stacks by infiltration, Journal of Power Sources. 378 (2018) 685–690. doi:10.1016/j.jpowsour.2018.01.021.

[36] P. Keyvanfar, V. Birss, Optimization of infiltration techniques used to construct Ni/YSZ anodes, Journal of the Electrochemical Society. 161 (2014) F660–F667. doi:10.1149/2.056405jes.

[37] A. Bertei, E. Ruiz-Trejo, K. Kareh, V. Yufit, X. Wang, F. Tariq, N.P. Brandon, The fractal nature of the three-phase boundary: A heuristic approach to the degradation of nanostructured solid oxide fuel cell anodes, Nano Energy. 38 (2017) 526–536. doi:10.1016/j.nanoen.2017.06.028.

[38] M. Kishimoto, M. Lomberg, E. Ruiz-Trejo, N.P. Brandon, Enhanced triple-phase boundary density in infiltrated electrodes for solid oxide fuel cells demonstrated by high-resolution tomography, Journal of Power Sources. 266 (2014) 291–295. doi:10.1016/j.jpowsour.2014.05.038.

[39] M. Lomberg, E. Ruiz-Trejo, G. Offer, N.P. Brandon, Characterization of Ni-infiltrated GDC electrodes for solid oxide cell applications, Journal of the Electrochemical Society. 161 (2014) F899–F905. doi:10.1149/2.0501409jes.

[40] J. Nielsen, T. Klemenso, P. Blennow, Detailed impedance characterization of a well performing and durable Ni:CGO infiltrated cermet anode for metal-supported solid oxide fuel cells, Journal of Power Sources. 219 (2012) 305–316. doi:10.1016/j.jpowsour.2012.07.031.

[41] X. Zhu, C. Guan, Z. Lü, B. Wei, Y. Li, W. Su, A rapid preparation of acicular Ni impregnated anode with enhanced conductivity and operational stability, Journal of Power Sources. 256 (2014) 424–429. doi:10.1016/j.jpowsour.2014.01.058.

[42] B. Hua, W. Zhang, M. Li, X. Wang, B. Chi, J. Pu, J. Li, Improved microstructure and performance of Ni-based anode for intermediate temperature solid oxide fuel cells, Journal of Power Sources. 247 (2014) 170–177. doi:10.1016/j.jpowsour.2013.08.060.

[43] T. Klemensø, K. Thydén, M. Chen, H.J. Wang, Stability of Ni-yttria stabilized zirconia anodes based on Ni-impregnation, Journal of Power Sources. 195 (2010) 7295–7301. doi:10.1016/j.jpowsour.2010.05.047.

[44] E. C. Miller, Q. Sherman, Z. Gao, P.W. Voorhees, S. A. Barnett, Stability of

nickel-infiltrated anodes in intermediate temperature SOFCs, ECS Transactions. 68 (2015) 1245–1254. doi:10.1149/06801.1245ecst.

[45] A.N. Busawon, D. Sarantaridis, A. Atkinson, Ni infiltration as a possible solution to the redox problem of SOFC anodes, Electrochemical and Solid-State Letters. 11 (2008) B186. doi:10.1149/1.2959078.

[46] M. V. Ananyev, D.I. Bronin, D.A. Osinkin, V.A. Eremin, R. Steinberger-Wilckens, L.G.J. De Haart, J. Mertens, Characterization of Ni-cermet degradation phenomena I. Long term resistivity monitoring, image processing and X-ray fluorescence analysis, Journal of Power Sources. 286 (2015) 414–426. doi:10.1016/j.jpowsour.2015.03.168.

[47] M.S. Khan, S.B. Lee, R.H. Song, J.W. Lee, T.H. Lim, S.J. Park, Fundamental mechanisms involved in the degradation of nickel-yttria stabilized zirconia (Ni-YSZ) anode during solid oxide fuel cells operation: A review, Ceramics International. 42 (2015) 35–48. doi:10.1016/j.ceramint.2015.09.006.

[48] M. Kishimoto, H. Iwai, M. Saito, H. Yoshida, Quantitative evaluation of solid oxide fuel cell porous anode microstructure based on focused ion beam and scanning electron microscope technique and prediction of anode overpotentials, Journal of Power Sources. 196 (2011) 4555–4563. doi:10.1016/j.jpowsour.2010.12.100.

[49] A. Faes, A. Hessler-Wyser, D. Presvytes, C.G. Vayenas, J. Vanherle, Nickel-zirconia anode degradation and triple phase boundary quantification from microstructural analysis, Fuel Cells. 9 (2009) 841–851. doi:10.1002/fuce.200800147.

[50] L. Holzer, B. Münch, B. Iwanschitz, M. Cantoni, T. Hocker, T. Graule, Quantitative relationships between composition, particle size, triple phase boundary length and surface area in nickel-cermet anodes for solid oxide fuel cells, Journal of Power Sources. 196 (2011) 7076–7089. doi:10.1016/j.jpowsour.2010.08.006.

[51] K.T. Lee, N.J. Vito, E.D. Wachsman, Comprehensive quantification of Ni-Gd0.1Ce0.9O1.95 anode functional layer microstructures by three-dimensional reconstruction using a FIB/SEM dual beam system, Journal of Power Sources. 228 (2013) 220–228. doi:10.1016/j.jpowsour.2012.11.117.

[52] J.S. Cronin, Y.K. Chen-Wiegart, J. Wang, S. a. Barnett, Three-dimensional reconstruction and analysis of an entire solid oxide fuel cell by full-field transmission X-ray microscopy, Journal of Power Sources. 233 (2013) 174–179. doi:10.1016/j.jpowsour.2013.01.060.

[53] V. Sonn, A. Leonide, E. Ivers-Tiffée, Combined deconvolution and CNLS fitting approach applied on the impedance response of technical Ni/8YSZ cermet electrodes, Journal of The Electrochemical Society. 155 (2008) B675. doi:10.1149/1.2908860.

[54] A. Leonide, Y. Apel, E. Ivers-Tiffee, SOFC modeling and parameter identification by means of impedance spectroscopy, ECS Transactions. 19 (2009) 81–109. doi:10.1149/1.3247567.

[55] C. Boigues Muñoz, D. Pumiglia, S.J. McPhail, D. Montinaro, G. Comodi, G. Santori, M. Carlini, F. Polonara, More accurate macro-models of solid oxide fuel cells through electrochemical and microstructural parameter estimation - Part I: Experimentation, Journal of Power Sources. 294 (2015) 658–668. doi:10.1016/j.jpowsour.2015.06.118.

[56] C. Boigues-Muñoz, D. Pumiglia, S.J. McPhail, G. Santori, D. Montinaro, G. Comodi, M. Carlini, F. Polonara, More accurate macro-models of solid oxide fuel cells through electrochemical and microstructural parameter estimation - Part II: Parameter estimation, Journal of Power Sources. 286 (2015) 321–329. doi:10.1016/j.jpowsour.2015.03.129.

[57] C.H. Law, S.W. Sofie, Anchoring of infiltrated nickel electro-catalyst by addition of aluminum titanate, Journal of the Electrochemical Society. 158 (2011) B1137–B1141. doi:10.1149/1.3610226.

[58] K.J. Yoon, P. Zink, S. Gopalan, U.B. Pal, Polarization measurements on single-step co-fired solid oxide fuel cells (SOFCs), Journal of Power Sources. 172 (2007) 39–49. doi:10.1016/j.jpowsour.2007.03.003.

[59] J.-C. Njodzefon, D. Klotz, A. Kromp, A. Weber, E. Ivers-Tiffee, Electrochemical modeling of the current-voltage characteristics of an SOFC in fuel cell and electrolyzer operation modes, Journal of the Electrochemical Society. 160 (2013) F313–F323. doi:10.1149/2.018304jes.

[60] W. Kong, H. Zhu, Z. Fei, Z. Lin, A modified dusty gas model in the form of a Fick's model for the prediction of multicomponent mass transport in a solid oxide fuel cell anode, Journal of Power Sources. 206 (2012) 171–178. doi:10.1016/j.jpowsour.2012.01.107.

[61] K.J. Yoon, S. Gopalan, U.B. Pal, Effect of fuel composition on performance of single-step cofired SOFCs, Journal of The Electrochemical Society. (2007) 1080–1087. doi:10.1149/1.2769826.

[62] P. Gasper, Y. Lu, S.N. Basu, S. Gopalan, U.B. Pal, Effect of anodic current density on the spreading of infiltrated nickel nanoparticles in nickel-yttria stabilized

zirconia cermet anodes, Journal of Power Sources. 410–411 (2019) 196–203. doi:10.1016/j.jpowsour.2018.11.002.

[63] H. Iwai, N. Shikazono, T. Matsui, H. Teshima, M. Kishimoto, R. Kishida, D. Hayashi, K. Matsuzaki, D. Kanno, M. Saito, H. Muroyama, K. Eguchi, N. Kasagi, H. Yoshida, Quantification of SOFC anode microstructure based on dual beam FIB-SEM technique, Journal of Power Sources. 195 (2010) 955–961. doi:10.1016/j.jpowsour.2009.09.005.

[64] B.F. Lasagni, A. Lasagni, M. Engstler, H.P. Degischer, F. Mücklich, Nano-characterization of cast structures by FIB-tomography, Advanced Engineering Materials. (2008) 62–66. doi:10.1002/adem.200700249.

[65] M. Schaffer, J. Wagner, B. Schaffer, M. Schmied, H. Mulders, Automated three-dimensional X-ray analysis using a dual-beam FIB, Ultramicroscopy. 107 (2007) 587–597. doi:10.1016/j.ultramic.2006.11.007.

[66] Z. Jiao, N. Shikazono, Study on the effects of polarization on local morphological change of nickel at active three-phase-boundary using patterned nickel-film electrode in solid oxide fuel cell anode, Acta Materialia. 135 (2017) 124–131. doi:10.1016/j.actamat.2017.05.051.

[67] A. Bertei, E. Ruiz-trejo, K. Kareh, V. Yu, X. Wang, F. Tariq, N.P. Brandon, The fractal nature of the three-phase boundary : A heuristic approach to the degradation of nanostructured solid oxide fuel cell anodes, Nano Energy. 38 (2017) 526–536. doi:10.1016/j.nanoen.2017.06.028.

[68] T. Klemensø, K. Thydén, M. Chen, H. Wang, Stability of Ni–yttria stabilized zirconia anodes based on Ni-impregnation, Journal of Power Sources. 195 (2010) 7295–7301. doi:10.1016/j.jpowsour.2010.05.047.

[69] P. Keyvanfar, V. Birss, Optimization of infiltration techniques used to construct Ni/YSZ anodes, Journal of The Electrochemical Society. 161 (2014) 660–667. doi:10.1149/2.056405jes.

[70] E.F. Hardjo, D.S. Monder, K. Karan, An effective property model for infiltrated electrodes in solid oxide fuel cells, Journal of The Electrochemical Society. 161 (2014). doi:10.1149/2.036401jes.

[71] P.I. Cowin, C.T.G. Petit, R. Lan, J.T.S. Irvine, S. Tao, Recent progress in the development of anode materials for solid oxide fuel cells, Advanced Energy Materials. (2011) 314–332. doi:10.1002/aenm.201100108.

[72] S.P. Jiang, Y.Y. Duan, J.G. Love, Fabrication of high-performance Ni/Y2O3-ZrO2 cermet anodes of solid oxide fuel cells by ion impregnation, Journal of The

Electrochemical Society. (2002) 6–14. doi:10.1149/1.1497982.

[73] T. Løye, J. Hjelm, P. Blennow, C. Graves, Reactivating the Ni-YSZ electrode in solid oxide cells and stacks by infiltration, Journal of Power Sources. 378 (2018) 685–690. doi:10.1016/j.jpowsour.2018.01.021.

[74] N. Mahato, A. Banerjee, A. Gupta, S. Omar, K. Balani, Progress in materials science progress in material selection for solid oxide fuel cell technology : A review, Progress in Materials Science. 72 (2015) 141–337. doi:10.1016/j.pmatsci.2015.01.001.

[75] X.M. Ge, S.H. Chan, Q.L. Liu, Q. Sun, Solid oxide fuel cell anode materials for direct hydrocarbon utilization, Advanced Energy Materials. 2 (2012) 1156–1181. doi:10.1002/aenm.201200342.

[76] Y. Sun, J. Li, Y. Zeng, B.S. Amirkhiz, M. Wang, Y. Behnamian, J. Luo, A-site deficient perovskite: the parent for in situ exsolution of highly active, regenerable nano-particles as SOFC anodes, Journal of Materials Chemistry A. 3 (2015) 11048–11056. doi:10.1039/C5TA01733E.

[77] P.R. Shearing, J. Golbert, R.J. Chater, N.P. Brandon, 3D reconstruction of SOFC anodes using a focused ion beam lift-out technique, Chemical Engineering Science. 64 (2009) 3928–3933. doi:10.1016/j.ces.2009.05.038.

[78] R. Kiebach, P. Zielke, J.V.T. Hogh, K. Thyden, H.J. Wang, R. Barford, P. V. Hendriksen, Infiltration of SOFC stacks: Evaluation of the electrochemical performance enhancement and the underlying changes in the microstructure, Fuel Cells. 16 (2016) 80–88. doi:10.1002/fuce.201500107.

[79] R. Kiebach, C. Knöfel, F. Bozza, T. Klemensø, C. Chatzichristodoulou, Infiltration of ionic, electronic and mixed conducting nano particles into performance enhancement and stability at different temperatures, Journal of Power Sources. 228 (2013) 170–177. doi:10.1016/j.jpowsour.2012.11.070.

[80] Z. Jiao, N. Shikazono, Study on the effects of polarization on local morphological change of nickel at active three-phase-boundary using patterned nickel- fi lm electrode in solid oxide fuel cell anode, Acta Materialia. 135 (2017) 124–131. doi:10.1016/j.actamat.2017.05.051.

[81] Z. Jiao, N. Shikazono, In operando optical study of active three phase boundary of nickel-yttria stabilized zirconia solid-oxide fuel cell anode under polarization, Journal of Power Sources. 396 (2018) 119–123. doi:10.1016/j.jpowsour.2018.06.001.

[82] A. Utz, H. Störmer, A. Leonide, A. Weber, E. Ivers-tiffée, Degradation and

relaxation effects of Ni patterned anodes in H2–H2O atmosphere, Journal of The Electrochemical Society. (2010) 920–930. doi:10.1149/1.3383041.

[83] A. Leonide, V. Sonn, A. Weber, E. Ivers-Tiffée, Evaluation and modeling of the cell resistance in anode-supported solid oxide fuel cells, Journal of The Electrochemical Society. 155 (2008) B36. doi:10.1149/1.2801372.

[84] T. Nakamura, K. Yashiro, A. Kaimai, T. Otake, Determination of the reaction zone in gadolinia-doped ceria anode for solid oxide fuel cell, Journal of The Electrochemical Society. (2008) 1244–1250. doi:10.1149/1.2975322.

[85] C. Zhang, M.E. Grass, A.H. McDaniel, S.C. DeCaluwe, F. El Gabaly, Z. Liu, K.F. McCarty, R.L. Farrow, M.A. Linne, Z. Hussain, G.S. Jackson, H. Bluhm, B.W. Eichhorn, Measuring fundamental properties in operating solid oxide electrochemical cells by using in situ X-ray photoelectron spectroscopy, Nature Materials. 9 (2010) 944–9. doi:10.1038/nmat2851.

[86] J.H. Yu, G.W. Park, S. Lee, S.K. Woo, Microstructural effects on the electrical and mechanical properties of Ni-YSZ cermet for SOFC anode, Journal of Power Sources. 163 (2007) 926–932. doi:10.1016/j.jpowsour.2006.10.017.

[87] G. Goula, V. Kiousis, L. Nalbandian, I. V Yentekakis, Catalytic and electrocatalytic behavior of Ni-based cermet anodes under internal dry reforming of CH4+CO2 mixtures in SOFCs, Solid State Ionics. 177 (2006) 2119–2123. doi:10.1016/j.ssi.2006.03.040.

[88] E.D. Wachsman, K.T. Lee, Lowering the temperature of solid oxide fuel ells, Science. 334 (2011) 935–939. doi:10.1126/science.1204090.

CURRICULUM VITAE